MODELING OF THE ARMATURE-RAIL INTERFACE IN AN ELECTROMAGNETIC LAUNCHER WITH LUBRICANT INJECTION

A Ph.D. Dissertation
Presented to
The Academic Faculty

by

Lei Wang

In Partial Fulfillment
of the Requirements for the Degree
Doctor of Philosophy in the
George W. Woodruff School of Mechanical Engineering

Georgia Institute of Technology
December, 2008

MODELING OF THE ARMATURE-RAIL INTERFACE IN AN ELECTROMAGNETIC LAUNCHER WITH LUBRICANT INJECTION

Approved by:

Dr. Richard F. Salant, Advisor
School of Mechanical Engineering
Georgia Institute of Technology

Dr. Richard S Cowan
Manufacturing Research Center
Georgia Institute of Technology

Dr. Steven Danyluk
School of Mechanical Engineering
Georgia Institute of Technology

Dr. Waymond R Scott
School of Electrical and Computer Engineering
Georgia Institute of Technology

Dr. Scott Bair
School of Mechanical Engineering
Georgia Institute of Technology

Date Approved: November 6, 2008

I dedicate this work to my wife, XU Binmeng,
and my parents, WANG Shiyou and HE Guirong.
Without their endless love and support,
the completion of this work would not have been possible.

ACKNOWLEDGEMENTS

I would like to express my sincere appreciation to my advisor, Dr. Richard F. Salant, for his guidance and support throughout my graduate study. His devotion to research will be the model for me to follow in my whole life. I also would like to thank my thesis committee, especially Dr. Scott Bair, for his significant help to my research. I wish to thank Dr. Jeffery Streator, for his valuable suggestions and help. I would like to acknowledge my colleague Dr. Dawei Shen for her help in my study and life.

I wish to express my deep appreciation to my family. I thank my parents for their support and guidance through my growth. I thank my wife, Binmeng, for her endless support, encouragement and tolerance.

Finally, I wish to acknowledge the financial support from the Office of Naval Research, U.S. Navy.

TABLE OF CONTENTS

LIST OF TABLES

LIST OF FIGURES

LIST OF SYMBOLS AND ABBREVIATIONS

a	acceleration
b	armature width
B	magnetic flux density
B_0	magnetic flux density at the trailing edge in the film
c	specific heat capacity
D	magnetic diffusion coefficient, $D = \frac{1}{\mu_0 \sigma^*}$
D_h	injection conduit diameter
E	Young's modulus
E^*	electric field intensity
f	friction coefficient
f_{emag}	longitudinal Lorentz force in fluid
f_x, f_y	magnetic body force in the x and y directions
F	cavitation index
$F(x)$	beam shear force
F_{emag}	magnetic force on the armature
F_f	friction force on the armature
F_v	viscous force on the armature
F_{res}	total resistive force on the armature, $F_{res} = F_f + F_v$
F_{total}	total longitudinal force on the armature
G	partial film content, $G = \frac{\rho}{\rho_c} = 1 + (1 - F)\Phi$
G_x	reciprocal of turbulent coefficient, $G_x = 1/K_T$

h	film thickness
$h1, h2$	pocket front and rear depths
h_{min}	minimum film thickness
h_T	local film thickness
H	nondimensional film thickness, h/σ
H_{min}	minimum nondimensional film thickness
I	electric current amperage
I'	contact integral
I^*	moment of inertia
J	electric current density
k	thermal conductivity
K_T	turbulent coefficient
L	lubrication length
L'	inductance gradient
Lc	length of the injection conduit
L_{inj}	injection area length in the MHD analysis
L_{pk}	pocket longitudinal length
L_{pk}'	Length filled by lubricant in the pocket
Lr	length filled by lubricant in the reservoir
m	armature mass including loaded lubricant
m_{load}	initial load in the reservoir
m_{pk}	mass capacity of the pocket
M_T	thermal bending moment
P_1	pressure at the reservoir side of the injection conduit
P_2	pressure at the pocket side of the injection conduit

P	total pressure, $P_{fl} + P_m$
P_{atm}	atmospheric pressure
P_c	cavitation pressure
P_{cont}	contact pressure
P_{fl}	fluid pressure
P_m	magnetic pressure in the fluid
P_{mt}	magnetic pressure at trailing edge
P_{ref}	reference pressure
$\dot{q}$	viscous heat generation rate
q_x	mass flow rate in the film
$\dot{Q}$	mass flow rate in the injection conduit
Q_l	amount of fluid flowing out from interface front edge
Q_{net}	amount of fluid in the pocket
Q_{out}	amount of fluid flowing out of the injection conduit
Q_r	amount of fluid flowing out from the interface trailing edge
R	injection conduit radius
R_{as}	asperity radius
Re_h	local Reynolds number
S	armature cross section area
t	time
Δt	time interval
T	temperature
u, v	fluid x and y velocity
v^*	beam deflection
U	armature speed

V	injection speed
w	distributed beam load
S	armature cross section area
x, y, z	coordinates
α	coefficient of thermal expansion
β	nondimensional variable, $\beta = \frac{\mu UL}{(P_{ref} - P_c)h_0^2}$
γ	surface directional characteristic, length to width ratio of representative asperity
ζ	film length to height ratio, $\zeta = \frac{L}{h_0}$
η	asperity density
θ_1	interface gap angle
θ_2	angle of injection conduit to sliding direction
λ	nondimensional variable, $\lambda = \frac{L}{Ut_0}$
μ	viscosity
μ_0	magnetic permeability of the air
μ_a	magnetic permeability of the armature
μ_f	magnetic permeability of the film
μ_r	magnetic permeability of the rail
μ_T	turbulent viscosity
ξ	nondimensional variable, $\xi = \frac{\rho a h_0^2}{2\mu U}$
ρ	lubricant density/partial content
ρ_c	constant lubricant density

σ combined standard deviation of surfaces

σ^* coefficient of electrical conductivity

$\hat{\sigma}$ dimensionless rms roughness, $\sigma R_{as}^{1/3}\eta^{2/3}$

τ shear stress

ϕ stream function

Φ pressure/density function

ϕ_f, ϕ_{fp}, ϕ_{fs}, ϕ_s, ϕ_x shear flow factor and pressure flow factor

Ω nondimensional variable, $\Omega = \dfrac{\rho_c a L}{P_{ref} - P_c}$

Subscripts:

$(\,)_0$ reference variable

$(\,)_a$ armature

$(\,)_r$ rail

$(\,)_f$ film

Superscripts:

$\overline{(\,)}$ nondimensional variables

SUMMARY

In electromagnetic launcher (EML) systems, the behavior of the materials and forces at the armature-rail interface involves fluid mechanics, electromagnetics, thermal effects, contact mechanics and deformation mechanics. These factors must interact successfully in order for a launch to be successful. A lubricant film either deposited on the rails prior to launch or injected from the armature during launch has been suggested as a means of improving the electrical conductivity of the rail-armature interface and of avoiding the occurrence of arcing. The fluid pressure generated by such film, together with the magnetic force, the contact force and the uneven temperature field in the armature, deforms the armature and changes the interface gap shape. An analytical model to study the interfacial behavior under these influences is necessary in order to predict the performance of a potential EML design and to provide optimization information.

Studies of this interfacial behavior have been done by a number of researchers. However, many critical factors were not included, such as surface roughness, cavitation, injection, magnetic lateral force, interface deformation and thermal effects. The three models presented in this study investigate the influence of those factors on the EML interface problem. The magneto-hydrodynamic (MHD) model establishes a description of the lubrication process under electromagnetic stress but neglects interface deformation. The magneto-elastohydrodynamic (MEHD) model extends the MHD model by considering the lateral magnetic force, interface contact force and elastic deformation. Finally, the magneto-elastothermohydrodynamic (METHD) model adds the thermal effects to the deformation analysis.

A coupled analysis of the interface behavior with the METHD model is developed and the history of a typical launch is studied. Detailed injection, lubrication and launch processes are revealed and the performance is predicted. A failed launch is simulated and the cause of failure is identified to be debris left on the rails. Several operation and design parameters, such as rail surface profile, electric current pattern, reservoir load, lubrication length, pocket size and geometry, injection conduit diameter, are analyzed and a recommended injection design procedure is developed. A scaling study is performed by doubling the dimensions to predict the scaling effects. In the end, the base case configuration and scaled configuration are optimized using the technique developed in this study.

CHAPTER 1

INTRODUCTION

The electromagnetic launcher (EML) is a device driven by magnetic forces, created by an electric current, to propel objects. As shown in Figure 1.1, it has two parallel, conducting rails electrically connected by a free-sliding shunt, called the armature. Electric current flows along one rail, across the armature and back along the second rail. The resulting magnetic field accelerates the armature until it reaches the muzzle. Then the armature and its load leave the electrical circuit and move into free flight. Compared with conventional launchers, the EML has advantages of flexibility, energy efficiency and a short cool down time and is very attractive to military, airplane launcher, and space-related applications. The focus of this study in the EML application is the armature-rail interface (as circled in the figure).

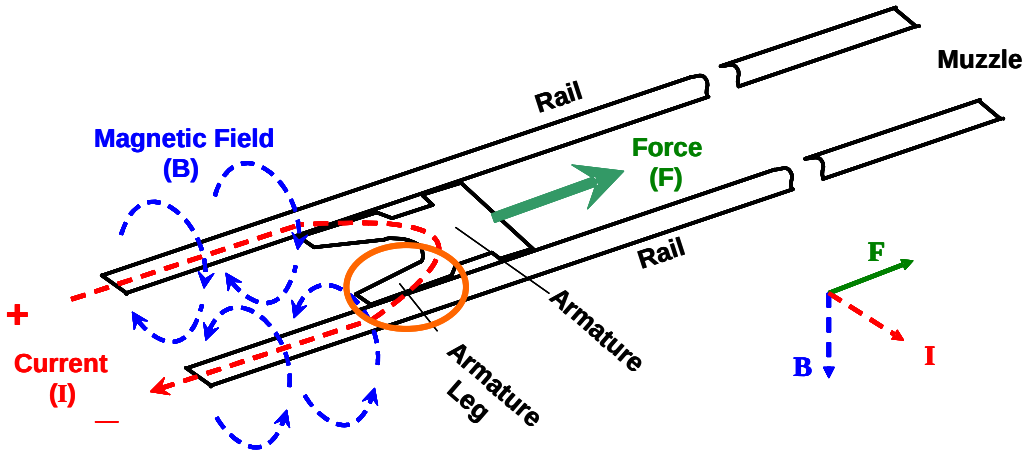

Figure 1.1 Schematic of an EML system

In EML systems, the behavior at the armature-rail interface involves lubrication, electromagnetics, contact mechanics, thermal effects, and elastic deformation. A lubricant film either deposited on the rails prior to launch or injected from the armature during a launch has been suggested (Drobyshevski et al., 1999). An effective implementation of the lubrication process by optimized designs is critical to a successful launch because it improves the electrical conductivity of the rail-armature contact area and avoids the occurrence of arcing across the armature-rail interface. The liquid film also helps to reduce friction and delay or even prevent the melting of the armature. While the existing intensive magnetic field propels the armature, it also exerts lateral forces on the armature legs at the interface. This magnetic force, together with the contact force at the contact area and the fluid pressure from the film, deforms the interface shape and influences the lubrication process. Furthermore, the temperature change caused by joule heating and frictional heating and viscous heating also induces thermal deformation. An analytical model to study the interfacial behavior, especially under such high electromagnetic stresses, is necessary to predict the performance of a potential EML design and provide optimization information.

In this study, three analytical models are developed in a progressive manner, i.e. the magneto-hydrodynamic (MHD) model, the magneto-elastohydrodynamic (MEHD) model, and the magneto-elastothermohydrodynamic (METHD) model. The MHD model studies the lubrication process under magnetic stresses, with an assumed interface gap profile. Results indicate that a converging gap is more favorable to injection and a laminar model generates more realistic solutions for this EML application. Results of the MHD model also suggest that the fluid pressure will deform the interface significantly.

Therefore an electromagnetic module, a contact module, and a deformation module are added and the METHD model is constructed to consider the interface deformation under fluid pressure, magnetic force, and contact force. The electromagnetic module in the METHD model reveals an intense electromagnetic field in the armature. In order to consider the effects of joule heating and thermal deformation that are introduced by this electromagnetic field, a thermal module is developed to achieve the final and the most comprehensive model in this analysis – the METHD model. Since the MHD and MEHD models are intermediate models, the results of both models are included in Appendices A-C. The results presented in the main body of this thesis are all from the final METHD model. EML launches are simulated with different configurations and parameters. The effects of different parameters are studied and an injection system design procedure is developed. A typical launch and a scaled configuration are simulated and then optimized using the techniques developed in this study.

CHAPTER 2

RESEARCH BACKGROUND

As mentioned previously, three analytical models for EMLs are developed in this study progressively:

1. MHD model: this model studies the lubrication process at the armature-rail interface with consideration of surface roughness, cavitation, injection, and magnetic effects in the fluid. The interface profile is assumed in this model.
2. MEHD model: this model extends the MHD model by calculating the electromagnetic field distribution and interface deformation. All the material properties are considered to be constant in this model.
3. METHD model: this model completes this study by adding the thermal effects to the previous MEHD model. The temperature field is calculated and the corresponding temperature-dependent properties and thermal deformation are considered.

2.1 Magneto-hydrodynamic Model

An EML MHD model studies the fluid film lubrication process at the armature-rail interface under electromagnetic stresses. It incorporates the Lorentz force effects on the fluid film with a traditional lubrication model, which involves surface roughness, cavitation, injection and possibly turbulence.

Electrically conducting lubricant has been introduced to the armature-rail interface to increase interface conductivity and prevent arcing (transition) (Drobyshevski et al., 1999 and 2001). In 1999 Yuferev et al. studied the electric current distribution, temperature distribution, and hydrodynamics of a conducting lubricant. They proposed that in EML systems the magnetic body force term in the Navier-Stokes equation can be represented by a *magnetic pressure*. As a result, the hydrodynamic pressure in the Reynolds equation is replaced by a total pressure which is the sum of the hydrodynamic and the magnetic pressure. With the application of this total pressure, the detailed magnetic field distribution is not required in the lubrication analysis. An acceleration term is also included in their formula. This seminal work is very important to an EML lubrication study, although many factors, such as surface roughness, lubricant injection and interface deformation, were not considered.

In 1978 and 1979, Patir and Cheng proposed the average flow model in which the effects of surface roughness on partially lubricated contacts are represented by flow factors obtained from numerical flow simulations. Applications of this flow factor approach have been reported in many articles, such as Li and Weng, 1995 and 1997; Chang et al., 2002. Tripp in 1983 used a perturbation expansion of the pressure term to obtain a simple closed form for the dependence of the flow factors on the roughness parameters. However, currently most EML studies still use a smooth surface model for the armature and rail surfaces (Flegontova and Yuferev, 1999; Drobyshevski et al., 1999; Ghassemi et al., 2003, 2005, 2007).

At the interface, cavitation occurs when the pressure in a lubricant falls below a critical value and air comes out of solution. Such cavitation can be suppressed by a well

designed injection configuration. By using the cavitation index approach (Payvar and Salant, 1992; Salant and Shen, 2002), Salant and Wang (2007) investigated several combinations of interface geometries and lubricant injection locations and found that the most desirable configuration to feed the interface and prevent cavitation is a converging film with upstream injection.

The fluid velocity in EML systems may become very large, and a turbulent model may be needed in this case. In fluid film lubrication, a general approach to treat turbulence is to magnify the fluid viscosity with a turbulence factor. The three most popular turbulent lubrication models to obtain this turbulence factor are the Ng-Pan-Elrod model, Constantinescu's model, and the bulk flow model. Such turbulent models have been successfully applied to bearings (Elrod and Ng, 1967) and seals (Brunetiere et al., 2002, 2003). However, whether the fluid behavior in an EML falls into the turbulence regime is still under investigation. Stefani et al. (2001, 2005) studied both a laminar model and a turbulent model for the melt-lubrication of surface wear in EML armatures and concluded that the laminar model provided a better fit to experiments.

2.2 Magneto-elastohydrodynamic Model

During a launch the armature-rail interface gap shape is deformed by the hydrodynamic pressure, the contact force at the interface and the magnetic force on the armature. The EML MEHD model includes these forces and considers the resultant elastic deformation of the armature.

The hydrodynamic pressure is obtained from the above MHD model. In addition to the magnetic pressure in the fluid film, the magnetic field produces Lorentz forces on the armature, which accelerate the armature in the longitudinal direction and squeeze the armature legs against the rails in the lateral direction. Therefore, unlike the previous model, this MEHD model requires calculation of the magnetic field to obtain the distributed magnetic lateral force. Research on this electromagnetic field is still under development and it has only been reported in few studies. Hsieh in 1995 and 1997, and Thiagarajan and Hsieh in 2007 presented a 3D model (EMAP3D) to calculate the electric and magnetic field distribution. However, the liquid film was not included in his model. By assuming a unidirectional magnetic field, Drobyshevski et al. (1999) developed an analytical model which included the film and the sliding velocity. The Maxwell equations are reduced to a single equation governing the magnetic flux density in their model. Electric current and Lorentz force distributions can be obtained from the results. Ghassemi et al. (2003, 2005, 2007) followed this approach and calculated the thermal, electromagnetic and force distributions in an EML system.

A phenomenon called the velocity skin effect (VSE) has been observed by many researchers either in 2D (Young and Hughes, 1982) and 3D (Barber and Dreizin, 1995) analyses or in experiments (Engel et al., 2008). VSE is caused by the extremely high velocity of the armature. With such high velocity, the electric current concentrates at the rear of the armature-rail contact interface. Barber and Dreizin suggested that in order to increase the velocity at transition, the length of the contact zone should be increased. However, increase of the contact zone length requires an adequate compliance and contact pressure, which are hard to maintain.

As stated above, the armature is squeezed while being inserted into the rails. A contact region exists at the interface, and contact forces are exerted on both surfaces. Such contact force, in addition to the hydrodynamic pressure and magnetic force, deforms the interface during a launch. A few researchers studied the rail deflection under distributed loads (Rapka et al., 1995; Jerome, 2003; Johnson and Moon, 2006; Daneshjoo et al., 2007) and the dynamic response of the containment under different velocities (Tzeng, 2003). James, T. E. and James D. C. in 2001 approximated the contact pressure distribution at startup with a simple cantilever model. Hopkins et al. in 1999 and Newill et al. in 2003 linked an electromagnetic finite element code (EMAP3D) with a structural analysis code (DYNA3D) to study the magnetic induced deformation in the armature. However, very few references in the literature studied the armature deformation (Zielinski et al., 2003). In fact, all the reviewed EML interfacial studies assumed no fluid or a flat/linear interface shape for the fluid film lubrication. Therefore, developing a complete MEHD model, considering the interface deformation under the action of surface contact, fluid pressure and magnetic forces, is necessary to reveal the complex behavior at the armature-rail interface.

3.3 Magneto-elastothermohydrodynamic Model

While the electric current flows through the rail-armature system, heat is generated by joule heating. At the same time, frictional heating is produced at the sliding surfaces and viscous heating is produced in the lubricant during a launch. These heat sources heat up the armature, cause a thermal deformation and change the interface shape. The solid

armature may even melt with this temperature rise. A “melt wave” moving from the back to the front of the armature has been observed with dry sliding EMLs (James, 1995; Woods, 1997; Merrill and Stefani, 2008).

Powell and Zielinski (1995, 1999) studied 2D current and heat transport with joule heating source in an EML configuration, while Critchley et al. (1995) studied a 3D model. Stefani et al. (2001, 2005) studied the viscous heating at the interface, while Hsieh and Kim (1997) used a dry friction model but included joule heating. Drobyshevskii et al. (1999) and Ghassemi et al. (2003, 2005) developed a more realistic model to include both viscous heating and joule heating. They found that resistive liquid films can be used to reduce joule heating of the accelerated body substantially.

Some other factors were also concerned by various researchers. Kim et al. (1999) proposed a phenomenological modeling of imperfect electric contacts and found higher local temperatures at imperfect contacts compared to at perfect contacts.

Unfortunately, no model considering the interface shape change by thermal deformation or solid melting has been carried out yet.

CHAPTER 3

MATHEMATICAL AND NUMERICAL MODEL DEVELOPMENT

The goal of an analytical EML model is the ability to predict the performance of a potential design under given operating conditions, reveal the effects of different design parameters, and provide optimization design guidelines. Since the problem of arcing due to lack of electrical conductivity at the interface is the major concern in this research, the primary modeling goal is the ability to determine the design parameters and operating conditions necessary to provide enough lubrication to avoid arcing. Depending on the scenario of the study, the three models proposed here are composed of some or all of the following five modules: fluid mechanics (lubrication), electromagnetics, contact mechanics, deformation mechanics, and thermal effects.

3.1 Magneto-hydrodynamic Model

3.1.1 Objective

The objective of this MHD model is to develop a fluid mechanics model that includes magnetic stress, surface roughness, cavitation, injection and possibly turbulence. The goal is to reveal the flow pattern in the interface gap and find the best injection configuration

3.1.2 Governing Equations

3.1.2.1 Reynolds Equation with Magnetic Term

A schematic of the armature-rail interface is shown in Figure 3.1. The Cartesian coordinate system is fixed to the armature. The rail moves to the right with velocity U and acceleration a (both are functions of time). Lubricant is present inside the interface gap with a wetted length of L.

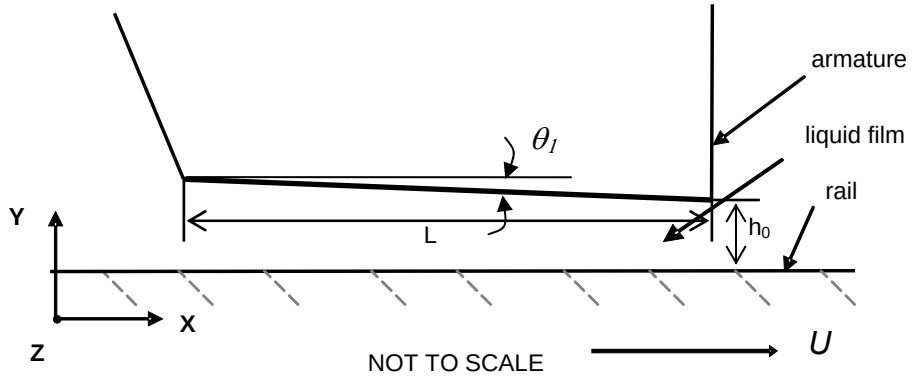

Figure 3.1 Schematic of the armature-rail interface

The Navier-Stokes equation that describes the behavior of the liquid is written as:

$$\rho\left(\frac{\partial u}{\partial t}+u\frac{\partial u}{\partial x}+v\frac{\partial u}{\partial y}\right)=-\frac{\partial P_{fl}}{\partial x}+\mu\frac{\partial^2 u}{\partial y^2}+\rho a+f_{emag} \tag{3.1}$$

where ρ, x, y, u, v, t, P_{fl}, μ, and a are fluid density, longitudinal coordinate, transverse coordinate, longitudinal velocity, transverse velocity, time, fluid pressure, fluid viscosity,

and fluid acceleration. f_{emag} is the longitudinal Lorentz force on the fluid, which is equal to the *x* component of the cross product of electric current and magnetic field ($\vec{J} \times \vec{B}$). As shown in section 3.2, with the assumption that the magnetic field is dominant in the *z* direction, f_{emag} is given by equation 3.2:

$$f_{emag} = -J_y B_z = -\mu_0 B_z \frac{\partial B_z}{\partial x} = -\frac{1}{2}\mu_0 \frac{\partial B_z{}^2}{\partial x} \tag{3.2}$$

where μ_0 is the magnetic permeability. Consequently, the Lorentz force term in the Navier-Stokes equation is substituted by an magnetic pressure term $P_m = B^2/2\mu_0$ and is combined with the fluid pressure term to create a total pressure $P = P_m + P_{fl}$. With the total pressure term, the N-S equation is reduced to its conventional form without explicit magnetic terms, as in equation 3.3.

$$\rho\left(\frac{\partial u}{\partial t} + u\frac{\partial u}{\partial x} + v\frac{\partial u}{\partial y}\right) = -\frac{\partial P}{\partial x} + \mu\frac{\partial^2 u}{\partial y^2} + \rho a \tag{3.3}$$

The thickness of the fluid film in the interface gap falls in the film lubrication category and therefore traditional lubrication assumptions are applied as follows:

1) The flow field in the fluid film is two-dimensional.
2) The flow is incompressible, laminar and quasi-steady.

3) The classical lubrication approximation is valid in the film, i.e., fluid pressure across the film is constant, velocity is dominant in the *x*-direction, and all the velocity spatial derivatives are neglected except $\frac{\partial^2 u}{\partial y^2}$,

4) Non-slip boundary conditions are applied at both upper and lower surfaces.

The Reynolds equation (equation 3.4) takes place of the Navier-Stokes equation with these assumptions

$$\frac{d}{dx}(h^3 \frac{dP}{dx}) = 3(2\mu U + \rho a h^2)\frac{\partial h}{\partial x} \tag{3.4}$$

where h is the film thickness. As in the Navier-Stokes equation, the magnetic effects are included in this equation by adopting the total pressure P.

3.1.2.2 Surface Roughness

Measurements suggest that both the armature surface and the rail surface are not smooth. Figure 3.2 shows the surface profiles of the rail under different conditions. The black line measures the original surface before a launch. The red lines are surface profiles after two dry launches. Surface profiles after lubricated launches are given in the two blue lines. Two sets of data are measured at distances of 0.05m and 1.0 m to the starting point. Roughness of the original surface is about 0.7 micron and the roughness increases to 1.3 microns after a lubricated launch.

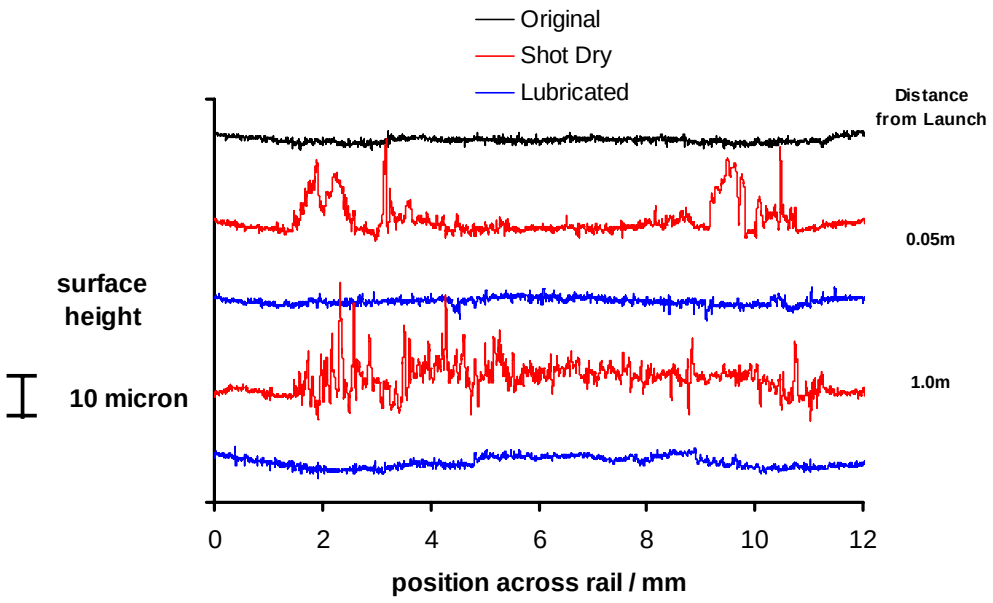

Figure 3.2 Typical rail surface profiles (Bair, 2008)

The average flow model by Patir and Cheng is used to include surface roughness, with consideration of asperity aspect ratio and orientation. With the flow factors ϕ_x and ϕ_s given in their model, the average Reynolds equation is

$$\frac{d}{dx}(\phi_x h^3 \frac{dP}{dx}) = 3(2\mu U + \rho a h_T^{\ 2})\frac{\partial h_T}{\partial x} + 6\mu U\sigma\frac{\partial \phi_s}{\partial x} \tag{3.5}$$

where σ is the combined r.m.s surface roughness and $h_T = \frac{h}{2} + \frac{h}{2} erf\left(\frac{h}{\sigma\sqrt{2}}\right) + \frac{\sigma}{\sqrt{2\pi}}\exp\left(\frac{-h^2}{2\sigma^2}\right)$ is the local film thickness with a Gaussian distribution.

3.1.2.3 Cavitation

Test runs suggest that cavitation occurs at the interface under certain conditions. Cavitation causes the interface to lose electrical conductivity and may result in arcing. Therefore, a cavitation model is included in this study. The mathematical equation for cavitation in this EML application is derived from the compressible rough surface lubrication equation, which is

$$\frac{\partial}{\partial x}(\phi_x \rho h^3 \frac{\partial P}{\partial x}) = a\frac{\partial \rho^2 h_T^3}{\partial x} + 6\mu U \frac{\partial \rho h_T}{\partial x} + 6\mu U \sigma \frac{\partial \rho \phi_s}{\partial x}. \tag{3.6}$$

At cavitating locations, $\frac{\partial P}{\partial x} = 0$. Equation 3.6 reduces to

$$a\frac{\partial \rho^2 h_T^3}{\partial x} + 6\mu U \frac{\partial \rho h_T}{\partial x} + 6\mu U \sigma \frac{\partial \rho \phi_s}{\partial x} = 0. \tag{3.7}$$

Following the cavitation index approach by Payvar and Salant, we define:

$$\frac{P - P_c}{P_{ref} - P_c} = F\Phi \qquad \begin{matrix} F = 1 \text{ for } \Phi > 0 \\ F = 0 \text{ for } \Phi < 0 \end{matrix} \tag{3.8}$$

$$\frac{\rho}{\rho_c} = 1 + (1 - F)\Phi \tag{3.9}$$

where P_c is the cavitation pressure, P_{ref} the reference pressure. F is the cavitation index, Φ is the dimensionless pressure in the liquid film region, and $(1+\Phi)$ is the partial film content in the cavitation zone. ρ_c is the liquid density in the full film region and is taken to be constant.

With above definitions, equation 3.6 is modified to be valid in both full film and cavitating regions as:

$$(P_{ref} - P_c)\frac{\partial}{\partial x}(\phi_x h^3 \frac{\partial \Phi F}{\partial x}) = a\rho_c \frac{\partial G^2 h_T^3}{\partial x} + 6\mu U_0 (\frac{\partial G h_T}{\partial x} + \sigma \frac{\partial G \phi_s}{\partial x}) + 12\mu V_{in} \qquad (3.10)$$

where $G = \frac{\rho}{\rho_c} = 1 + (1-F)\Phi$.

It must be noted that cavitation should be determined using the real fluid pressure. The equation above solves the total pressure and will produce a certain amount of error in determining fluid cavitation. However, the detailed magnetic field distribution in the film is unknown in this MHD model and therefore the real fluid pressure cannot be calculated. As a result, cavitation is still determined by the total pressure in the MHD model. The real fluid pressure approach will be discussed later in Section 3.2.4.2 when the magnetic field distribution in the film can be calculated.

3.1.2.4 Injection

Liquid injection supplies lubricant to the interface and avoids cavitation. To our knowledge, no research on lubricant injection can be found in previous EML studies.

Two injection designs are considered in this study. One is a direct injection to the interface (as in Figure 3.3a) while the other involves a more complicated system with a lubricant reservoir and an injection pocket (Figure 3.3b). The purpose of the direct injection study is to find the optimal gap shape and injection location to sufficiently fill the interface as well as suppress cavitation. In this study, the injection speed is pre-specified. Lubricant is injected from the injection port and simultaneously flows out of the interface from the leading and trailing edges. In the second reservoir-pocket injection system, a reservoir located inside the armature holds the lubricant initially. During a launch, the injection is driven by armature acceleration, and its speed is determined by equations given later, involving acceleration, reservoir load and fluid pressure. Lubricant injected from the reservoir flows through a conduit into a pocket and fills the interface during the launch. The complete history of launches with the reservoir-pocket injection will be studied, and the results will help to find the minimum reservoir load as well as to improve pocket design.

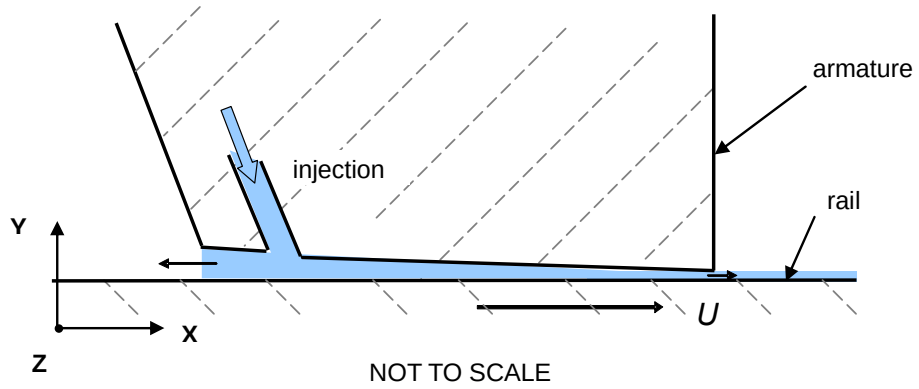

(a) Direct injection

Figure 3.3 Schematic of the two injection configurations

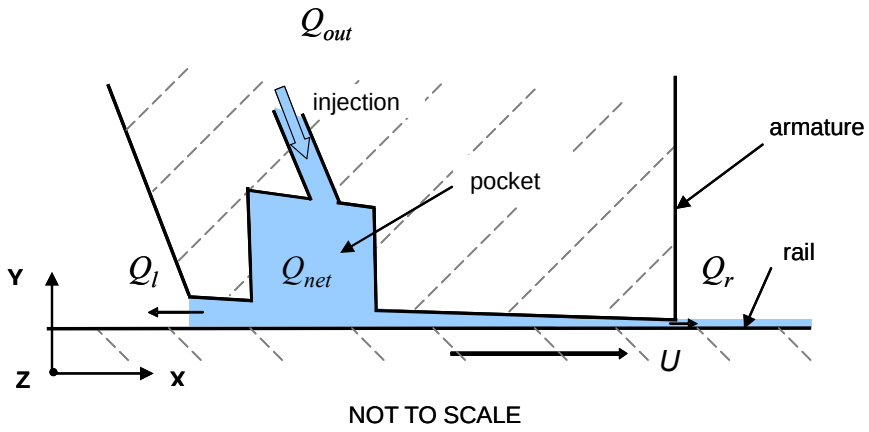

(b) Injection with a pocket

Figure 3.3 continued

In the direct injection model, injection is included by adding an additional injection term containing the injection speed V to the Reynolds equation:

$$\frac{\partial}{\partial x}(\phi_x h^3 \frac{\partial F\Phi}{\partial x}) = \rho a \frac{\partial\left(G^2 h_T^3\right)}{\partial x} + 6\mu U \frac{\partial G\left(h_T + \sigma\phi_s\right)}{\partial x} + 12\delta(x)\mu V \tag{3.11}$$

$$\delta(x) = \begin{cases} 1 & \text{at injection location} \\ 0 & \text{elsewhere} \end{cases}$$

In the reservoir-pocket injection model, pressure at the reservoir side of the injection conduit is approximated by $P_1 = \rho a L_r + P_{atm}$, where L_r denotes the length filled by lubricant in the reservoir. Flow in the conduit is modeled as Poiseuille flow with mass flow rate determined by the Hagen-Poiseuille Equation, equation 3.12.

$$\frac{8\mu}{\rho\pi R^4}\dot{Q}+\frac{1}{\pi R^2}\frac{d\dot{Q}}{dt}=\left(\frac{P_1-P_2}{L_c}+\rho a\cos\theta_2\right) \tag{3.12}$$

where R and L_c are the radius and length of the injection conduit, respectively. θ_2 is the angle of the injection conduit to the sliding direction. The pressure at the injection port P_2 is the static hydraulic pressure if the pocket is not full. In this case, P_2 is proportional to the product of armature acceleration a and pocket filled length L_{pk}', $P_2 = \rho a L_{pk}'$. If the pocket is full, P_2 is determined from the balance of flows into and out of the interface.

Figure 3.4 illustrates the injection process in the reservoir-pocket system. At the beginning, lubricant is loaded in the reservoir (Figure 3.4a). As the armature starts to accelerate, the inertia effects drive the lubricant out through the injection conduit into the pocket (Figure 3.4b). Fluid in the pocket flows in two directions, with one downstream flow towards the trailing edge and one upstream flow towards the leading edge. The down stream flow is our main focus in this study because it lubricates the interface, conducts the electric current and removes the generated heat at the interface. The up stream flow is modeled using a separate lubrication model, and fluid flowing out front the front edge is assumed to leak from the sides and never flow back into the pocket. As the launch process goes on, the reservoir quickly drains out and the pocket behaves as a spare reservoir to continually supply lubricant to the interface (Figure 3.4c)

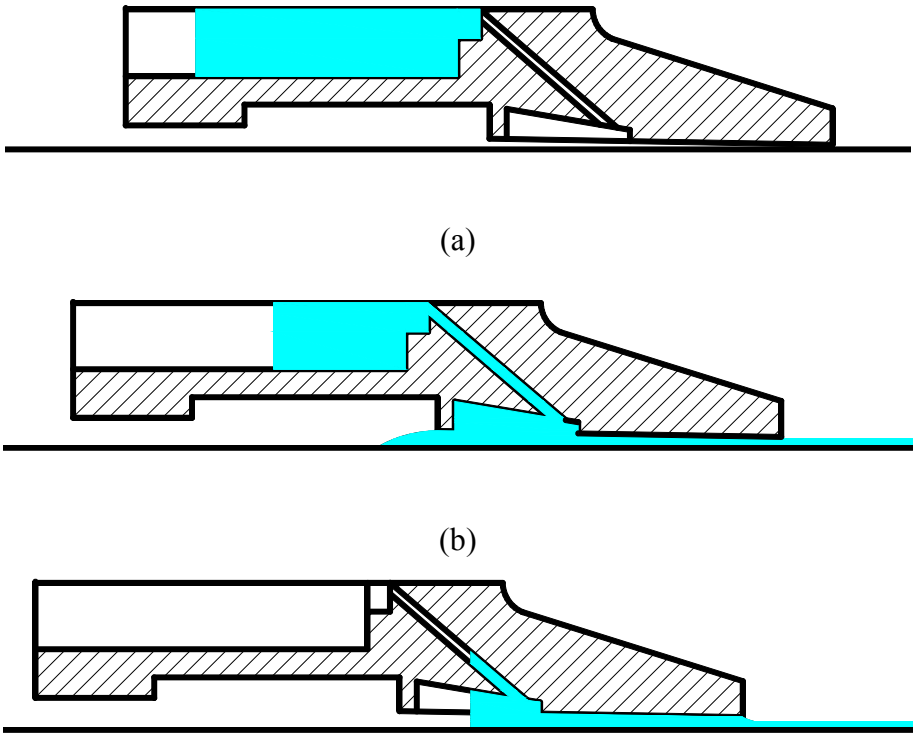

Figure 3.4 Injection process of the reservoir-pocket configuration at different stages

The mass amounts of fluid that have flowed across boundaries (Q_{out}, Q_l, Q_r) and the fluid mass remaining in the pocket (Q_{net}) are important for evaluating the injection performance. After solving the Reynolds equation, those values are determined by integrating the velocity field across the boundaries at each time step. Q_{out} and Q_{net}, denote the amount of fluid that has flowed out from the injection conduit and the amount of fluid accumulated in the pocket for one side of the armature. Q_l and Q_r denote the amounts of fluid that have flowed out from the leading edge and the trailing edge for one side, respectively. Equations for these mass flow amounts are given below. It must be noted that a certain amount of lubricant resides in the injection conduit after the reservoir is

depleted, as shown in Figure 3.4c. Therefore, this amount of lubricant must also be considered in Q_{out} as in equation 3.13.

$$Q_{out} = \begin{cases} \int_0^t \dot{Q} dt & \text{if reservoir not empty} \\ \dfrac{\pi R^2 \Delta L'_{pk}}{\cos\theta_2} & \text{if reservoir empty} \end{cases} \tag{3.13}$$

$$Q_l = \rho b \int_0^t \int_0^h u dy dt \Big|_{\text{at leading edge}} \tag{3.14}$$

$$Q_r = \rho b \int_0^t \int_0^h u dy dt \Big|_{\text{at trailing edge}} \tag{3.15}$$

$$Q_{net} = \begin{cases} Q_{out} - Q_l - Q_r & \text{if pocket not full} \\ m_{pk} & \text{if pocket full} \end{cases} \tag{3.16}$$

3.1.2.5 Turbulence

As stated earlier, all three turbulent models involve replacing the original fluid viscosity μ with a turbulent viscosity μ_T ($\mu_T = K_T \mu$). Different models lead to different equations for K_T. In Constantinescu's model, K_T is calculated from a single equation of local Reynolds number Re_h as in equation 3.17. The Ng-Pan-Elrod model uses piece-wise equations for the turbulent coefficient K_T in equation 3.18. The Hirs bulk flow model adopts a critical local Reynolds number $\mathrm{Re}_{h,\,critical}$ to distinguish the laminar regime and turbulent regime (equation 3.19).

$$K_T = 1 + 0.002166\,\mathrm{Re}_h^{\,0.8265} \tag{3.17}$$

$$G_x = \frac{12}{K_T} = \begin{cases} 1 & \mathrm{Re}_h < 100 \\ 12\sum_n a_n (\log \mathrm{Re}_h)^{n-1} & 100 \le \mathrm{Re}_h < 10,000 \\ 0.168 - 0.1368(\log \mathrm{Re}_h - 4.0) & \mathrm{Re}_h > 10,000 \end{cases} \quad (3.18)$$

$$K_T = \begin{cases} 1 & \mathrm{Re}_h < \mathrm{Re}_{h,critical} \\ \max(0.005725\,\mathrm{Re}_h^{0.75}, 1) & \mathrm{Re}_h \ge \mathrm{Re}_{h,critical} \end{cases} \quad (3.19)$$

Figure 3.5 compares the predicted turbulent coefficient K_T with different local Reynolds numbers by the three models. Little difference is observed among these three models. Constantinescu's model gives a smoother transition between the laminar regime and the turbulent regime. It is chosen for our turbulent simulations.

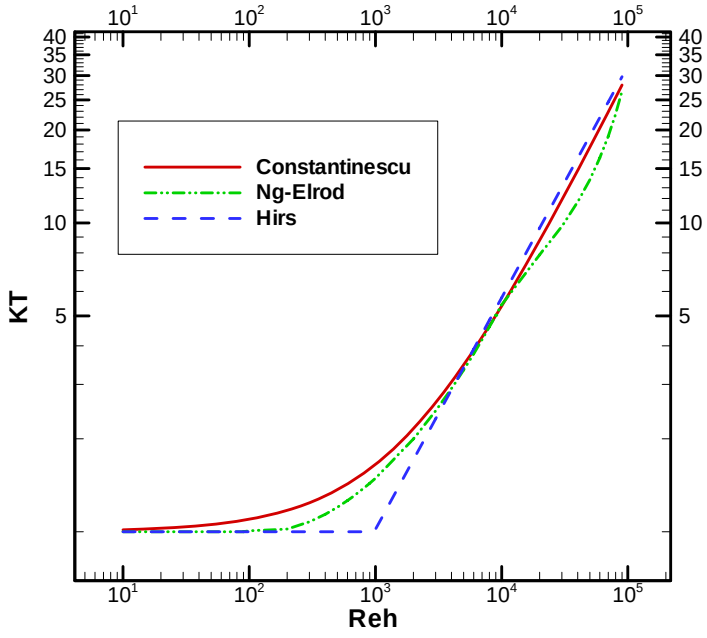

Figure 3.5 Comparison of different turbulent models

3.1.2.6 Unified Nondimensional Reynolds Equation

In previous sections, different influencing factors, such as surface roughness, cavitation, injection and turbulence, have been considered separately. It is necessary to construct a unified Reynolds equation to include all these factors. Combining all the terms discussed before, the unified Reynolds equation is written as:

$$(P_{ref} - P_c)\frac{\partial}{\partial x}(\frac{\phi_x h^3}{K_T}\frac{\partial \Phi F}{\partial x}) = a\rho_c \frac{\partial}{\partial x}\left(\frac{G^2 h_T^3}{K_T}\right) + 6\mu U(\frac{\partial G h_T}{\partial x} + \sigma\frac{\partial G\phi_s}{\partial x}) + 12\delta(x)\mu V \quad (3.20)$$

With nondimensional variables $\bar{x} = x/L$, $\bar{h} = h/h_0$, $\bar{\sigma} = \sigma/h_0$, $\bar{V} = V/U_0$, equation 3.20 can be normalized as:

$$\frac{\partial}{\partial \bar{x}}(\frac{\phi_x \bar{h}^3}{K_T}\frac{\partial \Phi F}{\partial \bar{x}}) = \Omega\frac{\partial}{\partial \bar{x}}\left(\frac{G^2 \bar{h}_T^3}{K_T}\right) + 6\beta\frac{\partial G\bar{h}_T}{\partial \bar{x}} + 6\beta\frac{\partial G\bar{\sigma}\phi_s}{\partial \bar{x}} + 12\delta(x)\beta\zeta\bar{V} \quad (3.21)$$

where $\Omega = \frac{\rho_c a L}{P_{ref} - P_c}$, $\beta = \frac{\mu U L}{(P_{ref} - P_c)h_0^2}$, $\zeta = \frac{L}{h_0}$ are the nondimensional variables.

3.1.2.7 Velocity and Stream Function

The longitudinal velocity component *u* in the film can be derived from the Navier-Stokes equations with lubrication assumptions and rough surface corrections. It is

calculated from equation 3.22 for the dimensional form or equation 3.23 for the nondimensional form:

$$u = \frac{1}{2\mu K_T}\left(\phi_x \frac{\partial P}{\partial x} - \rho a\right)(y-h)\,y + U\left(1-\frac{y}{h}\right) - \frac{3U\sigma\phi_s}{h^3}\,y(y-h) \qquad (3.22)$$

$$\bar{u} = \left(\frac{\phi_x}{2\beta K_T}\frac{\partial \bar{P}}{\partial \bar{x}} - \frac{\xi}{K_T} - \frac{3\bar{\sigma}\phi_s}{\bar{h}^3}\right)(\bar{y}-\bar{h})\,\bar{y} + \left(1-\frac{\bar{y}}{\bar{h}}\right) \qquad (3.23)$$

where $\xi = \dfrac{\rho a h_0^2}{2\mu U}$.

By integrating the longitudinal velocity term *u*, the corresponding mass flow rate at a cross section at location *x* with film thickness of *h* is written as:

$$q_x = \int_h \rho u dy = -\phi_x \frac{\rho h^3}{12\mu}\frac{\partial P}{\partial x} + \frac{\rho^2 h_T^3 a}{12\mu} + \frac{\rho U h_T}{2} + \frac{\rho U \sigma \phi_s}{2}. \qquad (3.24)$$

Stream function ϕ is used to visualize the flow field in this study. It is a scalar function which satisfies equation 3.25:

$$u = \frac{\partial \phi}{\partial y} \qquad v = -\frac{\partial \phi}{\partial x} \qquad (3.25)$$

The stream function can also be normalized as $\bar{\phi} = \dfrac{\phi}{U_0 h_0}$. The stream function is constant along surfaces. It is treated as zero along the rail surface (y=0). The value in the film at a given location ($\bar{x}$, $\bar{y}$) is calculated by integration from the rail surface as in equation 3.26. The velocity component v can be computed from the stream function by using equation 3.25.

$$\bar{\phi} = \int_0^{\bar{y}} \frac{\rho}{\rho_c} \bar{u} d\bar{y} = G\left[\bar{y} - \frac{\bar{y}^2}{2\bar{h}} + \left(\frac{\phi_x}{2\beta K_T} \frac{\partial \bar{P}}{\partial \bar{x}} - \frac{G\xi}{K_T} - \frac{3\bar{\sigma}\phi_s}{\bar{h}^3} \right) \left(\frac{1}{3}\bar{y}^3 - \frac{\bar{h}}{2}\bar{y}^2 \right) \right] \tag{3.26}$$

The shear stress and the corresponding viscous heat generation rate in the fluid are given by equations 3.27 and 3.28:

$$\tau = \frac{\mu K_T U}{h} \left(\phi_f + \frac{2y-h}{h} \phi_{fs} \right) + \frac{2y-h}{2} \phi_{fp} \left(\frac{dP}{dx} - \rho a \right) \tag{3.27}$$

$$\begin{aligned} \dot{q} = \tau \frac{\partial u}{\partial y} = & \left[\frac{\mu K_T U}{h} \left(\phi_f + \frac{2y-h}{h} \phi_{fs} \right) + \frac{2y-h}{2} \phi_{fp} \left(\frac{dP}{dx} - \rho a \right) \right] \\ & \left[\left(\frac{1}{2\mu K_T} \phi_x \frac{\partial P}{\partial x} - \frac{1}{2\mu K_T} \rho a - \frac{3U\sigma\phi_s}{h^3} \right) (2y-h) - \frac{U}{h} \right] \end{aligned} \tag{3.28}$$

3.1.3 Computational Scheme

The nondimensional equation 3.21 is discretized with the finite volume method by Patankar (1980). As shown in 3.6, a node P has two neighboring nodes E and W for a one-dimensional case. The control volume of P is shaded with its boundaries denoted by *w* and *e*.

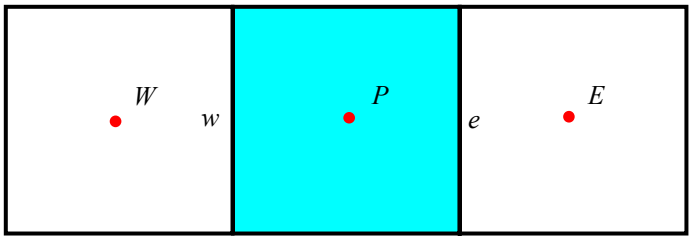

Figure 3.6 Individual control volume and neighboring nodes

The Reynolds equation for Φ is written in a finite volume form:

$$a_P \Phi_P = a_E F_E \Phi_E + a_W F_W \Phi_W + s \tag{3.29}$$

where $a_P = \left(K_e + K_w\right) F_P + 6\beta\Delta\bar{x}\left(1-F\right)\bar{h}_{T,e}$

$$a_W = K_w$$

$$a_E = K_e$$

$$s = -\Delta\bar{x}\begin{pmatrix} \Omega\left(\dfrac{G_P^2\bar{h}_{T,e}^3}{K_{T,P}} - \dfrac{G_W^2\bar{h}_{T,w}^3}{K_{T,W}}\right) + 6\beta\left(\bar{h}_{T,e} - G_W\bar{h}_{T,w}\right) \\ +6\beta\sigma\left(G_P\phi_{s,e} - G_W\phi_{s,w}\right) + 12\delta(x)\Delta\bar{x}\beta\zeta\bar{V} \end{pmatrix}.$$

and where the coefficients at boundaries *e* and *w* are evaluated as:

$$K_e = \frac{K_E K_P}{K_E + K_P}$$

$$K_w = \frac{K_W K_P}{K_W + K_P}$$

$$K_E = \left(\frac{\phi_x \bar{h}^3}{K_T}\right)_E$$

$$K_W = \left(\frac{\phi_x \bar{h}^3}{K_T}\right)_W$$

$$\bar{h}_e = \frac{\bar{h}_E + \bar{h}_P}{2}$$

$$\bar{h}_w = \frac{\bar{h}_W + \bar{h}_P}{2}.$$

The boundary conditions for equation 3.20 are

$$\Phi = \begin{cases} P_{atm} & \text{at leading edge} \\ P_{atm} + P_{mt} & \text{at trailing edge} \end{cases} \tag{3.30}$$

where P_{atm} is the atmospheric pressure. The magnetic pressure at the trailing edge P_{mt} can be either computed from equation 3.31 or 3.32. In the two equations, L' is the inductance gradient of the system, I the current amperage, S the cross section area, B_0 the magnetic flux density at the trailing edge and μ_f is the magnetic permeability in the film. An algebraic method to find L' can be found in the book by Marshall and Wang (2004). Liquid flowing out from the leading edge leaks around the armature without flowing back into the gap.

$$P_{mt} = \frac{L'I^2}{2S} \tag{3.31}$$

$$P_{mt} = \frac{B_0^{\,2}}{2\mu_f} \tag{3.32}$$

Armature acceleration is determined from L' from equation 3.33

$$a(t) = \frac{L'I^2}{2m} \tag{3.33}$$

The discretized equation 3.31 is solved using the Tridiagonal Matrix Algorithm (TDMA) method with relaxation (Patankar, 1980). Once pressure distribution is determined, stream function, velocity components, and mass flow rates can be calculated from equations 3.26, 3.25 and 3.24.

3.1.4 Results and Discussion

Injection is used to provide lubricant to the interface and to suppress cavitation. Before any detailed injection design of the reservoir-pocket configuration can be discussed, the most beneficial interface gap profile and injection location must be determined. In this study, these two parameters are determined by preliminary simulations with a direct injection configuration and given injection speeds.

The interface gap is assumed to be wedge-shaped. Three profiles are considered in this study: converging, parallel, and diverging. For a converging gap as shown in Figure 3.1, the angle of the upper surface to the longitudinal direction (θ_1) is positive and the minimum film thickness h_0 exists at the trailing edge. For a diverging gap, θ_1 is negative and h_0 exists at the leading edge. With parallel surfaces, the film thickness is constant along the gap and θ_1 equals zero. The minimum film thickness for all the cases is assumed to be 3σ.

The lubricant is injected into the interface from the armature at a specified location and over a specified length. Three injection locations are considered in this study: upstream, center, and downstream. The upstream and downstream boundaries of the solution space (at the leading and trailing edges of the interfaces) are treated as flooded with liquid, in order to avoid the complexities of dealing with a free surface between air and liquid. Since flooding at the boundaries only occurs when the interface is completely filled with the injected fluid, this analysis is completely valid only under such a condition. However, as will be seen below, even when this condition is not met, the analysis does provide useful information regarding the effectiveness of the injection.

Combinations of the different interface gap profiles and the different injection locations are simulated. It is found that the converging gap consumes the least lubricant at the interface and the upstream injection requires the lowest injection pressure. The combination of them two is the most beneficial injection configuration and is chosen for the succeeding reservoir-pocket injection study. It is also found that the turbulent model produces unrealistic results and the laminar model is more appropriate for this EML application, consistent with the results of Stefani et al. The details of these simulations are listed in Appendix A.

3.1.5 Launch History Prediction

The history of a launch with the reservoir-pocket configuration is predicted using the computational procedure shown in Figure 3.28. The meanings of Q_l, Q_{net}, Q_{out} and Q_r have been explained in Section 3.1.2.4. Q_{out} is balanced by Q_{net}, Q_l and Q_r during the injection process. The computational code automatically determines P_2, the pressure at the injection port in the pocket, to find the correct injection flow rate Q_{out} as shown in the figure.

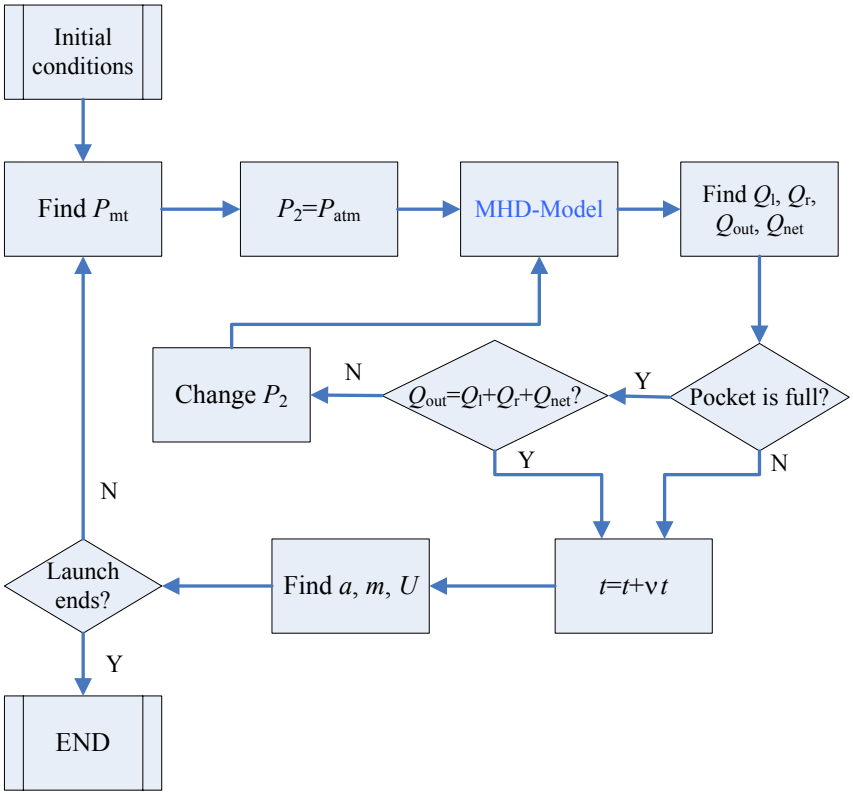

Figure 3.7 Flowchart of launch history prediction with the MHD model

Armature acceleration, velocity and mass are determined by equations 3.34, 3.35, and 3.36.

$$a(t) = \frac{L'I(t)^2}{2m(t)} \tag{3.34}$$

$$U(t+dt) = U(t) + a(t)\Delta t \tag{3.35}$$

$$m(t+\Delta t) = m(t=0) - 2Q_{out}(t) \tag{3.36}$$

The results and discussion of the MHD model's performance can be found in Appendix B.

3.2 Magneto-elastohydrodynamic Model

3.2.1 Objective

The presence of magnetic field, fluid pressure and contact force results in elastic deformation at the interface, as shown in Figure 3.8. The objective of the MEHD model is to study the coupled behaviors of lubrication process, magnetic field, and interface deformation. An electromagnetic model for magnetic field and Lorentz force distribution and a contact model for interface contact force are developed and combined with the MHD model to construct a more complete analytical model.

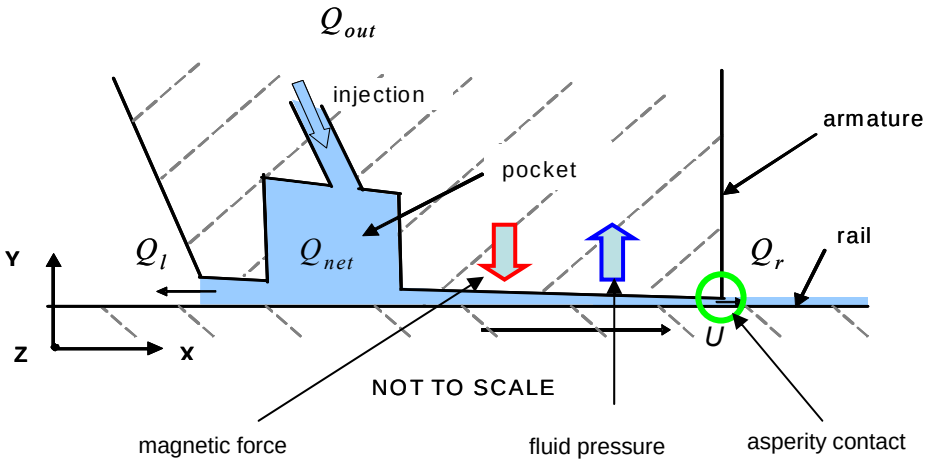

Figure 3.8 The coupled fields at the armature-rail interface

3.2.2 Electromagnetic Field

3.2.2.1 Problem Description

In EML, the electromagnetic field produced by the driving electric current affects the launch process in multiple ways: it accelerates the armature in the longitudinal direction and squeezes the armature leg in the lateral direction; it changes the fluid flow with the Lorentz force; it generates joule heating and results in an uneven temperature field. However, it is quite a challenge to compute the electromagnetic field because of the dynamism of the process and the presence of both lubricant and the velocity skin effect. This electromagnetic field has been widely investigated by a number of researchers with different methods, such as Hsieh in 1995 and 1997. However, these methods either failed to consider the presence of lubricant or neglected the velocity skin effect. Furthermore, the complete 3D models in those studies are hard to apply, and they take considerable modeling and computational efforts.

Considering the special characteristics of the electromagnetic field in EML applications, a simplified model was derived by researchers. This model was first presented by Drobyshevskii et al. in 1999 and later adopted by many researchers such as Ghassemi in 2003, 2005 and 2007. By taking advantage of the characteristics of the electromagnetic field in EML systems, this simplified model reduces the 3D electromagnetic equations to a 2D equation of magnetic flux density B, with consideration of the lubricant and velocity terms. This approach provides a more effective way to calculate electromagnetic field distribution with acceptable precision.

For convenience, this simplified electromagnetic model is called the EMAG model in this study.

3.2.2.2 Governing Equations

For a quasi-static state, the governing Maxwell's equations for an electromagnetic field are

$$\nabla \times \vec{B} = \mu_0 \cdot \vec{J} \tag{3.37}$$

$$\nabla \times \overrightarrow{E^*} = -\frac{\partial \vec{B}}{\partial t} \tag{3.38}$$

$$\vec{J} = \sigma^* \left(\overrightarrow{E^*} + \vec{U} \times \vec{B} \right). \tag{3.39}$$

where B is the magnetic flux density, μ_0 the magnetic permeability in air, J the electric current density, E^* the electrical field intensity, t the time, σ^* the coefficient of electrical conductivity, and U the velocity.

Combining equations (3.37) and (3.39) leads to

$$\frac{\nabla \times \vec{B}}{\mu_0} = \sigma^* \left(\overrightarrow{E^*} + \vec{U} \times \vec{B} \right). \tag{3.40}$$

Equation 3.40 can be reorganized as

$$\overrightarrow{E^*} = \frac{\nabla \times \vec{B}}{\mu_0 \sigma^*} - \vec{U} \times \vec{B} \,. \tag{3.41}$$

By inserting equation 3.41 into 3.38, we finally get

$$\frac{\partial \vec{B}}{\partial t} = \nabla \times \left(\frac{\nabla \times \vec{B}}{\mu_0 \sigma^*} - \vec{U} \times \vec{B} \right). \tag{3.42}$$

and

$$\frac{1}{\mu_0 \sigma^*} \left(\nabla \times \left(\nabla \times \vec{B} \right) \right) = -\frac{\partial \vec{B}}{\partial t} + \left(\nabla \times \left(\vec{U} \times \vec{B} \right) \right) \tag{3.43}$$

The magnetic field has been found to be dominant in the *z* direction and negligible in the other two directions. Therefore, the two negligible components are ignored and the magnetic field is represented by its *z* component, namely $\vec{B} = B\vec{k}$. With this assumption, equation 3.43 is simplified to three equations for the rail (equation 3.44), the armature equation 3.45) and the liquid film (equation 3.46) respectively:

$$\frac{\partial B_r}{\partial t} + U \frac{\partial B_r}{\partial x} = \frac{\partial}{\partial x} \left(D_r \frac{\partial B_r}{\partial x} \right) + \frac{\partial}{\partial y} \left(D_r \frac{\partial B_r}{\partial y} \right) \tag{3.44}$$

$$\frac{\partial B_a}{\partial t} = \frac{\partial}{\partial x} \left(D_a \frac{\partial B_a}{\partial x} \right) + \frac{\partial}{\partial y} \left(D_a \frac{\partial B_a}{\partial y} \right) \tag{3.45}$$

$$\frac{\partial B_f}{\partial t} + u(y)\frac{\partial B_f}{\partial x} = \frac{\partial}{\partial x}\left(D_f \frac{\partial B_f}{\partial x} \right) + \frac{\partial}{\partial y}\left(D_f \frac{\partial B_f}{\partial y} \right), \tag{3.46}$$

with subscript *r* for the rail, *a* for the armature and *f* for the film.

Assuming B_f is uniform across the film (*y* direction), integrating equation 3.46 in the film yields

$$h\frac{\partial B_f}{\partial t} + q_x \frac{\partial B_f}{\partial x} = \frac{\partial}{\partial x}\left(D_f h \frac{\partial B_f}{\partial x} \right) + D_a \frac{\partial B_a}{\partial y} - D_r \frac{\partial B_r}{\partial y} \tag{3.47}$$

where $D = \frac{1}{\mu_0 \sigma^*}$, $q_x(x) = \int_0^h u(x,y)dy$.

Once the magnetic field is calculated, the electric current and the magnetic body force can be obtained from equations 3.48-3.51.

$$J_{x,i} = \frac{1}{\mu_{0,i}}\frac{\partial B}{\partial y} \tag{3.48}$$

$$J_{y,i} = -\frac{1}{\mu_{0,i}}\frac{\partial B}{\partial x} \tag{3.49}$$

$$f_{x,i} = J_{y,i}B = -\frac{1}{\mu_{0,i}} B\frac{\partial B}{\partial y} \tag{3.50}$$

$$f_{y,i} = -J_{x,i}B = -\frac{1}{\mu_{0,i}} B\frac{\partial B}{\partial x} \tag{3.51}$$

where $i = r, a, f$ represents rail, armature and fluid, respectively.

3.2.2.3 Computational Scheme

In the MEHD model, all the material properties are considered to be independent of temperature. With the finite volume method and fully implicit scheme, equation 3.44 is discretized as

$$a_p B_{i,j} = a_E B_{i+1,j} + a_W B_{i-1,j} + a_N B_{i,j+1} + a_S B_{i,j-1} + a_p^0 B_{i,j}^{n-1}, \tag{3.52}$$

where

$$a_p = a_W + a_E + a_S + a_N + a_P^0$$

$$a_E = \frac{1}{\Delta x^2} - \frac{\mu_r \sigma_r^* U}{2\Delta x}$$

$$a_W = \frac{1}{\Delta x^2} + \frac{\mu_r \sigma_r^* U}{2\Delta x}$$

$$a_N = a_S = \frac{1}{\Delta y^2}$$

$$a_P^0 = \frac{\mu_r \sigma_r^*}{\Delta t}.$$

Similarly, equation 3.45 is discretized as

$$a_p B_{i,j} = a_E B_{i+1,j} + a_W B_{i-1,j} + a_N B_{i,j+1} + a_S B_{i,j-1} + a_p^0 B_{i,j}^{n-1}, \tag{3.53}$$

where

$$a_p = a_W + a_E + a_S + a_N + a_P^0$$

$$a_E = a_W = \frac{1}{\Delta x^2}$$

$$a_N = a_S = \frac{1}{\Delta y^2}$$

$$a_P^0 = \frac{\mu_a \sigma_a^*}{\Delta t}.$$

Equation 3.47 is discretized as

$$a_p B_{i,j} = a_E B_{i+1,j} + a_W B_{i-1,j} + a_N B_{i,j+1} + a_S B_{i,j-1} + a_p^0 B_{i,j}^{n-1}, \tag{3.54}$$

where

$$a_p = a_W + a_E + a_S + a_N + a_P^0$$

$$a_E = \frac{h_e}{\mu_f \sigma_f^* \Delta x^2} - \frac{q_{x,i}}{2\Delta x}$$

$$a_W = \frac{h_w}{\mu_f \sigma_f^* \Delta x^2} + \frac{q_{x,i}}{2\Delta x}$$

$$a_N = \frac{1}{\mu_a \sigma_a^* \Delta y}$$

$$a_S = \frac{1}{\mu_r \sigma_r^* \Delta y}$$

$$a_P^0 = \frac{h_i}{\Delta t}.$$

At each time step, equations 3.52, 3.53, and 3.54 are solved iteratively with the alternate direction implicit (ADI) method, which computes this 2D problem in a row-by-row and column-by column manner alternately.

3.2.2.4 EMAG Validation

The EMAG module presented above simplifies the 3D electromagnetic field to a 2D distribution. The accuracy of this approach needs to be investigated and validated. Results from the commercial FEA software COMSOL are chosen to validate the EMAG module. A simple steady conducting model is constructed with the EMAG module in 2D and COMSOL in 3D. In this case, a steady and constant electric current flows through the armature and rails. The resultant current density and magnetic flux density distributions are computed and compared.

COMSOL employs the complete Maxwell's equations to compute the electromagnetic field. Therefore the air that surrounds the armature and rails must be included in the computation domain as a magnetic conductor. As shown in Figure 3.9, the armature (in green) and two rails (in blue) are surrounded by a cylindrical block (only frame shown) which represents the air. We neglect the pocket in this electromagnetic analysis because results are insensitive to it according to preliminary simulations.

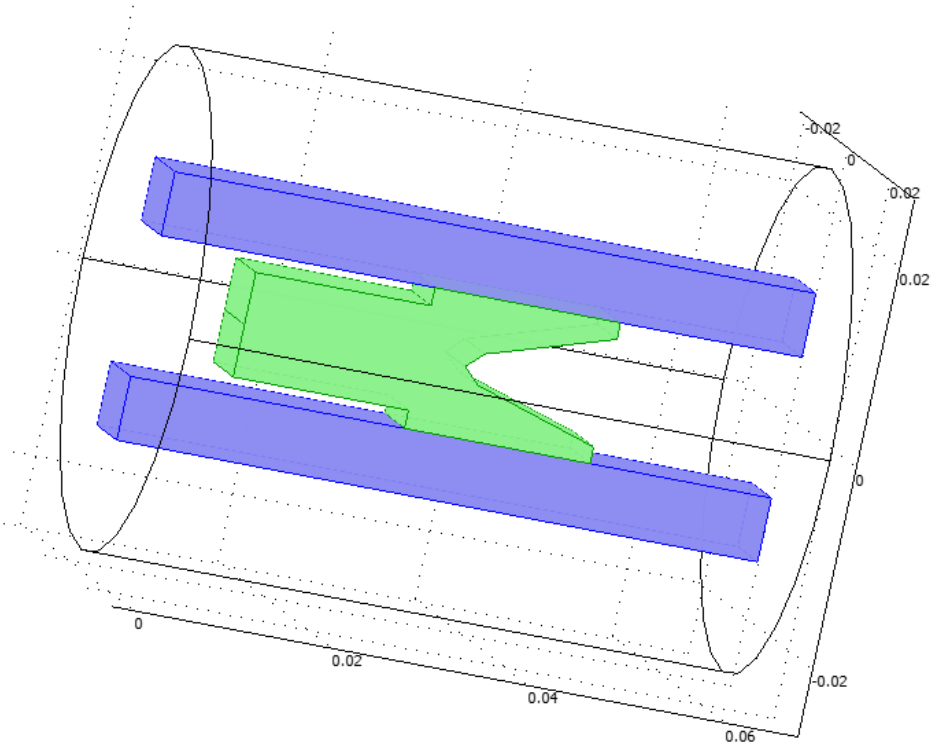

Figure 3.9 3D modeling of the armature and rail configuration in COMSOL

Two 3D modules are implemented and coupled in COMSOL, i.e. Conductive Media DC (*emdc*) for electric current distribution and Magnetostatics (*emqa*) for induced magnetic field. All the boundaries in the *emdc* module are set to be electrical insulation except that a specified inflow electric current density and ground condition are applied on the boundary cross sections of the two rails. Perfect contact and continuity are assumed at the armature-rail interface. Electric current distribution calculated from the *emdc* module is imported into the *emqa* module as an external current. Magnetic insulation is applied to all *emqa* boundaries. The EMAG module in this study follows the computational scheme described in the previous section. The electromagnetic properties of the materials are given in Table 3.1.

Table 3.1 Electromagnetic Properties of the Materials (Ghassemi and Barsi, 2004)

	Armature	**Rail**	**Air**
Material	Aluminum	Copper	Air
Electrical conductivity (S/m)	3.21×10^{7}	4.41×10^{7}	0
Magnetic permeability (N/A^2)	1.2567×10^{-6}	1.2567×10^{-6}	1.2567×10^{-6}

Figure 3.10 shows the distribution of the magnetic flux component that is normal to the shown plane from both COMSOL and the EMAG module in this study. In the COMSOL results, the air is included in the solution and the magnetic field in the air is also generated; in the EMAG results, the air is not included in the model and the magnetic field in the air is not calculated. COMSOL predicts a negative magnetic flux on the outer surfaces of the rails, while in our EMAG module, the magnetic flux density is set to be zero as a boundary condition. Nevertheless, the magnetic field distribution generated by the EMAG module shows good agreements with COMSOL results, especially inside the armature.

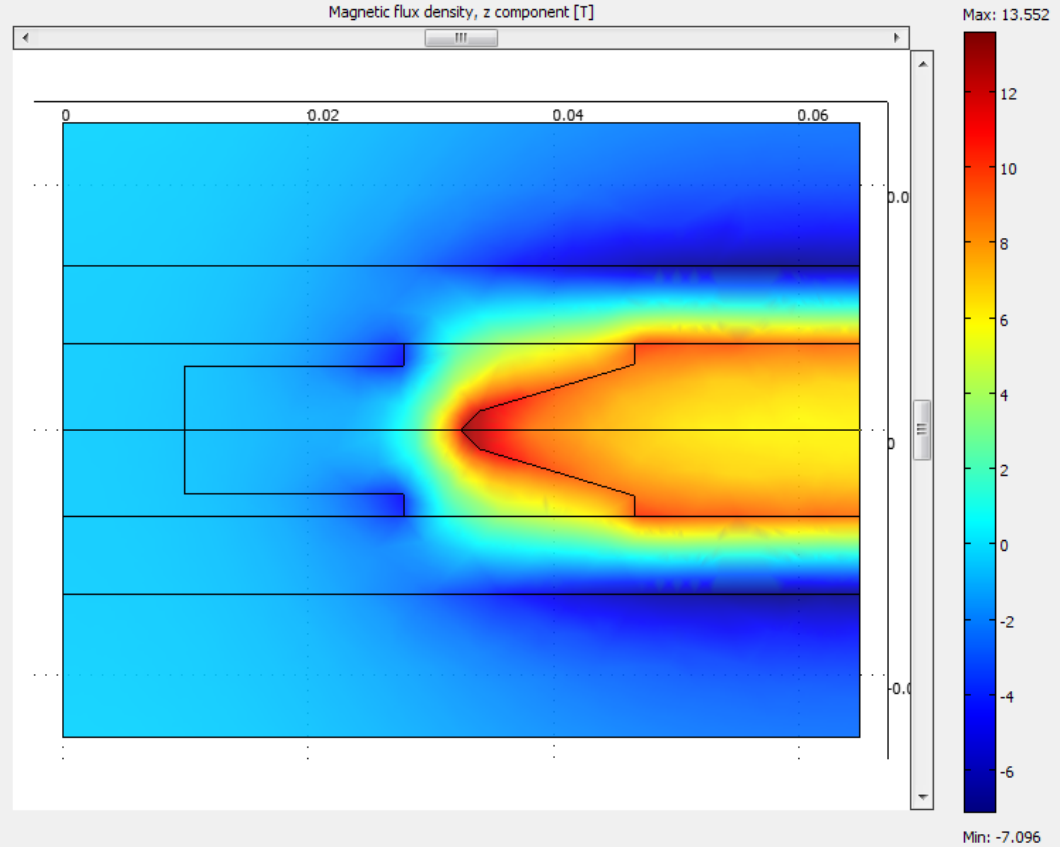

(a)

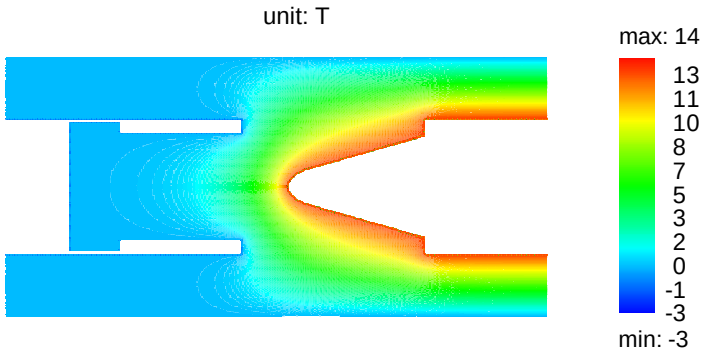

(b)

Figure 3.10 *z* direction magnetic flux component density distribution in (a) COMSOL and (b) this study

The electric current distributions generated from both approaches are given in Figure 3.11, with arrows showing current direction, and contour colors and arrow length representing its magnitude. Both approaches produce similar current patterns, while the EMAG module predicts a smaller current. In both results, large current density is observed at the corners in the armature.

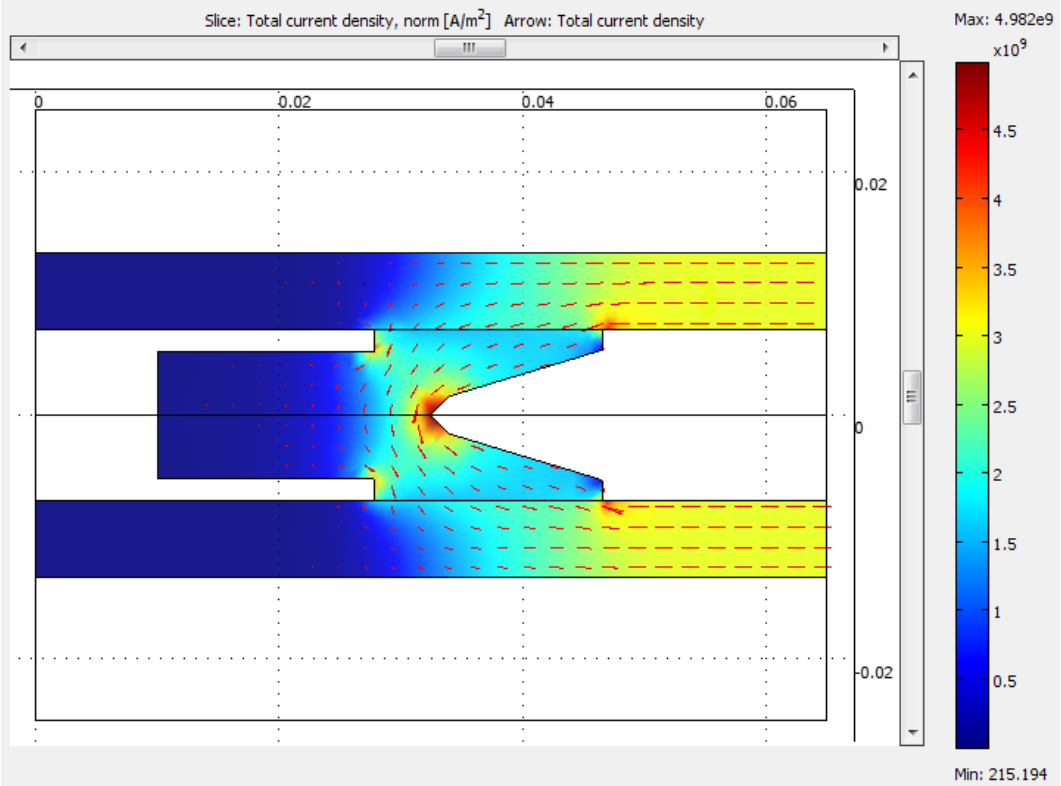

(a)

Figure 3.11 Electric current distribution in a) COMSOL and b) this study

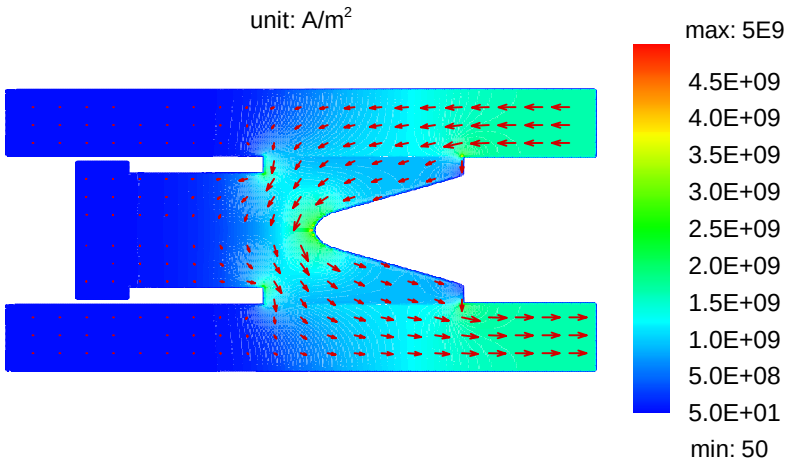

(b)

Figure 3.11 continued

As mentioned earlier, the EMAG module in this study assumes that the magnetic field is dominant in the *z* direction by neglecting the *x* and *y* components. To validate this assumption, the density of the *x* and *y* direction magnetic flux components from COMSOL is shown in Figure 3.12. The magnitude of these two components is at least two orders less than the *z* component, which means that our previous assumption is quite acceptable.

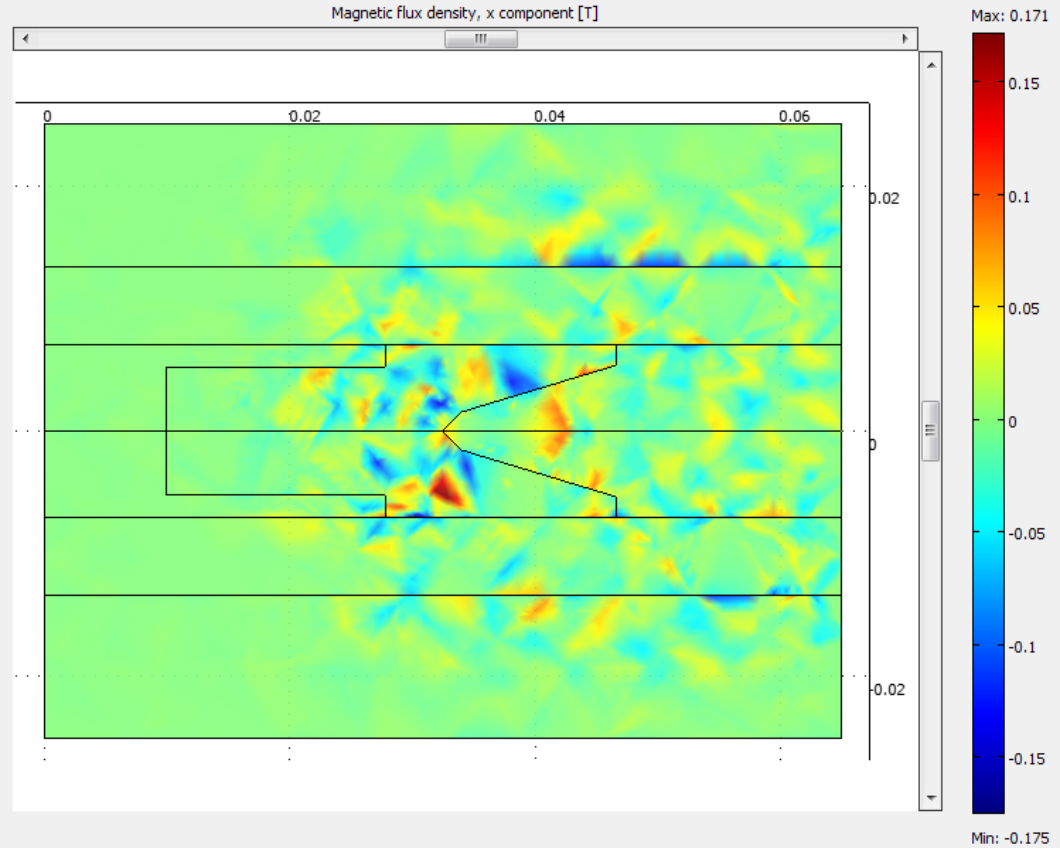

(a)

Figure 3.12 Magnetic flux component density distribution: (a) longitudinal, (b) vertical

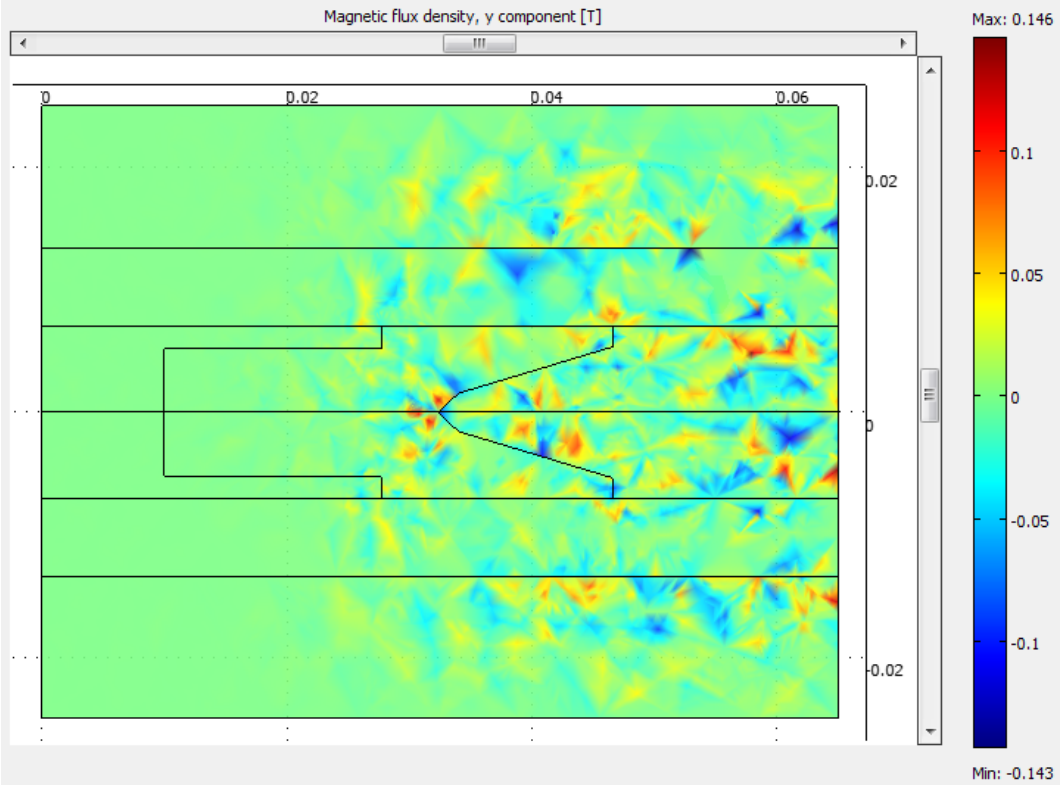

(b)

Figure 3.12 continued

In conclusion, in comparison with the COMSOL results for a static electromagnetic conducting model, the EMAG module developed in this study demonstrates good accuracy. Furthermore, this EMAG model has the capacity to consider the velocity term with a moving armature, which is not available in COMSOL. Such a capability is very important for EML applications because the extremely high velocity found in EML systems has a significant influence on the electromagnetic field distribution (the velocity skin effect) as stated in Section 2.2. Because of this, the EMAG model in this study is a better choice over commercial software, such as COMSOL, for EML simulations.

3.2.3 Contact and Deformation

3.2.3.1 Governing Equations

The armature leg deforms during a launch by contact force, magnetic lateral force and fluid pressure. This deformation changes the armature-rail interface gap shape and influences the lubrication process in return. Such contact and deformation can be computed by finite element analysis with commercial software, such as ANSYS. However, such an FEA process takes considerable computation time and is hard to integrate into the coupled analysis with the other modules developed in this study. The armature leg is very similar to a cantilever beam with one end bonded to the armature body and one end free to deform. Therefore, an alternative method is adopted, and the armature leg is modeled as a cantilever beam, as in Figure 3.13, with the Euler-Bernoulli equation:

$$-\frac{d^2}{dx^2}\left(EI^*(x)\frac{d^2v^*(x)}{dx^2} \right) = w(x). \tag{3.55}$$

where v^* is the deflection, w the distributed load and the moment of inertia is calculated by $I^*(x) = \frac{bh(x)^3}{12}$. The boundary conditions for this cantilever are: $v^*=0$ at $x=0$ and $v^{*\prime}=0$ at $x=0$. Deformation of the rail is neglected because the rail is much stiffer than the armature and is also well supported.

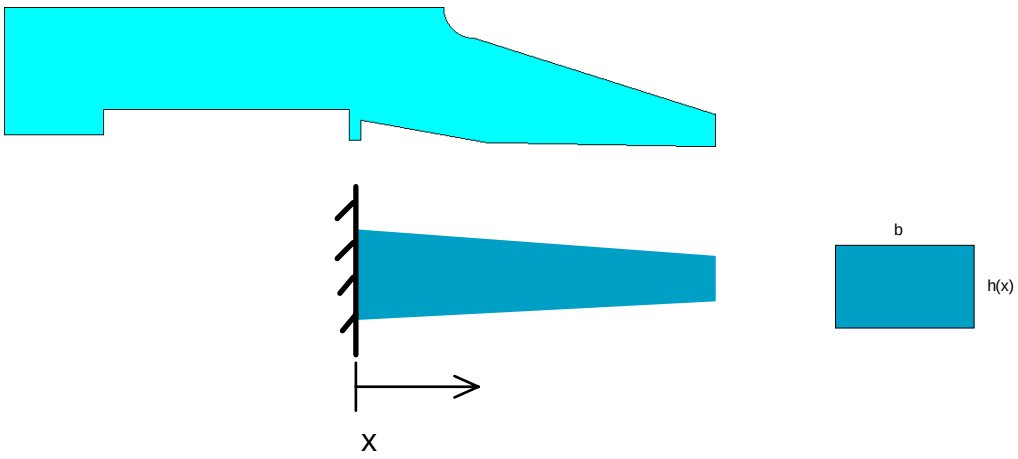

Figure 3.13 The beam approximation of the armature leg

Asperity contact occurs at the contact region of the rail surface and the armature surface. The Greenwood-Williamson contact model is used to calculate contact and a Gaussian distribution of asperities is assumed. The contact pressure is then given by

$$p_{cont} = \frac{4}{3}\frac{E\hat{\sigma}^{3/2}}{\left(1-\nu^{*2}\right)}I' . \tag{3.56}$$

The integral I^* is evaluated as

$$\begin{aligned} I' &= \frac{1}{\sqrt{2\pi}}\int_H^\infty \left(z-H\right)^{3/2} e^{-z^2/2}dz \\ &\approx \exp\left(-0.1973H^2 - 0.4199H + 0.4929\right) \end{aligned} . \tag{3.57}$$

3.2.3.2 Computational Scheme

The Euler cantilever is solved by integrating the bending-moment equation. As in Figure 3.14, the distributed force *w(x)* on the armature leg, which could be the fluid force, magnetic force and contact force, is integrated and combined with the concentrated force $F_0(x)$ (if any) to obtain the shear force $F(x)$ within the beam (equation 3.59). The shear force $F(x)$ is then integrated again to obtain the bending moment $M(x)$ in the beam. The bending moment is a function of the second derivative of the beam deflection $v^*(x)$ (equation 3.60). Equation 3.60 is then integrated twice to obtain the deflection slope $v^{*\prime}(x)$ and the deflection $v^*(x)$ of the beam (equations 3.61 and 3.62).

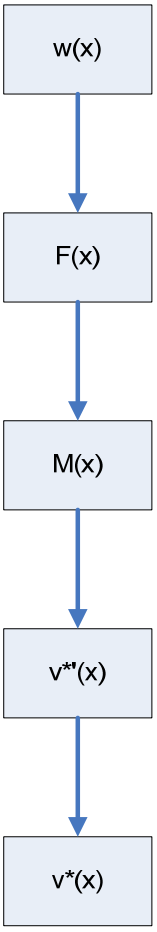

$$w(x) = -\frac{d^2}{dx^2}\left(EI^*(x)\frac{d^2v^*(x)}{dx^2} \right) \tag{3.58}$$

$$F(x) = F_0(x) + \int -w(x)dx = \frac{d}{dx}\left(EI^*(x)\frac{d^2v^*(x)}{dx^2} \right) \tag{3.59}$$

$$M(x) = \int F(x)dx = EI^*(x)\frac{d^2v^*(x)}{dx^2} \tag{3.60}$$

$$v^{*\prime}(x) = \frac{dv^*(x)}{dx} = \int \frac{M(x)}{EI^*(x)}dx \tag{3.61}$$

$$v^*(x) = \int v^{*\prime}(x)dx \tag{3.62}$$

Figure 3.14 Procedure to calculate beam deflection

The contact module in this study proceeds in a surface approaching manner with a predictor-corrector method. As depicted in Figure 3.15, the armature and the rail are initially apart from each other without any interference (Figure 3.15a). The armature is fixed and the rail gradually moves towards the armature with incremental spatial steps. At the point that the minimum distance between the rail surface and the armature surface falls into the Hertzian contact regime, the corresponding contact pressure is calculated using the Greenwood-Williamson asperity contact model (Figure 3.15b). Armature deformation is then calculated with this contact pressure and the surface interference is updated. A new contact status is formed and the program iterates until equilibrium is achieved (Figure 3.15c) and the rail moves to the next spatial step until the desired final spacing between the rail and the armature is reached. The flowchart of this contact analysis is shown in Figure 3.16.

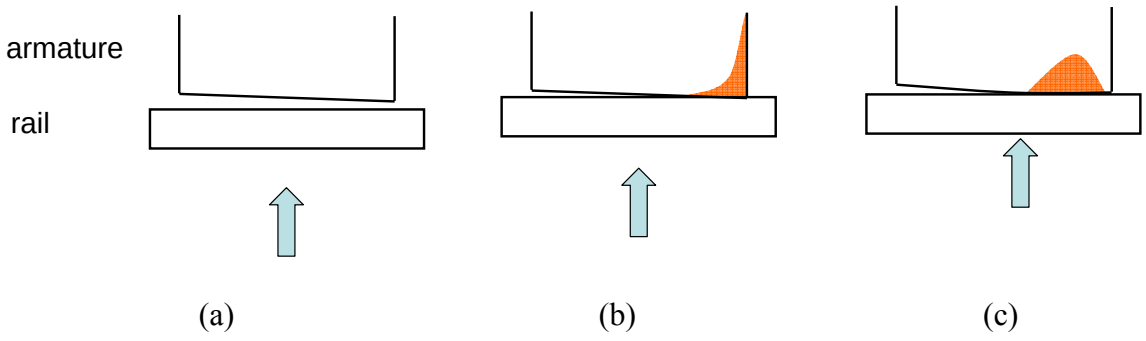

Figure 3.15 Schematic of the contact model

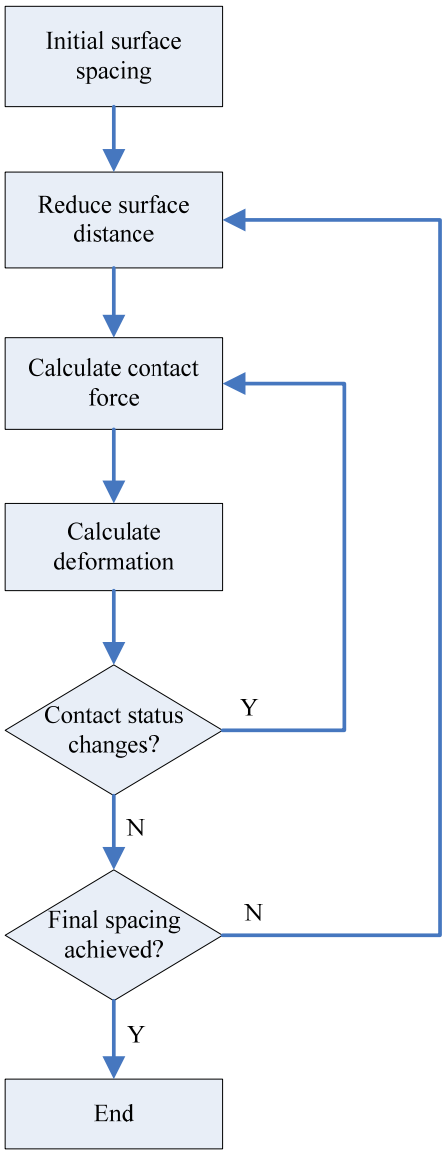

Figure 3.16 Flowchart of contact computation

3.2.3.3 Deflection Validation

A point force deflection model is used to validate the deformation code. Various forces are applied at the tip of the armature leg and the corresponding deformation is

calculated with the beam deformation model and FEA software -- ANSYS. As shown in Figure 3.17, only half of the symmetric geometry is modeled. The loading and boundary conditions in ANSYS are as follows:

1. The centerline of the armature is fixed by defining zero displacement in *x* and *y* direction (UX and UY equal zero).
2. The left side of the armature is fixed in UX to prevent longitudinal motion.
3. A nodal force on the armature leg tip.

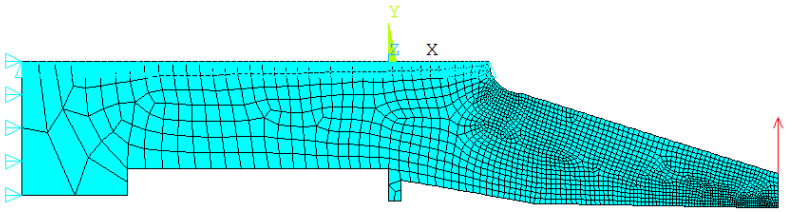

Figure 3.17 Schematic of the deformation model in ANSYS

The properties of the armature are given in Table 3.2. The high order 2-D, 8-node rectangular plane element PLANE183 (Figure 3.18) is employed with plane strain option. Mesh density is manually specified to ensure a fine mesh at the armature leg, especially at the tip where contact happens. A mesh convergence study was first conducted to find the optimal mesh density. In the final configuration, 1932 elements are meshed in the armature.

Table 3.2 Material Properties and Element Type of the Armature

	Armature
Material	Aluminum
Young's modulus	70 GPa
Poisson's ratio	0.33
Element type	PLANE183

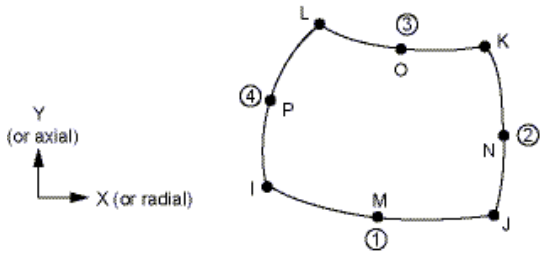

Figure 3.18 Schematic of the 2-D, 8-node rectangular PLANE 183 element

A typical ANSYS deformation result is shown in Figure 3.19. The displacement in any vertical cross section of the armature leg is uniform, which agrees with the Euler beam assumption. Since the armature leg is not an ideal cantilever, an equivalent moment of inertia is found for the armature leg by comparing the deflection at the armature leg tip as a function of the bending force with the ANSYS results. Comparison of the armature leg's lower surface displacement from both the ANSYS model and the Euler beam approximation with various forces is given in Figure 3.20. Table 3.3 lists the deflections of the armature leg tip. Results show that the Euler beam approximation not only provides a good prediction of the armature tip deflection, but also generates a very accurate deformation curve along the lower surface.

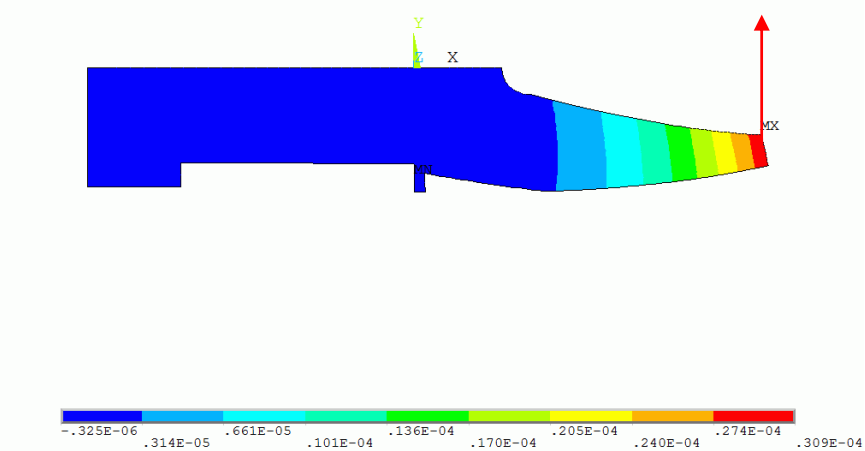

Figure 3.19 Armature deformation in ANSYS with a 100 N bending force

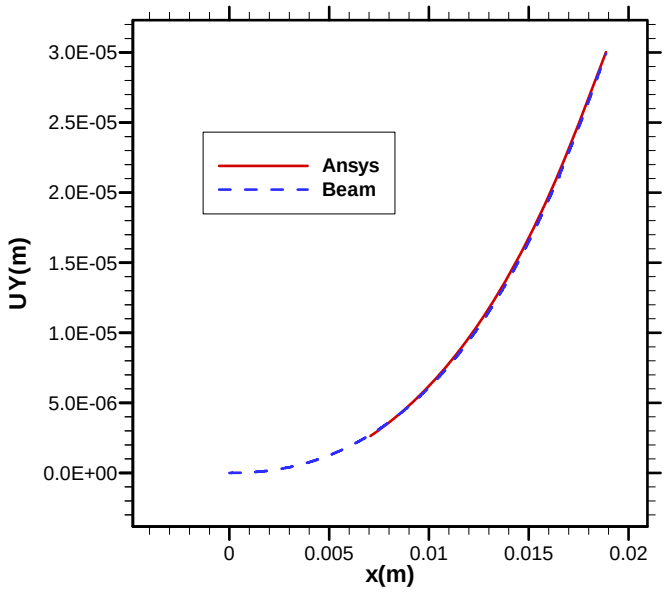

(a)

Figure 3.20 Comparison of armature leg displacement in ANSYS and beam model with a bending force of (a) 100 N, (b) 200 N, (c) 500 N and (d) 1000 N.

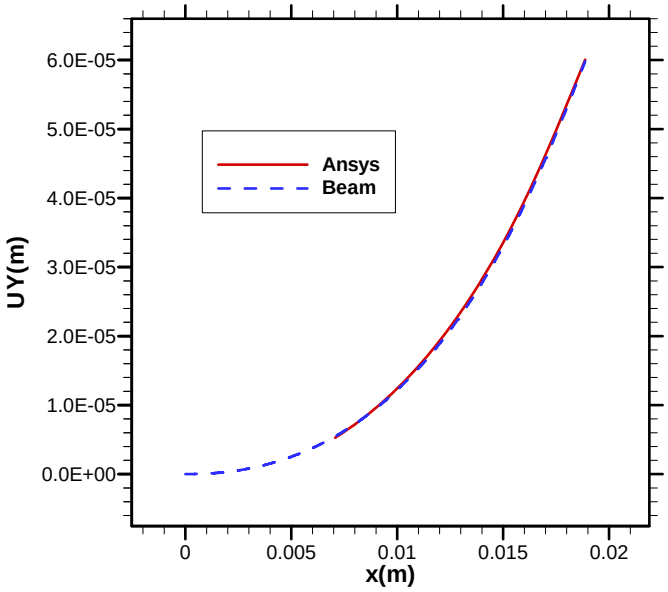

(b)

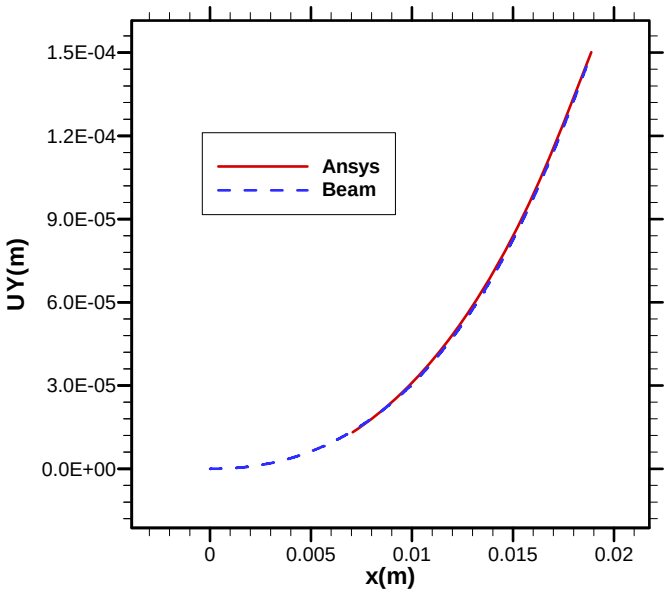

(c)

Figure 3.20 continued

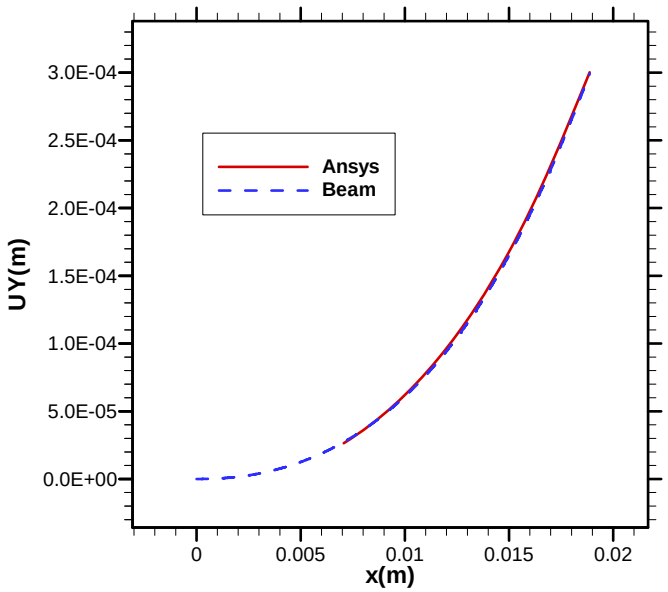

(d)

Figure 3.20 continued

Table 3.3 Comparison of Armature Leg Tip Deflection

Force (N)	Deflection		
	ANSYS (m)	Euler Beam (m)	Difference
100	2.99E-5	2.98E-5	0.33%
200	6.00E-5	5.98E-5	0.33%
500	1.50E-4	1.49E-4	0.67%
1000	3.00E-4	2.99E-4	0.33%

3.2.3.4 Contact Validation

The contact algorithm is also validated with an ANSYS contact analysis. Similar to the deformation analysis, only half of the geometry is modeled in ANSYS (Figure 3.21). The rail is set apart from the armature at the beginning. Then a displacement condition is

applied on the rail based on the final spacing between the two rails. The loading and boundary conditions in ANSYS are as follows:

1. The centerline of the armature is fixed by defining zero UX and UY.
2. The lower rail is fixed in UX and has a displacement UY so that the desired final rail spacing is achieved.
3. The left side of the armature is fixed in UX to prevent longitudinal motion.
4. The armature surface and the rail surface at the interface are defined as a contact pair. The rail surface is specified to be the target surface as a rigid body. The armature surface is chosen to be the contact surface, allowing deformation.

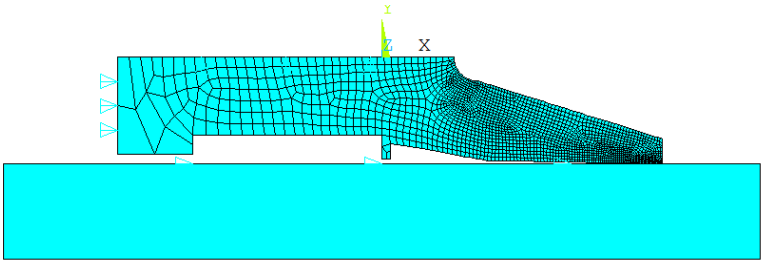

Figure 3.21 Schematic of the contact model in ANSYS

The material properties and contact element used in ANSYS are given in Table 3.4. PLANE183 is still chosen for the structure and stress analysis. Surface to surface contact is defined and the 2-D contact elements TARGE169 and CONTA172 (Figure 3.22) are selected for the target surface (rail) and the contact surface (armature), respectively. It must be noted that ANSYS does not consider asperity contact and that interface clearance at the contact region cannot be extracted from ANSYS results.

Table 3.4 Material Properties and Element Types in ANSYS Contact Analysis

	Armature	**Rail**
Material	Aluminum	Copper
Young's modulus	70 GPa	120 GPa
Poisson's ratio	0.33	0.33
Element type	PLANE183	PLANE183
Contact type	CONTACT	TARGET
Contact element	CONTA172	TARGE169

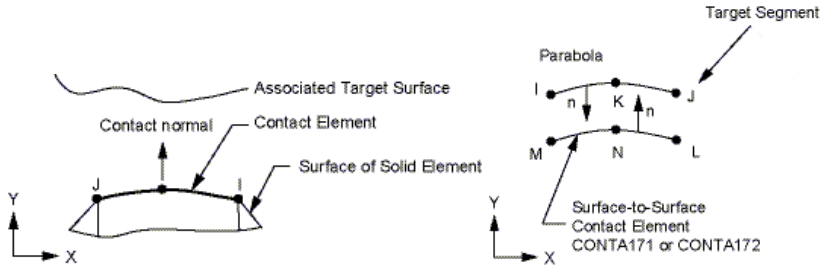

Figure 3.22 Relationship of the target and contact elements in ANSYS

Figures 3.23 and 3.24 show a typical contact solution from ANSYS with the interference of the armature and the rail surfaces to be 76.2 μm, which corresponds to a final rail spacing of 14.1 mm (0.555 inch). In this solution, contact occurs over a very small area at the tip of the armature (Figure 3.23). The maximum contact pressure is about 40 MPa, which is far below the yield strength of aluminum. Therefore, the elastic assumption in the Greenwood-Williamson contact model is appropriate. In the displacement distribution shown in Figure 3.24, the vertical displacement in the armature is still uniform in the *y* direction, which agrees with our Euler beam assumption in the deformation module.

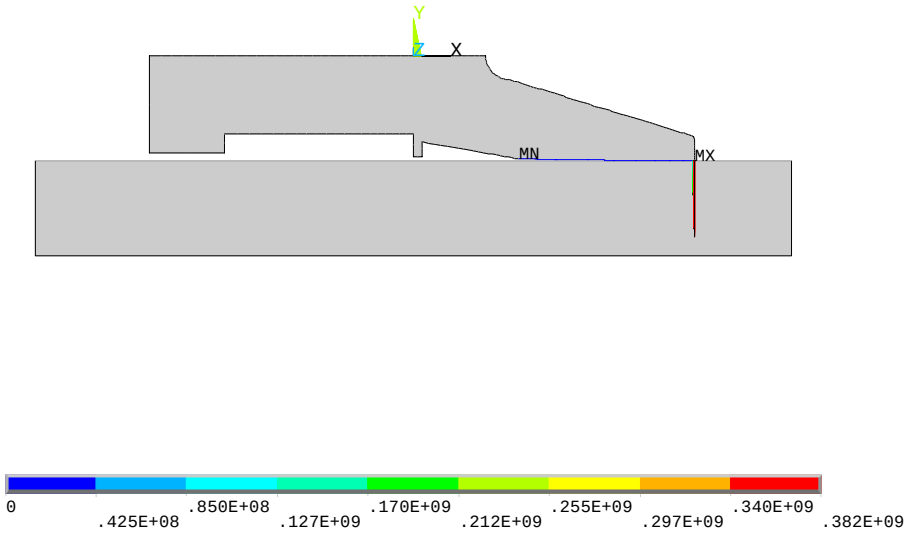

Figure 3.23 Contact pressure distribution in ANSYS

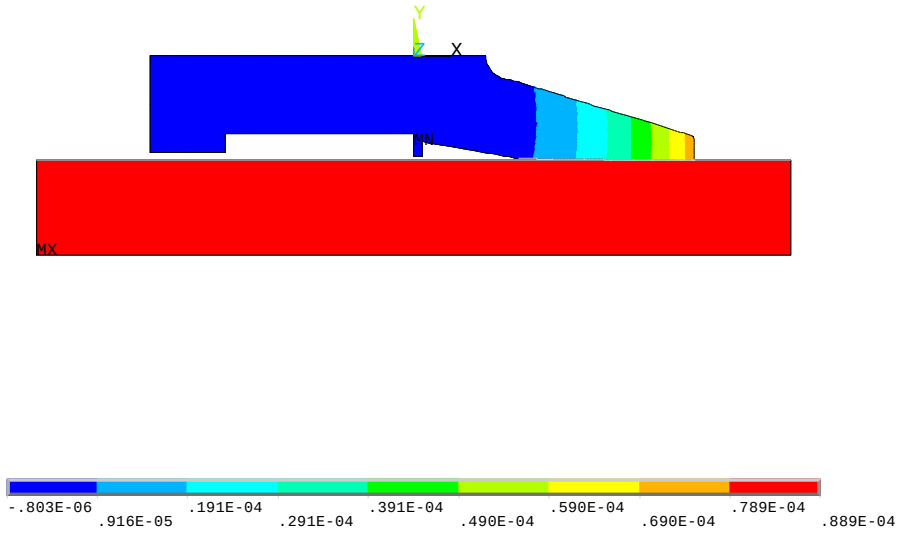

Figure 3.24 Vertical displacement (UY) distribution in ANSYS

A series of simulations have been performed in both ANSYS and the contact module, with the surface interference increased from 76.2 μm, to 139.7 μm and 203.2 μm, by reducing the spacing between the two rails. The resultant contact pressure distribution

is compared in Figure 3.25. With an increasing surface interference, the contact region area grows. With a surface interference of 203.2 μm, both solutions predict a forward migration of the contact region. Although both approaches demonstrate similar contact pressure profiles, a deviation exists between the ANSYS results and beam results. In general, the beam model predicts a smaller contact pressure with a larger contact area.

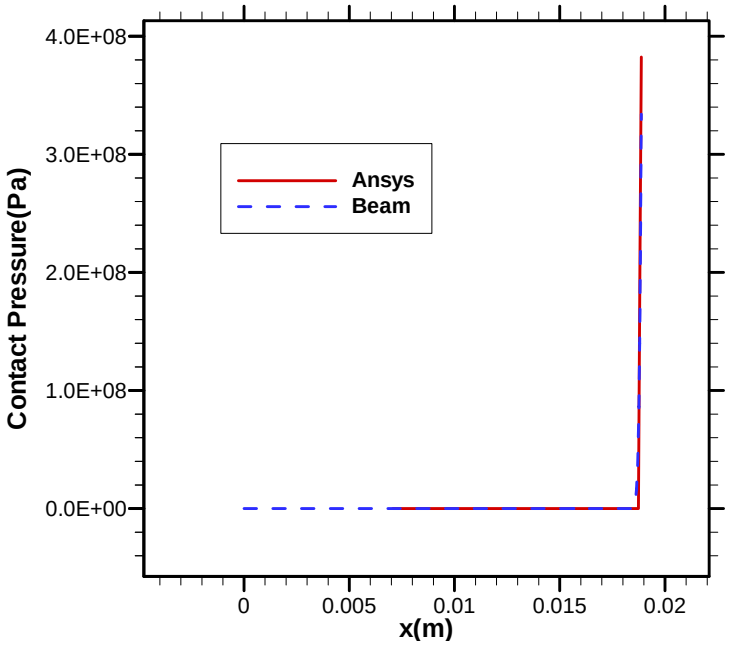

(a)

Figure 3.25 Comparison of contact pressure distributions with different surface interference: (a) 76.2 μm, (b) 139.7 μm, (c) 203.2 μm.

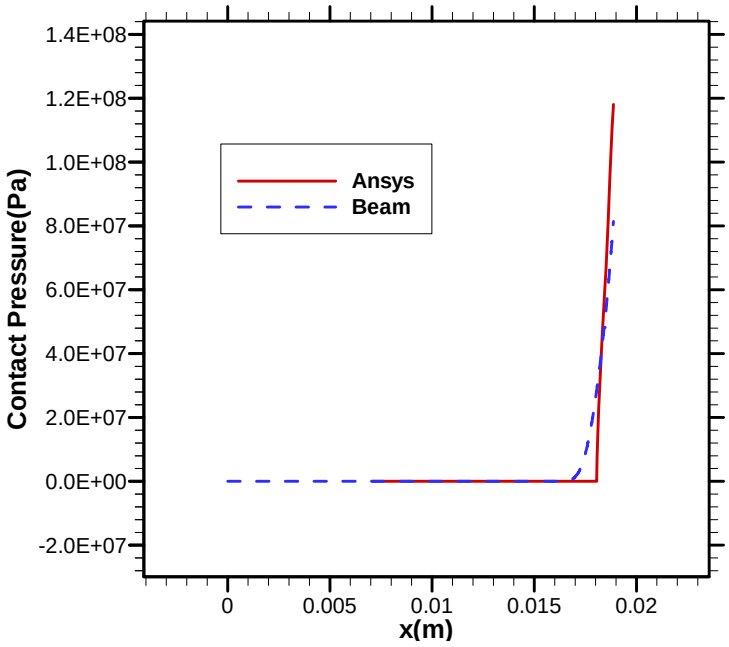

(b)

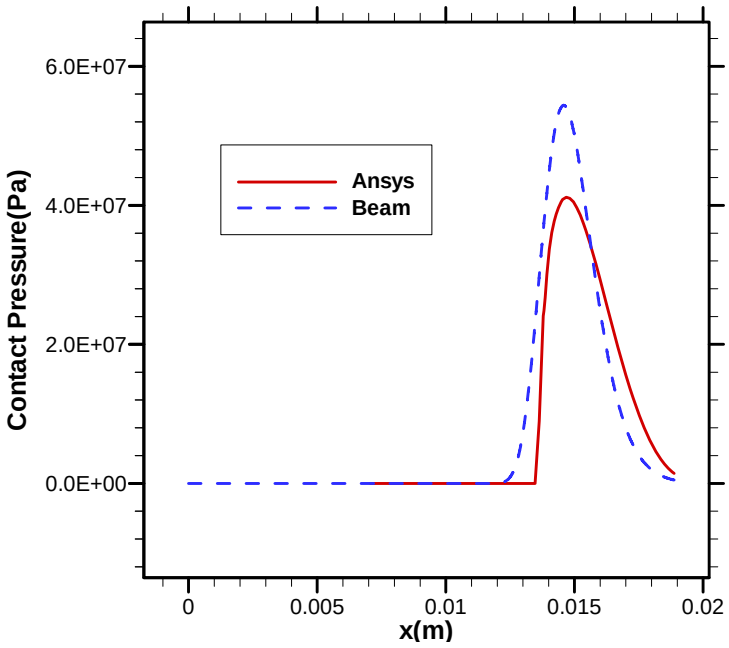

(c)

Figure 3.25 continued

3.2.4 Coupled Analysis and Launch History Prediction

3.2.4.1 Program Flowchart

In this MEHD model, the coupled analysis involves four modules: electromagnetics, contact mechanics, fluid mechanics and deformation mechanics (Figure 3.26). The electromagnetic module calculates the magnetic force in the armature and the magnetic pressure in the fluid. The magnetic force, together with the fluid pressure from the fluid mechanics module and the contact pressure from the contact module, is imported into the deformation module to determine interface deformation. The deformation module then provides the film thickness distribution to the lubrication module and surface interference to the contact module through a feedback process. With updated information, the lubrication module and the contact module regenerate results and the whole process iterates.

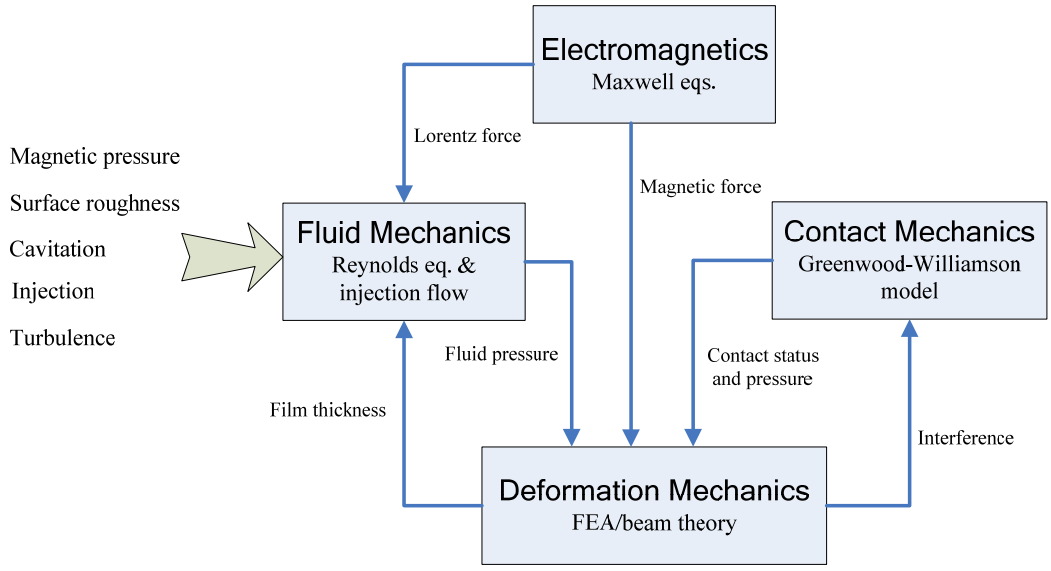

Figure 3.26 Coupled analysis of the MEHD model

When the results in the above coupled analysis converge, computation of the MEHD model for the current time step is finished and the program moves on to the next time step in the launch history simulation, as shown in Figure 3.27.

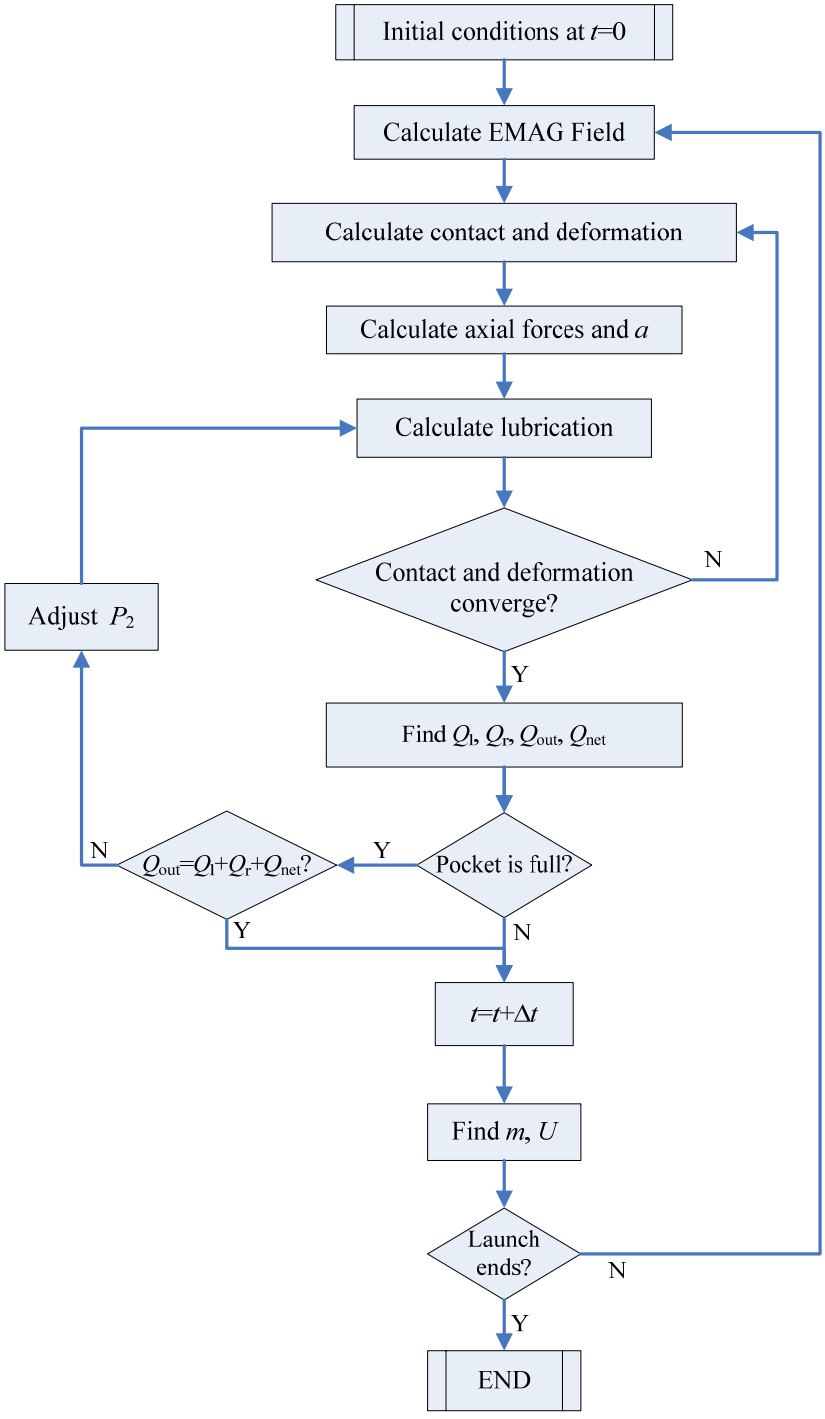

Figure 3.27 Flowchart of launch history prediction with the MEHD model

3.2.4.2 Fluid Cavitation Detection

As mentioned in Section 3.1.2.3, using total pressure to determine fluid cavitation is not accurate. Since the magnetic field distribution is computed in this MEHD model, the magnetic term can be evaluated throughout the whole film. Therefore, it is possible to go back to the original Reynolds equation with the real fluid pressure term, separate the magnetic term, and determine cavitation solely by fluid pressure. The Reynolds equation with the magnetic Lorentz force term is

$$\frac{d}{dx}(\phi_x h^3 \frac{dP}{dx}) = \frac{d}{dx}(\phi_x h^3 \frac{1}{\mu_f} B \frac{dB}{dx}) + 3(2\mu U + \rho a h_T^{\,2}) \frac{\partial h_T}{\partial x} + 6\mu U \sigma \frac{\partial \phi_s}{\partial x}. \quad (3.63)$$

There should be no difference between these two approaches in the situation where the fluid pressure is positive. Figure 3.28 shows the comparison of results by both approaches when the same boundary conditions are applied. The corresponding magnetic pressure and total pressure in the film are also plotted in Figure 3.28b. In this case no cavitation is detected in either approach, and the results are identical. However, since the total pressure approach detects cavitation using the sum of fluid pressure and magnetic pressure, it may fail to predict cavitation even when the fluid pressure is negative. The area of the cavitating region predicted from total pressure will be smaller than the real value. The severity of such error depends on the ratio of fluid pressure to magnetic pressure and it could be negligible if the fluid pressure is dominant.

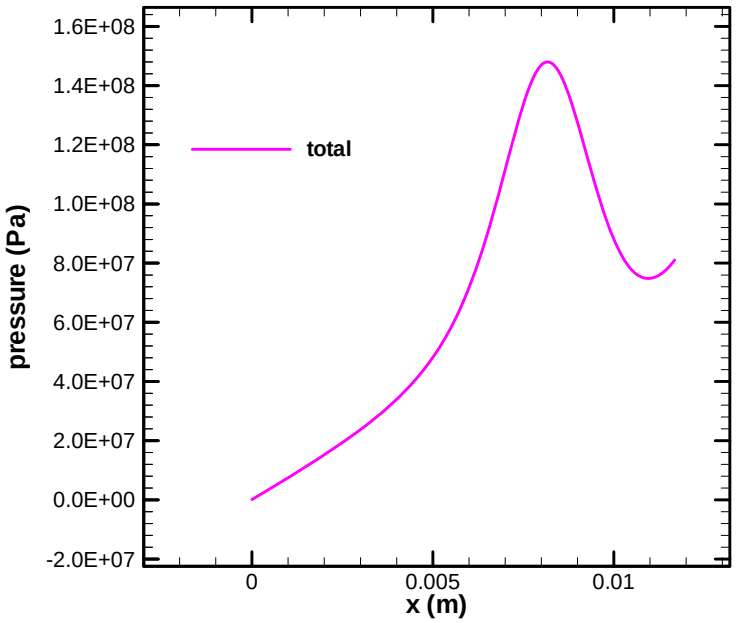

(a)

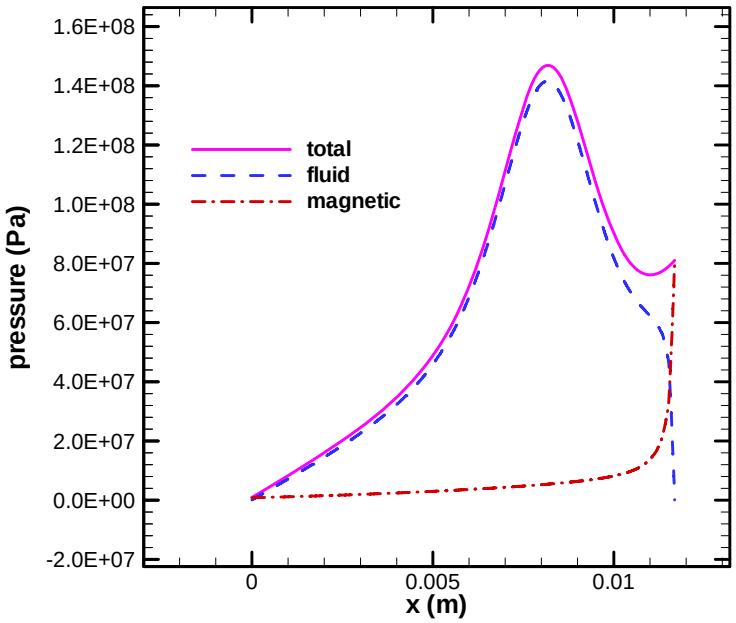

(b)

Figure 3.28 Pressure distribution from (a) total pressure approach and (b) fluid pressure approach

The computation process iterates much faster by solving for the total pressure. Therefore, the Reynolds equation with total pressure is solved initially. As iteration goes on, fluid pressure is regularly checked and once it is found to drop below zero, cavitation is detected and the computational code switches to solve fluid pressure using equation 3.63.

3.2.4.3 Resistive Forces

With the results of interface deformation and contact pressure, it is now possible to analyze the resistive forces that have been neglected earlier. Two major resistive forces act on the armature: the friction force by the contacting surfaces and the viscous shear force by the lubricant.

The friction force only exists at contact regions. It is proportional to the contact pressure as in equation 3.64.

$$F_f = \int f P_{cont} dA \tag{3.64}$$

The coefficient of friction f is a function of contact force, current density and sliding speed (Streator, 2001). The exact relationship is still unknown. f is assumed to be constant with a value of 0.1 in this study.

The viscous force is produced by the velocity gradient in the film close to the armature surface. According to the shear stress factor approach by Patir and Cheng (1979), the shear stress on the armature is calculated by equation 3.65.

$$\tau = \frac{\mu U}{h}\left(\phi_f + \phi_{fs}\right) + \phi_{fp}\frac{h}{2}\frac{\partial P}{\partial x}. \tag{3.65}$$

Considering the acceleration term in the Reynolds equation, equation 3.65 can be modified as

$$\tau = \frac{\mu U}{h}\left(\phi_f + \phi_{fs}\right) + \phi_{fp}\frac{h}{2}\left(\frac{\partial P}{\partial x} - \rho a\right), \tag{3.66}$$

and the viscous force is given by

$$F_v = \int \tau dA. \tag{3.67}$$

The total resistive force is the sum of the friction force and the viscous force, as in equation 3.68:

$$F_{res} = F_f + F_v. \tag{3.68}$$

The driving magnetic body force, calculated in equation 3.2, and this resistive force F_{res} are added together to determine the total longitudinal force on the armature (F_{total}) by equation 3.69. Such longitudinal force produces the acceleration (equation 3.70) of the armature and can be used to replace the *L'* hypothesis which neglected the resistive forces in equation 3.34.

$$F_{total} = F_{emag} - F_{res} = \int_V f_x dV - F_{res} \tag{3.69}$$

$$a = \frac{F_{total}}{m} \tag{3.70}$$

3.2.4.4 Squeeze Film Effect

Once interface deformation is introduced to the coupled analysis as in the MEHD model in this section and the final METHD model in next section, a squeeze film term must be included in the Reynolds equation to count for the transient film thickness variation, as in equation 3.71 for the dimensional form and equation 3.72 for the nondimensional form:

$$\frac{d}{dx}(\phi_x h^3 \frac{dP}{dx}) = 3(2\mu U + \rho a h_T{}^2)\frac{\partial h_T}{\partial x} + 6\mu U\sigma \frac{\partial \phi_s}{\partial x} + 12\mu \frac{\partial h_T}{\partial t}, \tag{3.71}$$

$$\frac{\partial}{\partial \bar{x}}(\frac{\phi_x \bar{h}^3}{K_T}\frac{\partial \Phi F}{\partial \bar{x}}) = \Omega \frac{\partial}{\partial \bar{x}}\left(\frac{G^2 \bar{h}_T^3}{K_T}\right) + 6\beta \frac{\partial G\bar{h}_T}{\partial \bar{x}} + 6\beta \frac{\partial G\bar{\sigma}\bar{\phi}_s}{\partial \bar{x}} + 12\delta(x)\beta\zeta\bar{V} + 12\beta\lambda \frac{\partial G\bar{h}_T}{\partial \bar{t}}. \tag{3.72}$$

where $\lambda = \frac{L}{Ut_0}$, t_0 is the reference time.

3.3 Magneto-elastothermohydrodynamic Model

3.3.1 Objective

The objective of the METHD model is to consider temperature change in the armature-rail system and the resultant thermal deformation in the armature caused by joule heating, frictional heating, and viscous heating. Such thermal effects are coupled with the other modules to construct a complete analytical description of the armature-rail behavior.

3.3.2 Thermal Analysis

3.3.2.1 Governing Equations

The electric current flowing through the EML system introduces considerable joule heating. Friction and viscous effects at the armature-rail interface generate frictional and viscous heating. These heat sources raise the temperature in the armature, the rail and the lubricant. Temperature-dependent material properties, such as electrical conductivity, are changed by such temperature rise. The temperature gradient inside the armature also produces thermal deformation.

Like the EMAG module developed in this research, the temperature field is approximated by a 2D model. The transient heat diffusion equations with joule heating and viscous heating sources are:

$$\rho_r c_r \left(\frac{\partial T_r}{\partial t} + U \frac{\partial T_r}{\partial x} \right) = k_r \left(\frac{\partial^2 T_r}{\partial x^2} + \frac{\partial^2 T_r}{\partial y^2} \right) + \frac{J^2}{\sigma_r} \tag{3.73}$$

$$\rho_a c_a \frac{\partial T_a}{\partial t} = k_a \left(\frac{\partial^2 T_a}{\partial x^2} + \frac{\partial^2 T_a}{\partial y^2} \right) + \frac{J^2}{\sigma_a} \tag{3.74}$$

$$\rho_f c_f \left(\frac{\partial T_f}{\partial t} + u(y) \frac{\partial T_f}{\partial x} \right) = k_f \left(\frac{\partial^2 T_f}{\partial x^2} + \frac{\partial^2 T_f}{\partial y^2} \right) + \frac{J^2}{\sigma_f} + \dot{q} \tag{3.75}$$

where $\dot{q}$ is the viscous heat generation defined by equation 3.28.

The armature is composed of aluminum with a melting point of 650 ^{o}C. Preliminary tests show that only a very tiny spot in the armature may reach this point. No obvious melting is observed in experiments. Therefore, the temperature at this tiny melting spot is limited to the melting temperature of Aluminum, and phase change is neglected in this study.

At the contact region, frictional heating is generated by the relative motion of the armature and the rail. It is proportional to the relative speed and contact pressure, as in equation 3.76.

$$\dot{q}_f = fUP_{cont} \tag{3.76}$$

Integrating equation 3.75 in the film yields:

$$\begin{aligned} &\rho_f c_f \left(h(x) \frac{\partial T_f}{\partial t} + Q \frac{\partial T_f}{\partial x} \right) \\ &= k_a \frac{\partial T_a}{\partial y} - k_r \frac{\partial T_r}{\partial y} + h \frac{\partial^2 T_f}{\partial x^2} + h \frac{J^2}{\sigma_f} + \int_0^h \dot{q} dy + \delta(x) fUP_{cont} \end{aligned} \tag{3.77}$$

where $\delta(x) = \begin{cases} 1 & \text{at contact} \\ 0 & \text{no contact} \end{cases}$.

In this thermal analysis, lubricant viscosity, material specific heat capacity, and electrical conductivity are functions of temperature. Their temperature dependency is listed in Table 3.5. Other properties, such as density (unit: kg/m^3), are insensitive to temperature (unit: ^{o}C) and treated as constants.

Table 3.5 Temperature Dependent Material Properties (Ghassemi and Barsi, 2004)

Property	**Rail (Copper)**	**Armature (Aluminum)**	**Film (Gallium)**
σ^* (Mho/m)	$\frac{4.41\times10^7}{1+0.0039(T-27)}$	$\frac{3.21\times10^7}{1+0.0039(T-27)}$	5.75×10^6
C (J/(Kg-^{o}C))	$0.0987(T+273)+355$	$0.486(T+273)+766$	371
μ (Pa-s)	___	___	$2.468\times10^{-4}\rho^{\frac{1}{3}}e^{\frac{79.05\rho}{T+273}}$

3.3.2.2 Computational Scheme

Similarly to the EMAG module, equations 3.73, 3.74 and 3.77 are discretized to finite volume forms. The FVM formula of equation 3.73 is

$$a_p T_{i,j} = a_E T_{i+1,j} + a_W T_{i-1,j} + a_N T_{i,j+1} + a_S T_{i,j-1} + a_p^0 T_{i,j}^{n-1} + S\,, \tag{3.78}$$

where

$$a_p = a_W + a_E + a_S + a_N + a_P^0$$

$$a_E = \frac{k_r}{\Delta x^2} - \frac{\rho_r c_r U}{2\Delta x}$$

$$a_W = \frac{k_r}{\Delta x^2} + \frac{\rho_r c_r U}{2\Delta x}$$

$$a_N = a_S = \frac{k_r}{\Delta y^2}$$

$$a_P^0 = \frac{\rho_r c_r}{\Delta t}$$

$$S = \frac{J_i^2}{\sigma_r^*}.$$

Similarly, equation 3.74 is discretized as

$$a_p T_{i,j} = a_E T_{i+1,j} + a_W T_{i-1,j} + a_N T_{i,j+1} + a_S T_{i,j-1} + a_p^0 T_{i,j}^{n-1} + S\,, \tag{3.79}$$

where

$$a_p = a_W + a_E + a_S + a_N + a_P^0$$

$$a_E = a_W = \frac{k_a}{\Delta x^2}$$

$$a_N = a_S = \frac{k_a}{\Delta y^2}$$

$$a_P^0 = \frac{\rho_a c_a}{\Delta t}$$

$$S = \frac{J_i^2}{\sigma_a^*}$$

Assuming no temperature difference exists at the armature-fluid and rail-fluid boundaries, equation 3.77 is discretized as

$$a_p T_{i,j} = a_E T_{i+1,j} + a_W T_{i-1,j} + a_N T_{i,j+1} + a_S T_{i,j-1} + a_p^0 T_{i,j}^{n-1} + S\,, \tag{3.80}$$

where

$$a_p = a_W + a_E + a_S + a_N + a_P^0$$

$$a_E = \frac{h_e k_f}{\Delta x^2} - \frac{\rho_f c_f Q_i}{2\Delta x}$$

$$a_W = \frac{h_w k_f}{\Delta x^2} + \frac{\rho_f c_f Q_i}{2\Delta x}$$

$$a_N = \frac{k_a}{\Delta y}$$

$$a_S = \frac{k_r}{\Delta y}$$

$$a_P^0 = \frac{\rho_f c_f h_i}{\Delta t}$$

$$S = h_i \frac{J_i^2}{\sigma_f^*} + \int_0^h \dot{q} dy + \delta(x) f U P_{cont}$$

At each time step, equations 3.78, 3.79, and 3.80 are also solved iteratively with the alternating direction implicit (ADI) method. The values of the temperature-dependent material properties are updated after each iteration.

3.3.2.3 Thermal Deformation

The armature expands and deforms with temperature. A thermal bending beam model is employed in this study to account for such deformation. A thermal moment M_T can be derived from the uneven temperature field as in equation 3.81.

$$M_T = \int_A \alpha ETydA \tag{3.81}$$

This thermal moment produces a thermal deflection similar to a force moment, as shown in equation 3.82. Such thermal deflection is combined with the force deflection calculated in the Euler beam model to compute the total deformation.

$$\frac{d^2 v^*(x)}{dx^2} = -\frac{M_T}{EI^*} \tag{3.82}$$

3.3.2.4 Thermal Validation

This thermal module is validated with ANSYS by comparing the temperature distribution and thermal deformation for a simple heat conduction problem. As shown in Figure 3.29, the inner boundary of the armature leg is set to be under a high temperature T_h. All the other boundaries are set to be room temperature (20 ^oC) except the centerline, which is set to be a symmetric boundary.

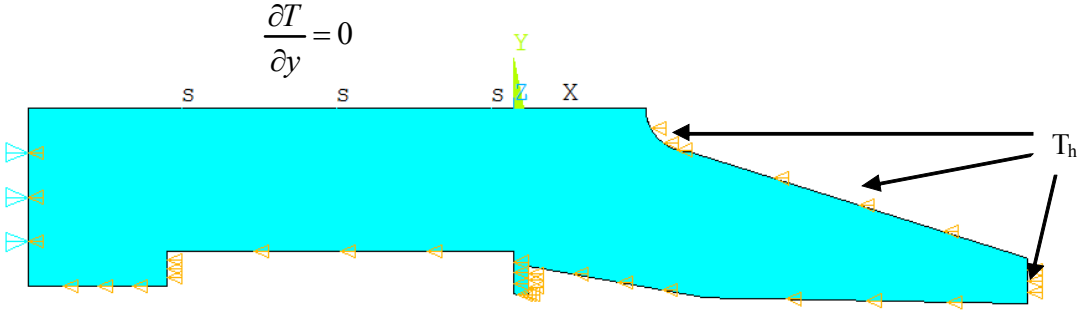

Figure 3.29 Boundary conditions of the thermal model in ANSYS

The armature is meshed by rectangular PLANE13 elements, shown in Figure 3.30, which have a 2-D magnetic, thermal, electrical, piezoelectric, and structural field capability with limited coupling between the fields. The same mesh strategy used in Section 3.2 is applied to this analysis to produce a fine mesh in the armature leg. 1881 elements are generated in this module.

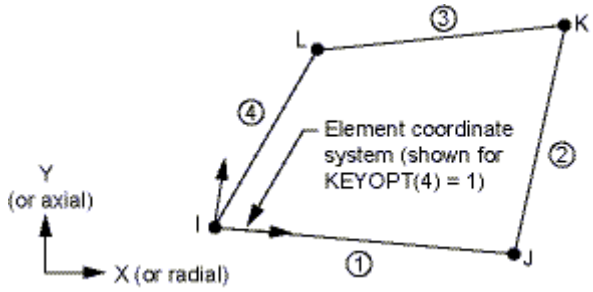

Figure 3.30 Schematic of the 2-D rectangular PLANE12 element

A series of temperatures (200 ^{o}C, 300 ^{o}C, 400 ^{o}C, and 600 ^{o}C) are assigned to T_h in this validation. Figure 3.31 shows the temperature distributions for T_h=600 ^{o}C, with 3.51a from ANSYS and 3.51b from the thermal module in this research. Both approaches

generate identical distributions. A positive temperature gradient is found from the upper surface to the lower surface of the armature leg. Such a temperature gradient will generate a downward deflection on the armature leg.

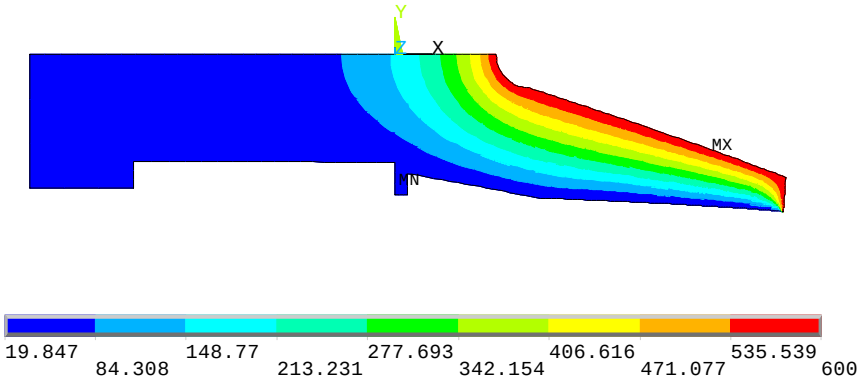

(a)

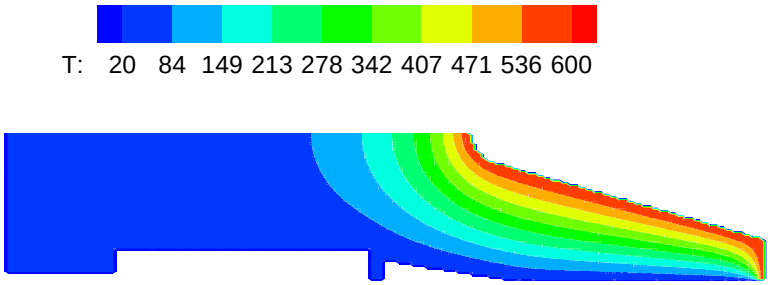

(b)

Figure 3.31 Comparison of the temperature distribution obtained from (a) ANSYS and (b) METHD model

Figure 3.32 compares the vertical displacement of the armature leg lower surface from both methods. Again, since the armature leg is not an ideal cantilever beam, an equivalent moment of inertia is found for the armature leg in the thermal analysis by comparing the deflection at the armature leg tip as a function of temperature T_h with

ANSYS results. The thermal beam bending model deployed in this research shows good agreement with ANSYS simulations. As listed in Table 3.6, the difference in the armature leg tip deflection from both methods is less than 3% for all four cases.

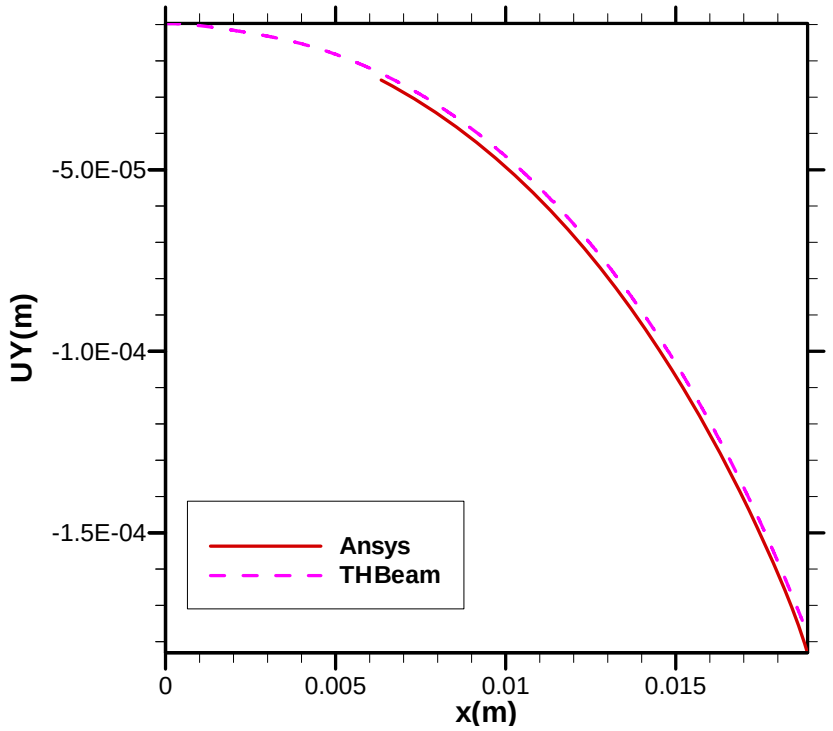

(a)

Figure 3.32 Thermal deformation results with different boundary temperature (*Th*): (a) 200 ^{o}C, (b) 300 ^{o}C, (c) 400 ^{o}C and (d) 600 ^{o}C

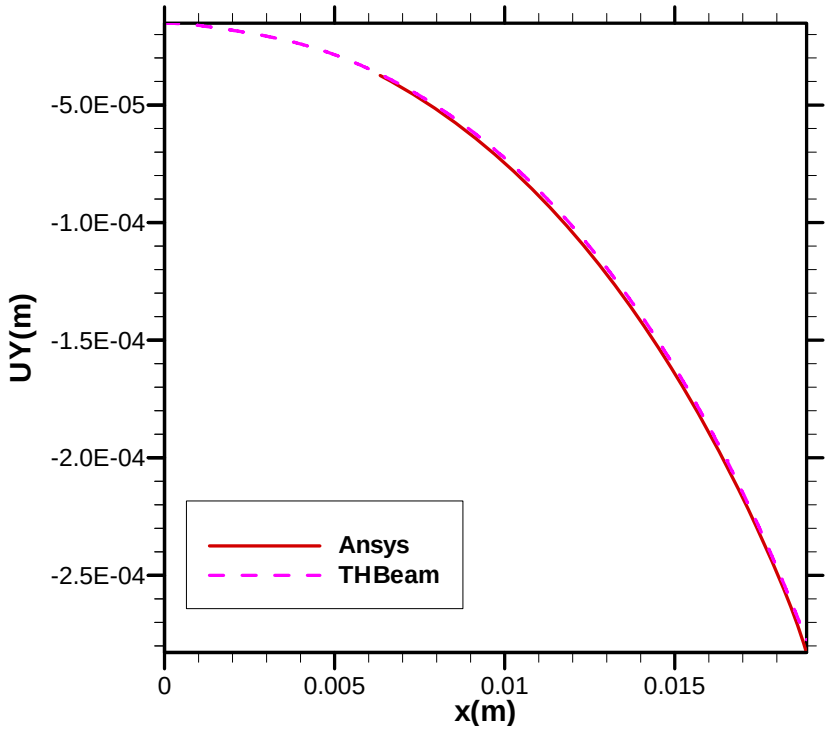

(b)

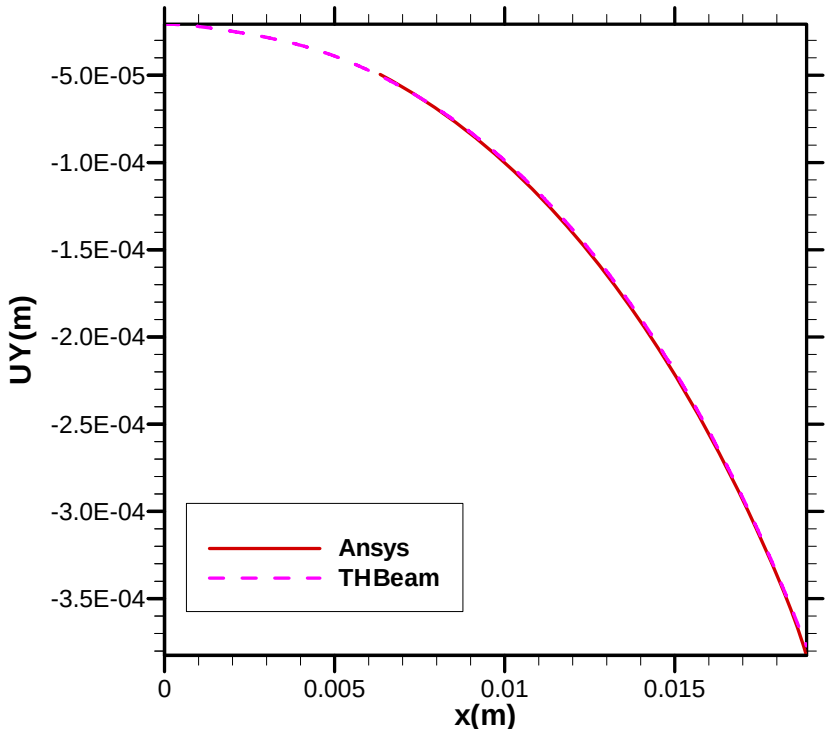

(c)

Figure 3.32 continued

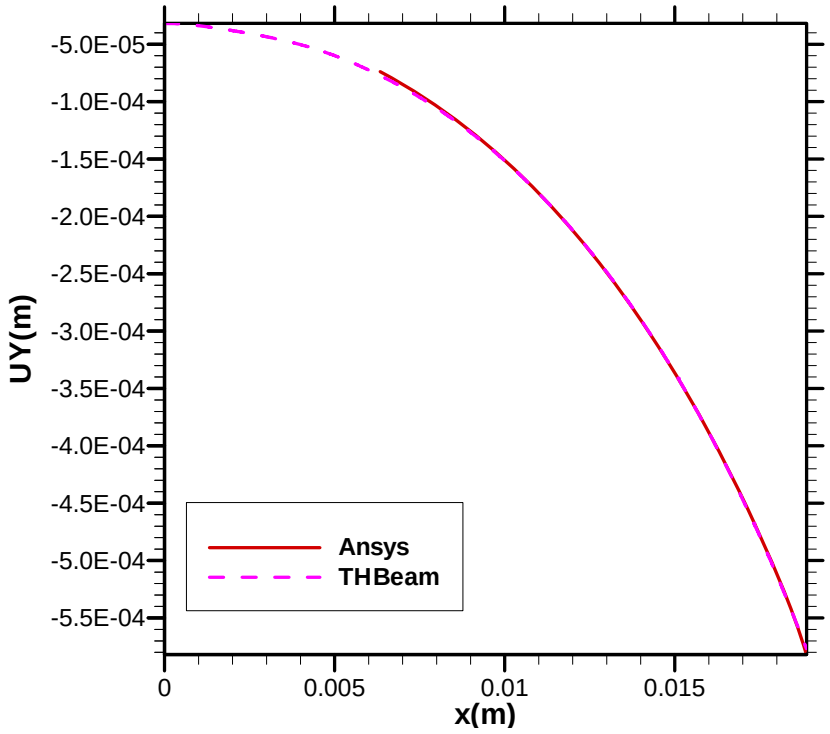

(d)

Figure 3.32 continued

Table 3.6 Comparison of the Predicted Thermal Deflection at Armature Leg Tip

Temperature (N)	**Deflection (m)**		
	ANSYS	Beam Model	Difference
200	-1.82E-4	-1.77E-4	2.7%
300	-2.83E-4	-2.78E-4	1.8%
400	-3.82E-4	-3.77E-4	1.3%
600	-5.81E-4	-5.76E-4	0.9%

3.3.3 Coupled Analysis and Launch History Prediction

The METHD model adds a thermal module to the previous coupled analysis. As shown in Figure 3.33, the electromagnetic module provides joule heating results to the thermal module, while the fluid mechanics module generates viscous heating and the contact module calculates frictional heating. The thermal module then computes the temperature field in the armature and transfers it to the deformation module to calculate thermal deformation.

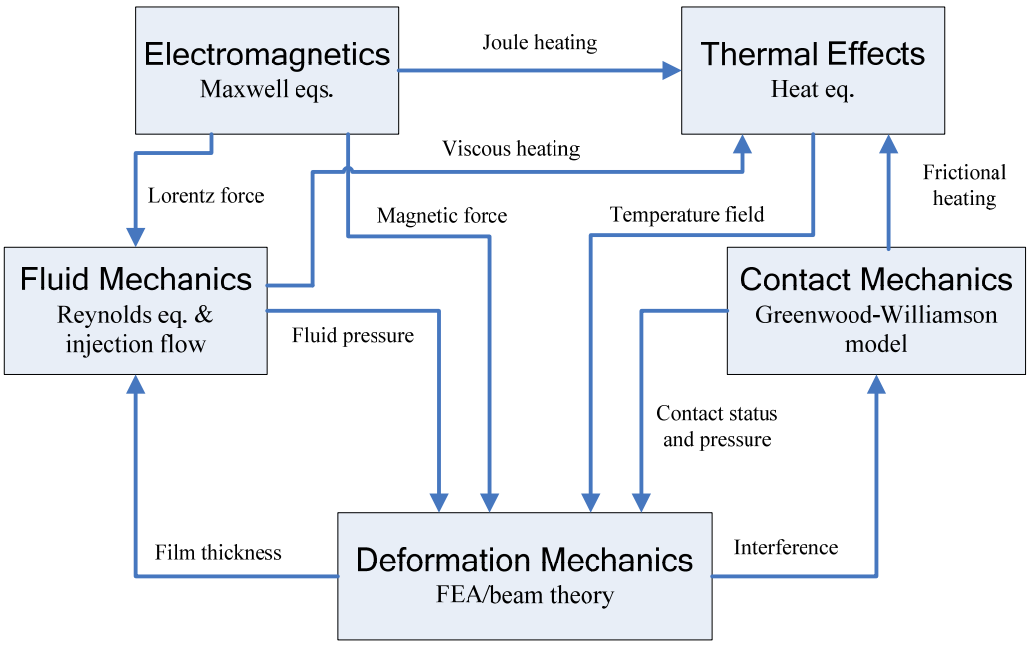

Figure 3.33 Coupled analysis of the METHD model

The corresponding program flowchart for launch history prediction is given in Figure 3.34. Note that the temperature field calculation is not included in the coupled

iteration. The temperature field is calculated at the end of each temporal step, and the corresponding thermal deformation is calculated at the beginning of each temporal step using the temperature information of the last step. Numerical simulations have shown that with small time intervals, such treatment greatly reduces the computational time while retaining the same accuracy as programs that iterate the temperature. Results obtained in this coupled manner provide a more complete and realistic prediction of the interface behavior and launch history in EML systems than do the results obtained using the previous two models.

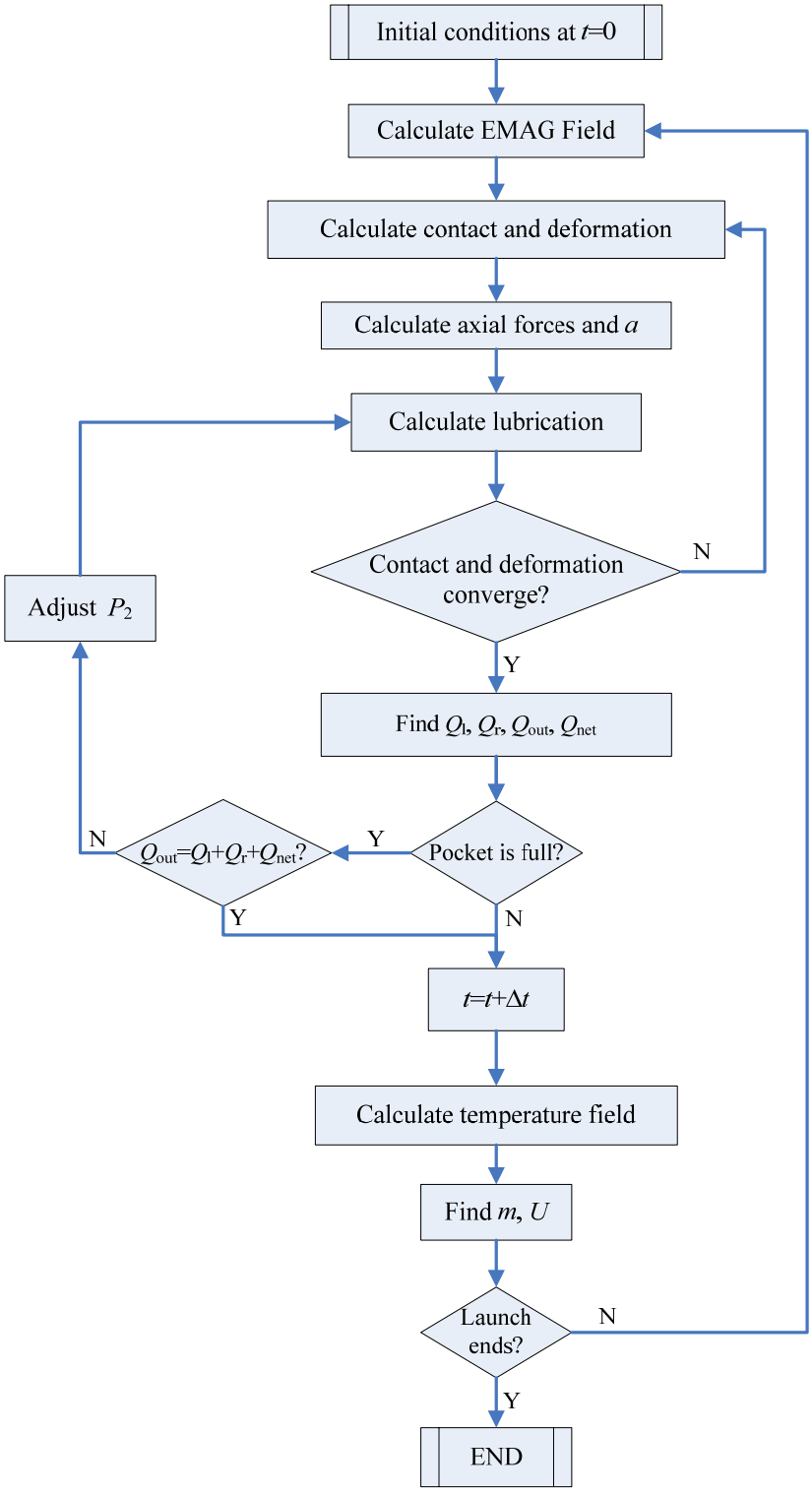

Figure 3.34 Flowchart of launch history prediction with the METHD model

CHAPTER 4

RESULTS AND DISCUSSION

In the previous chapter, a complete analytical model (the METHD model) is constructed to simulate the coupled effects of fluid mechanics, electromagnetics, temperature field, contact, and deformation mechanics. The goal of this model is to reveal the injection and lubrication mechanism at the interface, which cannot be discovered in experiments. Understanding the injection and lubrication process helps us to optimize design parameters, such as initial reservoir load, lubrication length, pocket capacity, and pocket geometry, and operation parameters, such as electric current discharge pattern. Such optimization seeks to discover the most effective interface injection and lubrication process with minimal initial reservoir load.

Parallel EML experiments have been conducted by Dr. Scott Bair and other researchers at Georgia Tech. In this chapter, a base case configuration with parameters from a real Georgia Tech launch is first simulated. Results are analyzed to understand the mechanism of a typical launch process. A troubleshooting analysis is conducted to find the possible reason for an unsuccessful experimental run. Different initial reservoir loads are tested and the optimal value is found. The current discharge patterns of two configurations are compared and the more beneficial one is identified. In order to provide guiding information for new armature pocket designs, different geometric parameters are studied and the effects of each parameter are evaluated. A recommended design procedure is then developed. To study the scaling effects, the size of the base case configuration is doubled and simulated. The optimal injection designs and corresponding

minimum initial reservoir loads for both the base case and the scaled one are found following the design guidelines developed in this study.

4.1 Base Case

The configuration of the Georgia Tech armature with an injection system in this base case is shown in Figure 4.1. A cylindrical reservoir is located in the head of the armature. Two injection conduits connect the reservoir to two pockets on each side of the sliding surface. The sliding surface is slightly tapered in order to produce a converging gap profile between the armature and the rail. The final spacing of the two rails is 13.9954 mm (0.551 inch). The net mass of the armature without any load is 8.9 grams. An amount of 1.7 g lubricant (gallium) is initially loaded in the reservoir sealed by a membrane. When the armature accelerates, the membrane is broken by the fluid pressure and lubricant is injected into the pockets and fills the armature-rail interface. An electric current discharged from a capacitor drives the armature to slide over a 1.0 meter long rail in 1.5 milliseconds in this case. Values of the material properties are listed in Table 4.1. To take advantage of the configuration symmetry, only half of the armature and one of the two rails are modeled in the simulation. The METHD model is implemented for computation. Results of the MHD and MEHD models for this base case are shown in Appendix B and C.

Table 4.1 Material Properties of the Base Case
(Ghassemi and Barsi, 2004; Spells, 1936; Bair, 2008; www.efunda.com, 2008)

Lubricant (gallium)	
$\mu^{(1)}$	$2.468\times10^{-4}\left(\frac{\rho}{1000}\right)^{\frac{1}{3}} e^{\frac{79.05\left(\frac{\rho}{1000}\right)}{T+273}}$ Pa-s
ρ	6.0×10^{3} kg/m^3
σ^*	5.75×10^{6} Mho/m
μ_a	1.2567×10^{-6} N/A^2
k_f	41 W/(m-K)
c_f	371 J/(Kg-^{o}C)
Armature (aluminum)	
σ	1×10^{-6} m
γ	1 (isotropic)
E	70 GPa
$\sigma^{*(2)}$	$\frac{3.21\times10^{7}}{1+0.0039(T-27)}$ Mho/m
μ_a	1.2567×10^{-6} N/A^2
k_a	167 W/(m-K)
$c_a^{(2)}$	0.486(T+273)+766 J/(Kg-^{o}C)
Rail (copper)	
σ	1 x 10^{-6} m
γ	1 (isotropic)
E	120 GPa
$\sigma^{*(2)}$	$\frac{4.41\times10^{7}}{1+0.0039(T-27)}$ Mho/m
μ_r	1.2567×10^{-6} N/A^2
k_r	388 W/(m-K)
$c_r^{(2)}$	0.0987(T+273)+355 J/(Kg-^{o}C)

(1): Units for ρ are kg/m^3.
(2): Unit for T is ^{o}C.

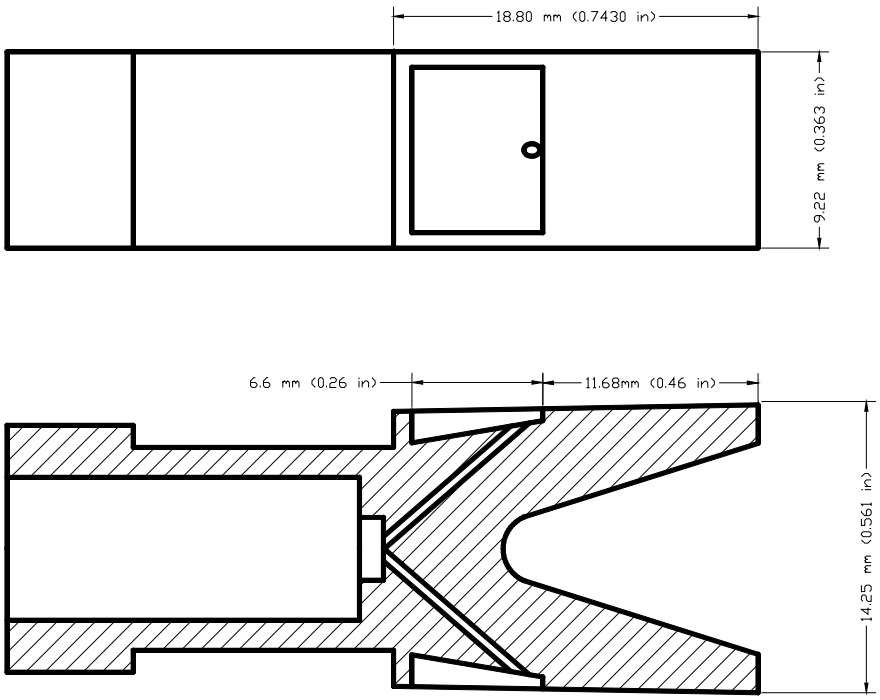

Figure 4.1 Dimensions of the armature with the reservoir-pocket injection configuration

In the EML system at Georgia Tech, electrical energy is first charged to a capacitor connected to the device. When a launch begins, the capacitor discharges and serves as the power supply for the system. Figure 4.2 shows the electric current history of the base case. The current increases rapidly as the launch starts and reaches its maximum value of 250 KA at 0.5 ms. It then decreases gradually till the end of the launch (I=50 KA at t= 1.5 ms). After the armature has left the barrel, the capacitor quickly discharges through arcing in the air.

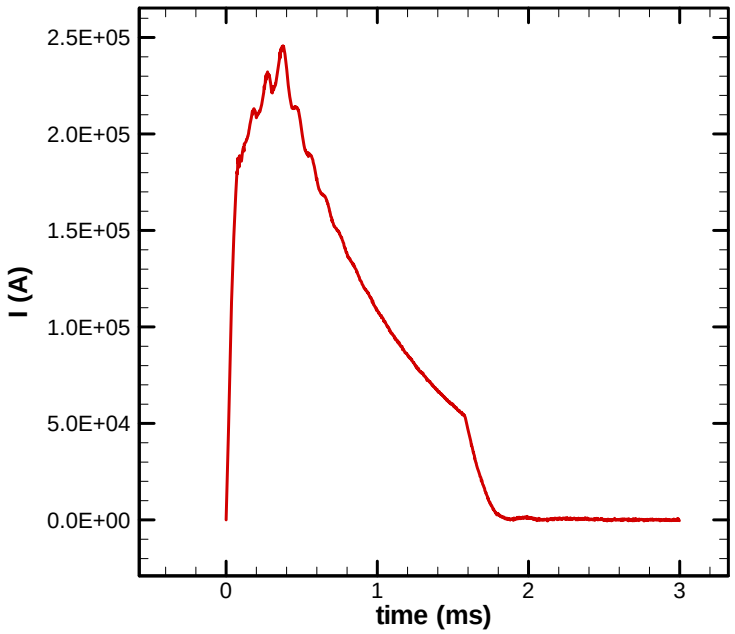

Figure 4.2 Electric current history of the base case

Figure 4.3 illustrates the magnetic flux density distribution at different times in the symmetric half of the armature-rail configuration. Evolution of the magnetic field during the launch is captured by the transient EMAG module: in the armature, the magnetic field concentrates at the trailing surfaces initially (t= 0.1 ms) and diffuses into the armature as time goes on; in contrast, the magnetic penetration depth in the rail adjacent to the armature decreases as the armature velocity increases with time. The maximum magnetic flux density occurs at 0.5 ms when the electric current achieves its maximum value (Figure 4.3b).

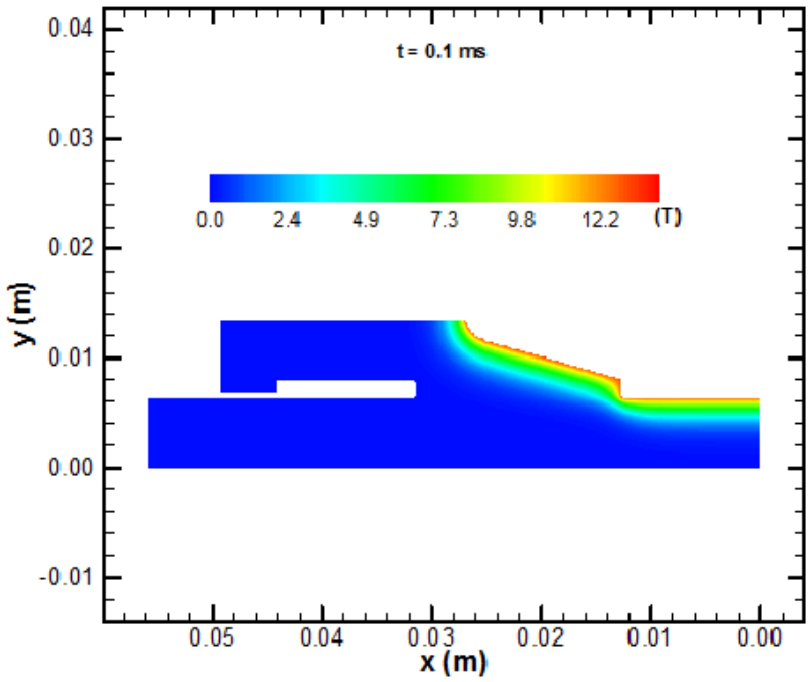

(a)

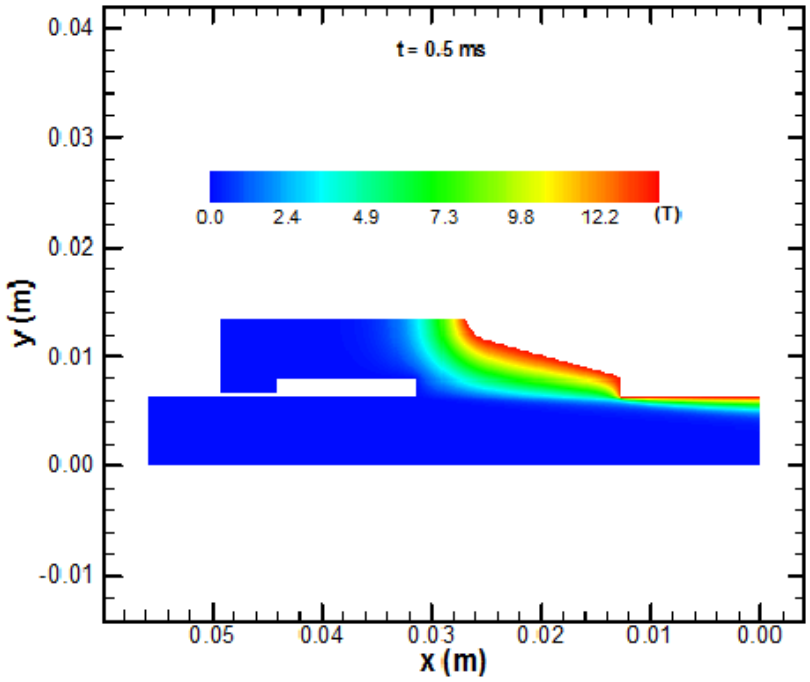

(b)

Figure 4.3 Magnetic flux density distribution of the base case at different times

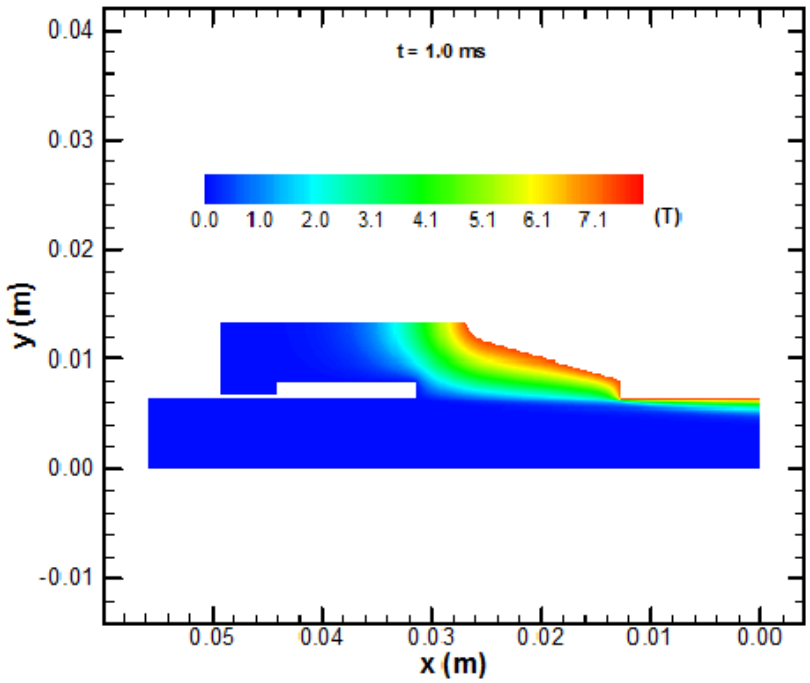

(c)

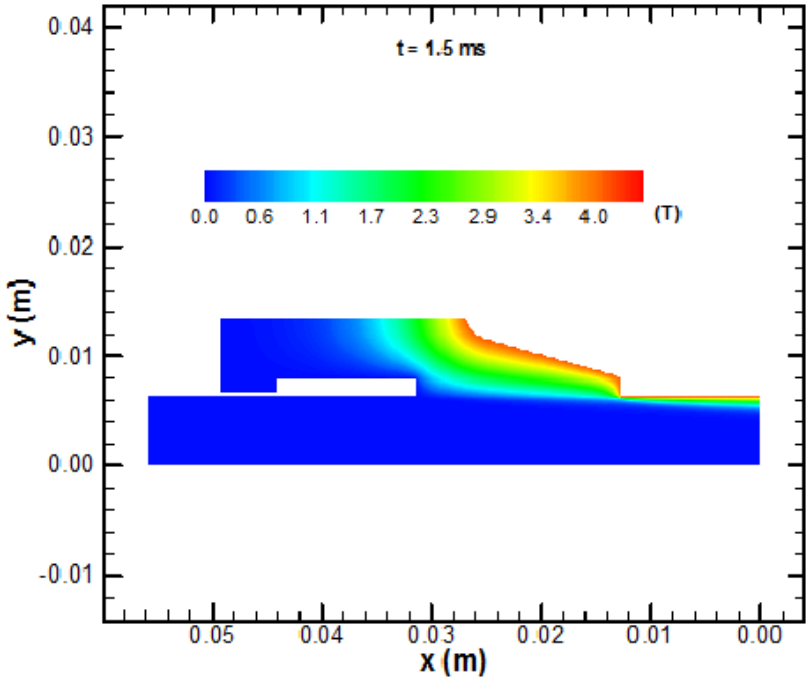

(d)

Figure 4.3 continued

The corresponding electric current distributions for these times are depicted in Figure 4.4 (arrows for direction, contour colors and arrow length for magnitude). As shown in the figure, the electric current flows in from the rail and enters the armature across the interface. It concentrates at the upper surface of the rail at the rear of the armature-rail interface, namely the velocity skin effect. The current also condenses close to the inner surface in the armature. For example, at 0.5 ms, the maximum current density at the trailing edge of the interface is about 10 GA/m^2; the average density in the armature leg is about 3 GA/m^2. However, in contrast to the magnetic field distribution, high current density regions are not always on armature surfaces. They sometimes appear at a certain distance away from the surface to compose the lowest resistance path for current flow.

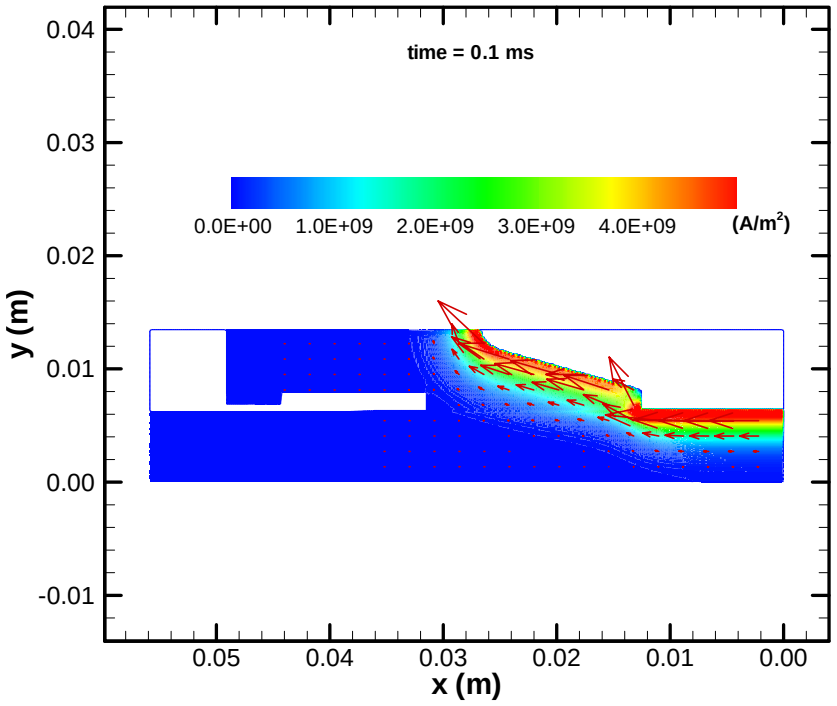

(a)

Figure 4.4 Electric current distribution of the base case at different times

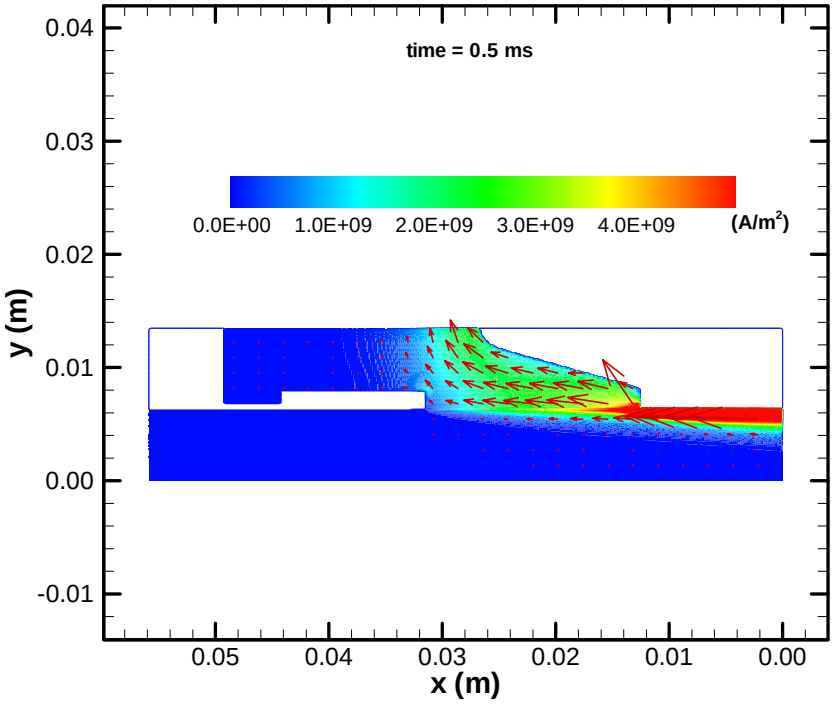

(b)

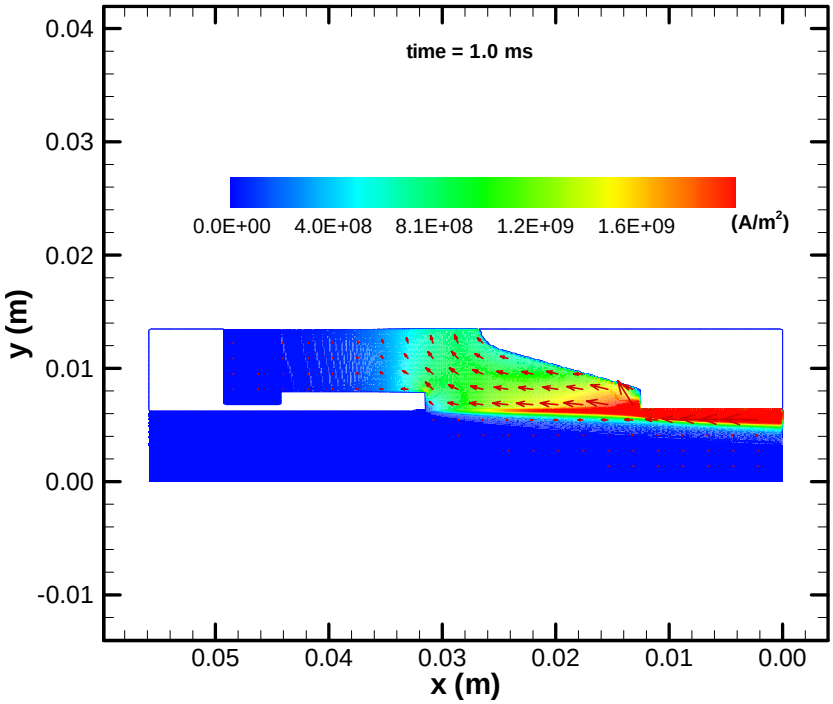

(c)

Figure 4.4 continued

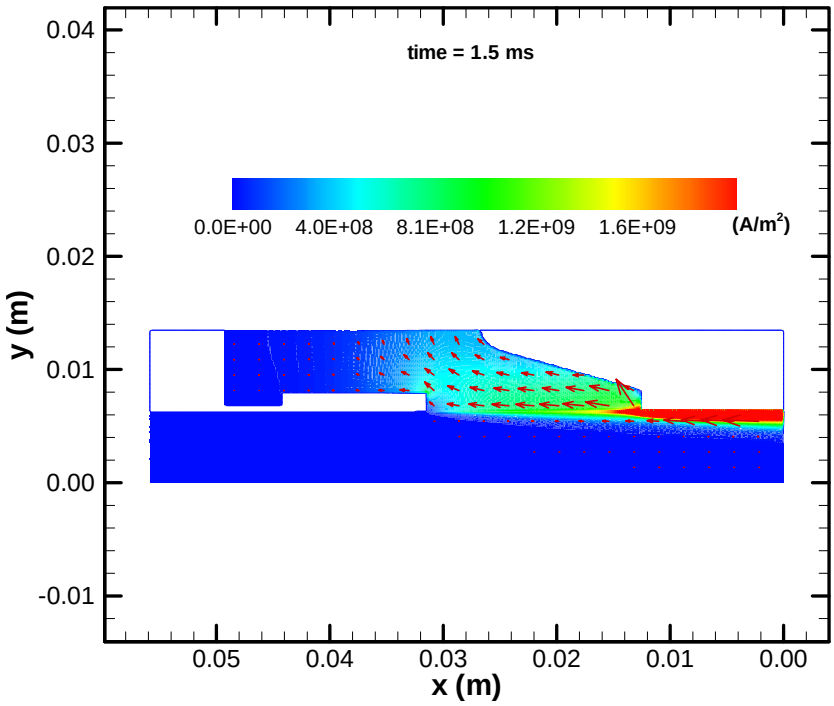

(d)

Figure 4.4 continued

With the distributions of the magnetic field and the electrical field, the magnetic force acting on both the armature and the rail is calculated and plotted in Figure 4.5. Since it is proportional to magnetic flux density and electric current strength, this magnetic force also distributes mainly in the armature leg, with one component acting forwards to propel the armature and the other one acting downwards to squeeze the armature leg against the rail. The effects of the magnetic force in the rail are neglected in this study because the rail is fixed and well supported.

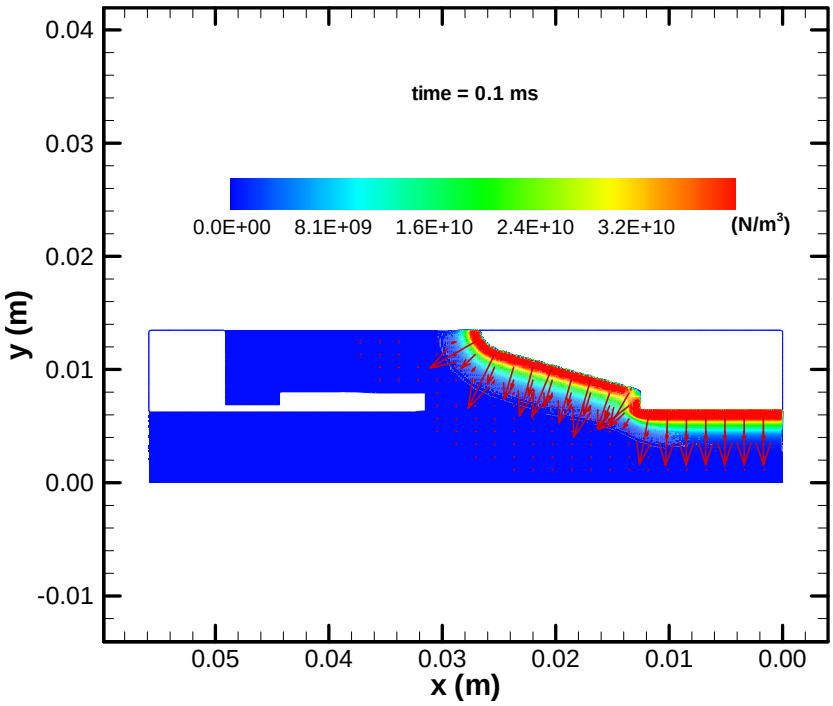

(a)

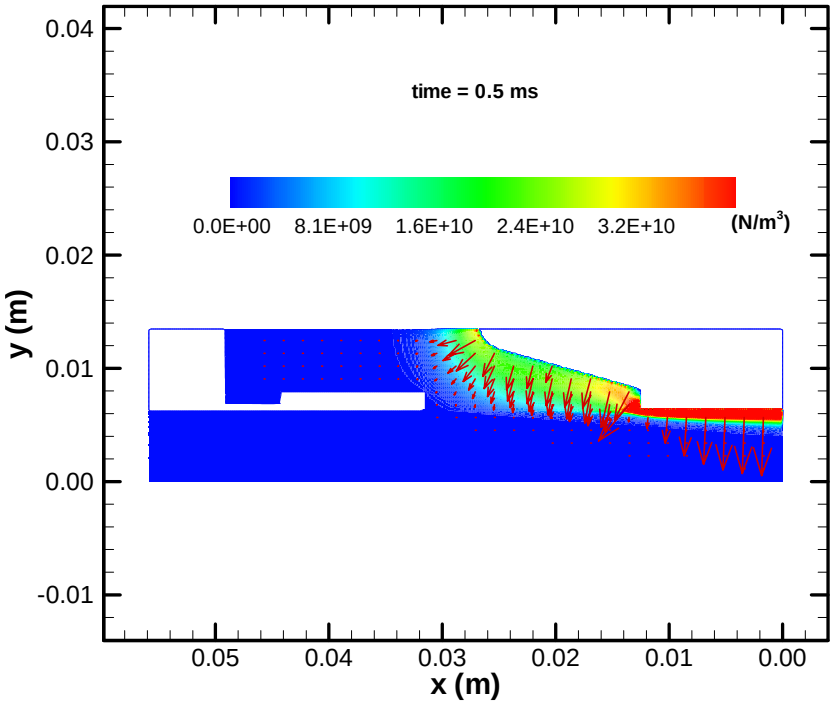

(b)

Figure 4.5 Magnetic body force distribution of the base case at different times

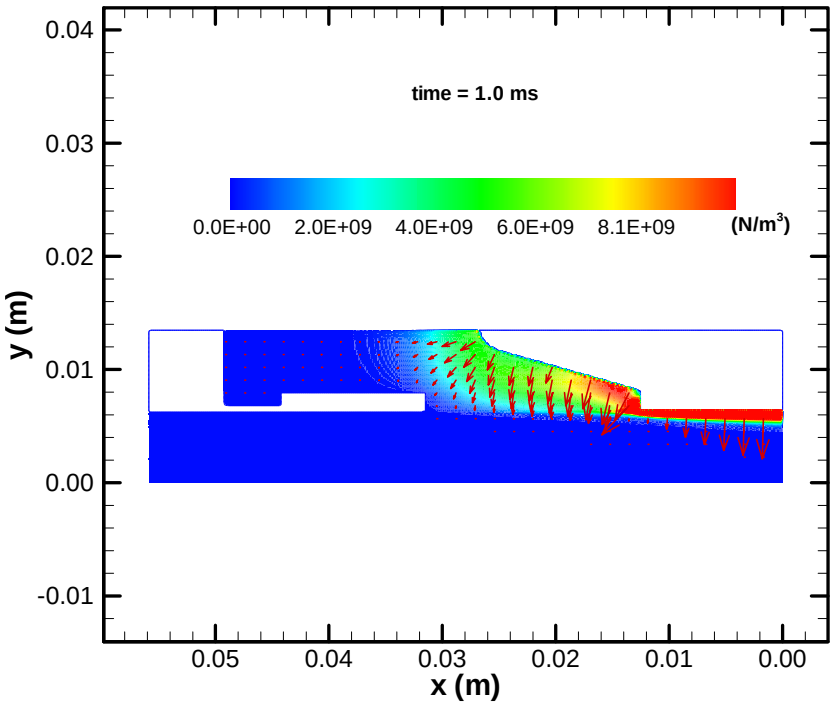

(c)

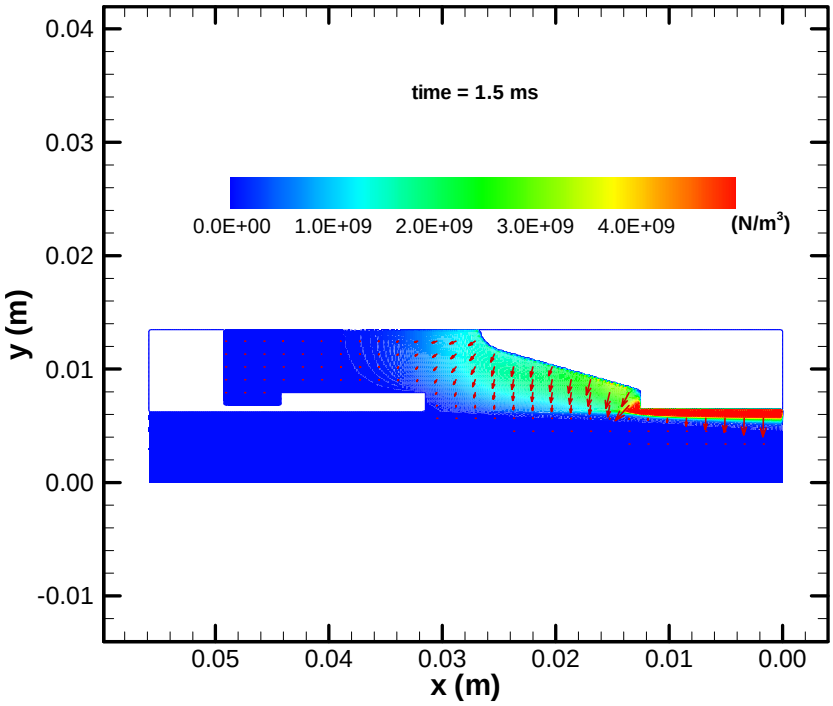

(d)

Figure 4.5 continued

Heat sources are introduced to the system by joule heating from the electric current, frictional heating from the sliding of contact surfaces, and viscous heating from liquid flow. The resultant temperature history is displayed in Figure 4.6. As the armature slides on the rails, heat at the interface is removed by the rail and the lubricant that flows out. Therefore, the temperature rise inside the armature is mainly produced by joule heating. High temperature zones are found at corners where the electric current is intense. Although the duration of a launch is rather short and some researchers neglect the heat diffusion in their research, especially in the melt-wave analysis (James and James, 1995; Woods, 1997), heat diffusion is observed in this study and a thermal model to consider such conduction is believed to be more realistic.

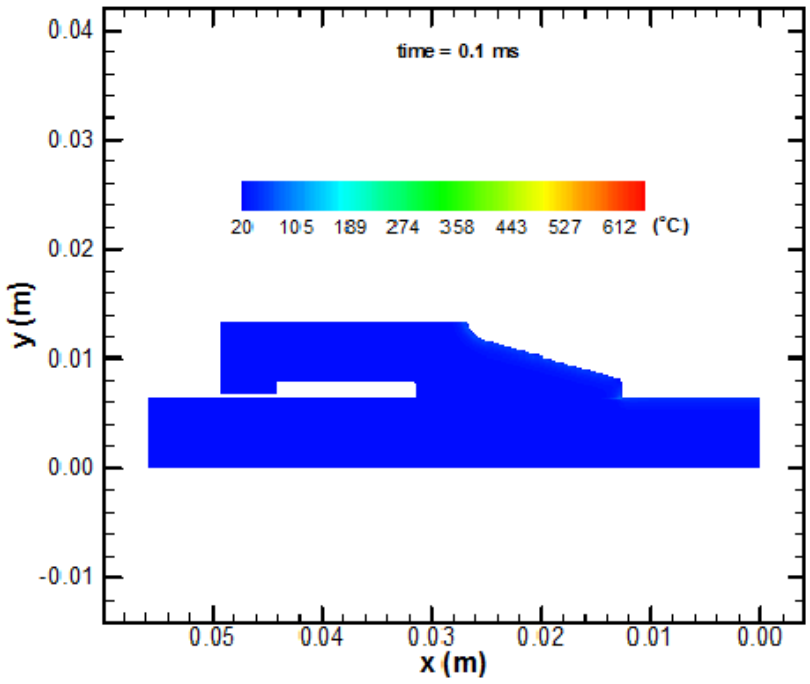

(a)

Figure 4.6 Temperature distribution of the base case at different times

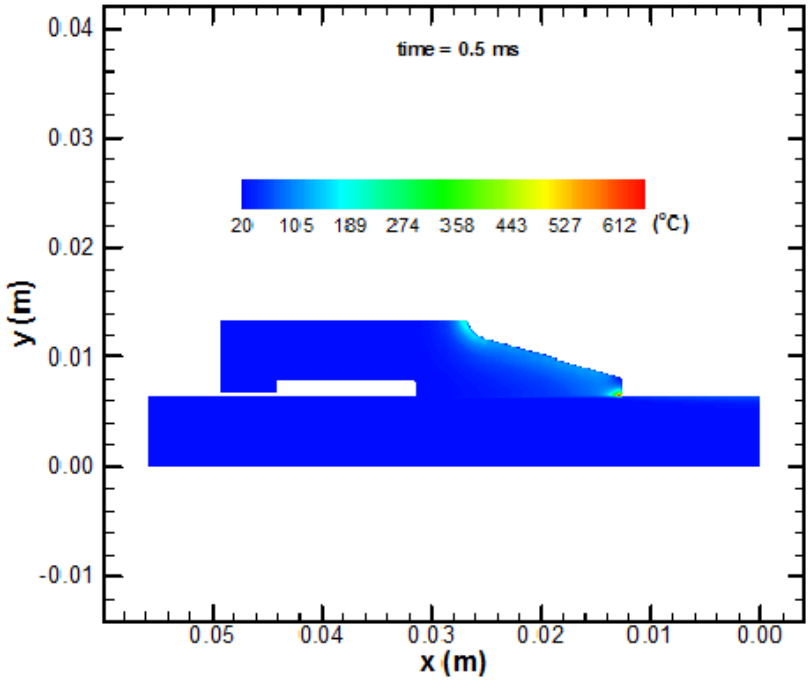

(b)

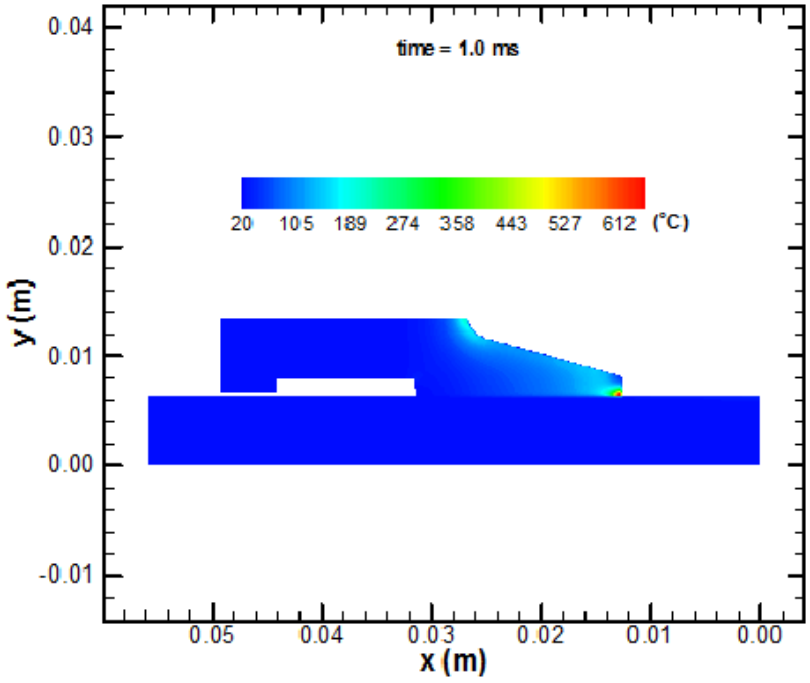

(c)

Figure 4.6 continued

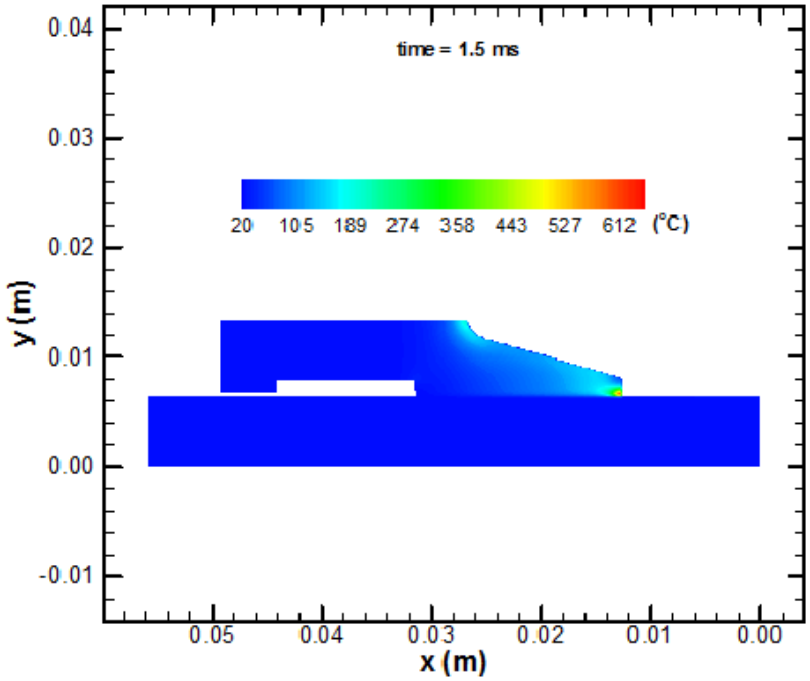

(d)

Figure 4.6 continued

The magnetic force shown in Figure 4.5 generates an *x*-direction component that propels the armature (F_{emag}). On the other hand, *x*-direction resistive forces are produced by friction due to contact sliding (F_f) and by the viscous effects in the fluid (F_v). These three forces and their summation (the total force F_{total}) are plotted in Figure 4.7. The magnetic driving force is proportional to the electric current that flows through the system. The maximum value of F_{emag} is 15K N at 0.5 ms. The peak of the friction force is observed at the threshold of the launch, being the result of intensive initial contact. This friction force then declines rapidly as contact is gradually eliminated when the sliding speed goes up. The viscous force grows from zero with the increasing sliding speed. It remains relatively stable after 0.5 ms because the increasing film thickness compensates for the growing sliding speed. Both friction and viscous forces are several orders less

than the magnetic force. The total force is almost identical to the magnetic force and they overlap in the figure.

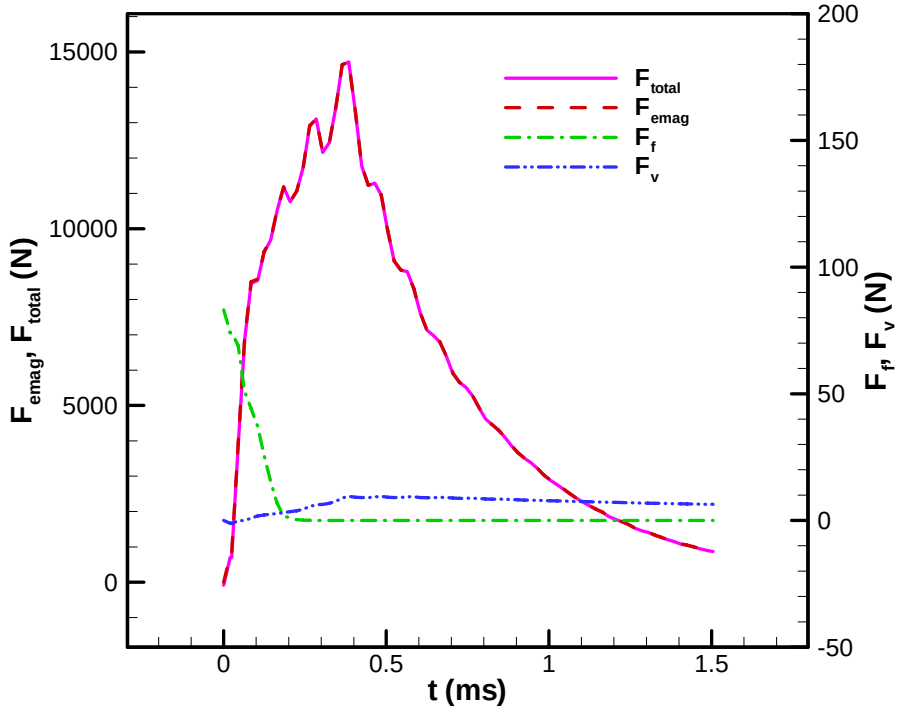

Figure 4.7 *x*-direction armature force history of the base case

The armature acceleration history, resulting from the forces shown in Figure 4.7, is depicted in Figure 4.8. The acceleration also shows a positive relationship with the electric current: the armature achieves its maximum acceleration of 1.5E6 m/s^2 by the maximum current at 0.5 ms.

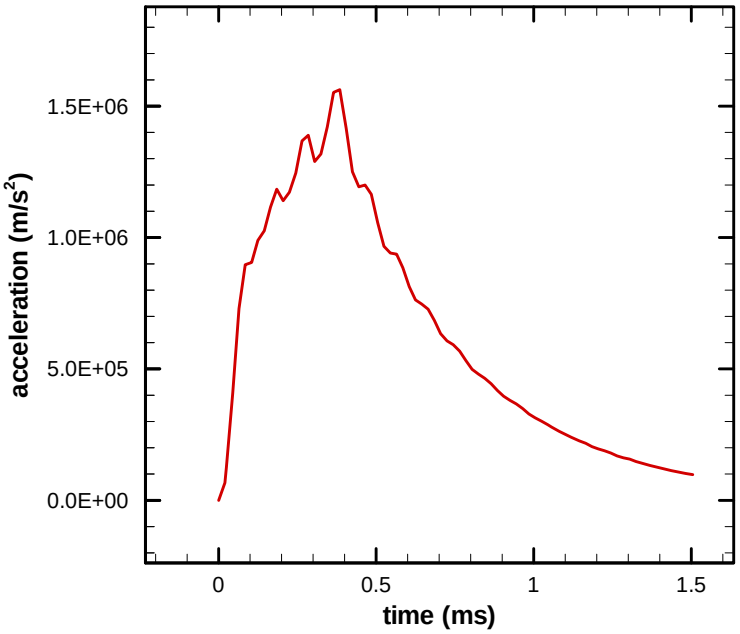

Figure 4.8 Armature acceleration history of the base case

Figure 4.9 shows the corresponding velocity history of the armature. The velocity increases rapidly at the threshold of the launch as a result of the strong acceleration. As acceleration drops after 0.5 ms, armature velocity increases gradually slow until a final velocity of around 1000 m/s is reached.

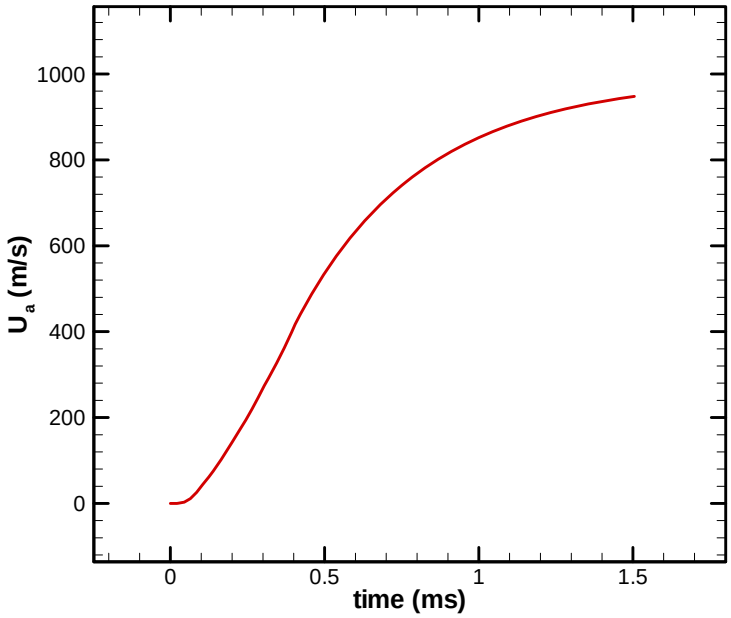

Figure 4.9 Armature velocity history of the base case

In experiments, some sensors called the B-DOTs are placed on the rail at given locations. Those B-DOTs detect the armature when it passes by them. In this way, some scattered data of location vs. time are generated. Figure 4.10 shows the predicted armature location compared to those experimental measurements. The prediction not only agrees with the measurements but also provides complete and continuous armature location information.

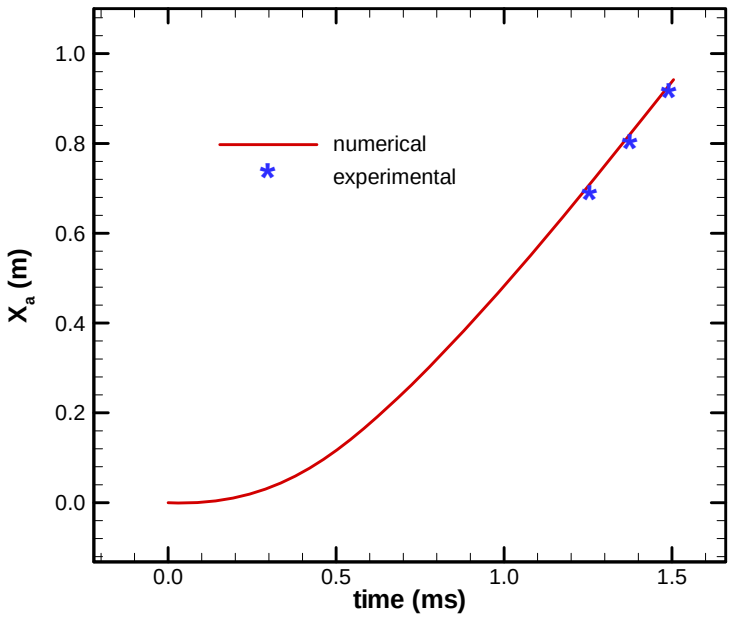

Figure 4.10 Comparison of predicted armature location history with experimental measurements

Figure 4.11 contains the histories of the mass flow amounts: Q_{out}, Q_l, Q_r, and Q_{net}. The history of Q_{out} shows that all the lubricant in the reservoir is driven out at the beginning of the launch. The pocket is immediately filled (Q_{net}) and excess fluid flows out from the leading edge at once (Q_l). Then the pocket acts as a spare reservoir and provides lubricant flowing downstream through the interface to the trailing edge (Q_r). The amount of lubricant left in the pocket (Q_{net}) is an indication of the pocket lubricant life. Such a lubrication process demonstrates the importance of the pocket, which is indeed the only source to feed the interface during the launch. Therefore, it must be carefully designed in order to ensure a successful launch. Another fact that is noticed from the results is that around 0.6g of lubricant leaks from the front edge of the interface (Q_l). This portion of the lubricant makes no contribution to the lubrication process and thus it should be minimized in order to reduce the reservoir load. Investigations will be

conducted later in this study based on these observations to improve the pocket design as well as to reduce the reservoir load.

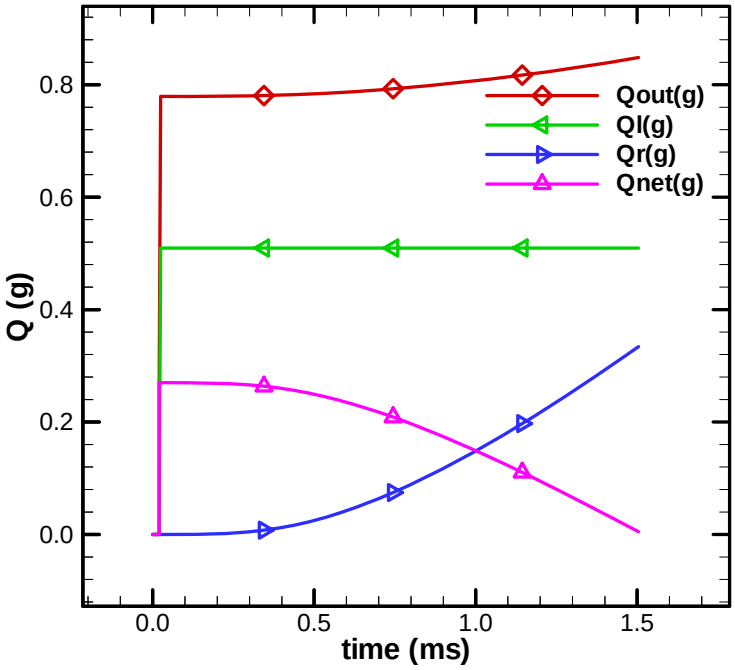

Figure 4.11 Mass flow amount history of the base case

The minimum film thickness along the interface provides an estimate of contact status and overall film thickness. Figure 4.12 presents the evolution of non-dimensional minimum film thickness. With the base case configuration, the interface starts with a close contact (H_m=1.3, calculated from the contact module); as the armature accelerates and the fluid pressure goes up, the interface gap is expanded and contact is expected to disappear since H_m gradually reaches 6 at 0.5 ms and 9 at the end of the launch. Reducing contact at the interface by providing lubricant into the gap as in this study will help to reduce friction and wear of the contacting surfaces while still ensuring electrical continuity across the interface.

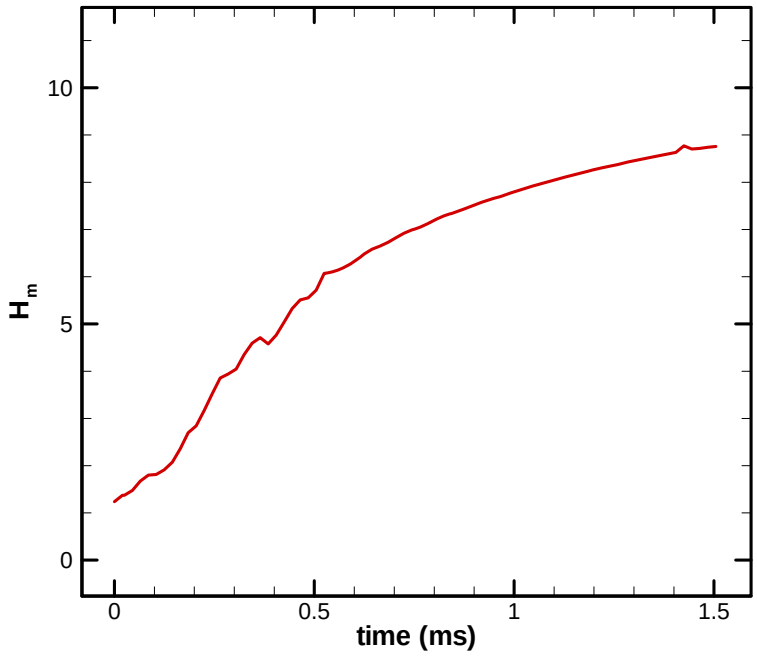

Figure 4.12 Minimum nondimensional film thickness history of the base case

Figure 4.13 illustrates the pressures in the lubricant at different times, where the dashed line is the real fluid pressure (P_{fl}), the dash-dotted line is the magnetic pressure (P_m) and the solid line is the total pressure (P) which is the summation of the former two. At the beginning of the launch (t=0.1 ms, Figure 4.13a), the fluid pressure at the pocket side (x=0) is very high (35 MPa); it is the hydrostatic pressure produced by the large acceleration and high pocket charge. At the interface's rear exit, the fluid pressure is assumed to be atmospheric. The magnetic pressure is negligible at the front half of the film but significant (65 MPa) at the trailing edge (x=0.012 m). Similar patterns are observed at 0.5 ms. However, as the armature moves on (t=1.0 ms, Figure 4.13b), the fluid pressure at the pocket side decreases to 8 MPa due to decreases in armature acceleration and pocket charged length. The magnetic pressure is also reduced to 20 MPa.

When the armature approaches the muzzle at t=1.5 ms (Figure 4.13d), the pocket is almost drained out and the fluid pressure at the pocket side also becomes atmospheric pressure. The magnetic pressure almost vanishes because of a very weak electric current. In the entire launch history, the maximum total pressure occurs at 0.5 ms with a value of 130 MPa.

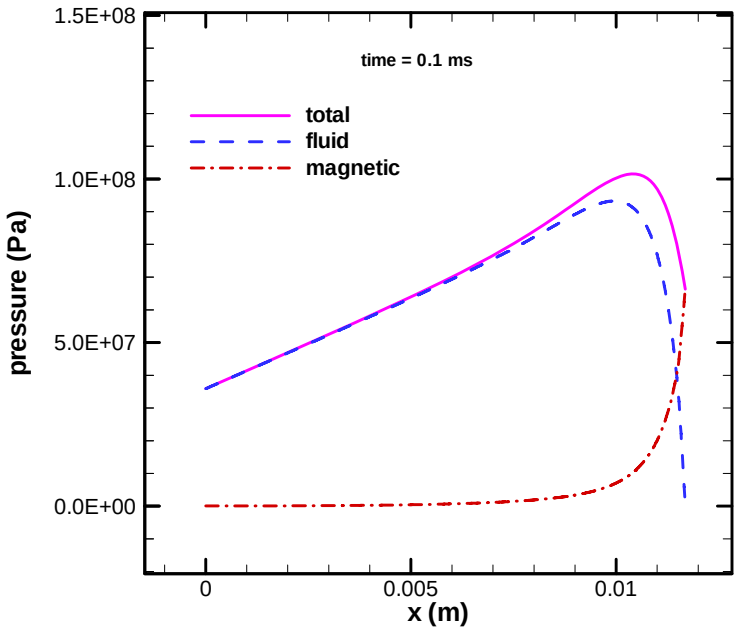

(a)

Figure 4.13 Pressures in the fluid of the base case at different times

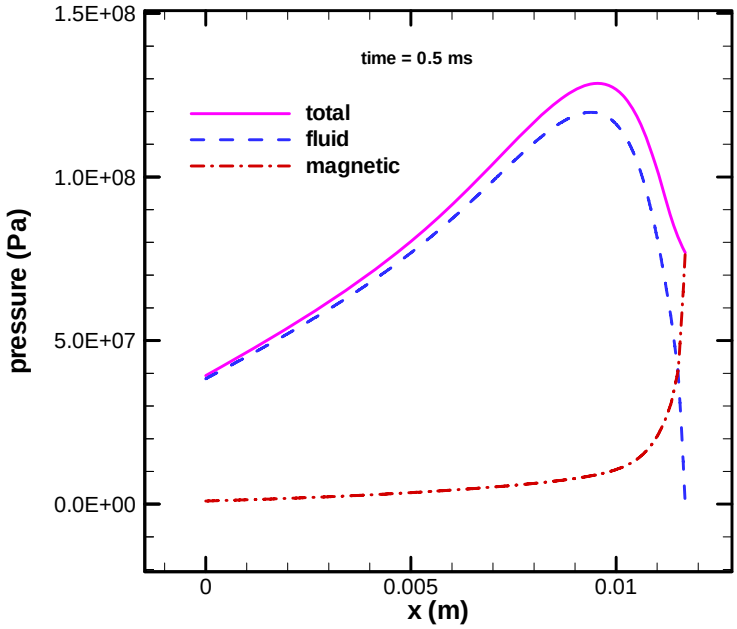

(b)

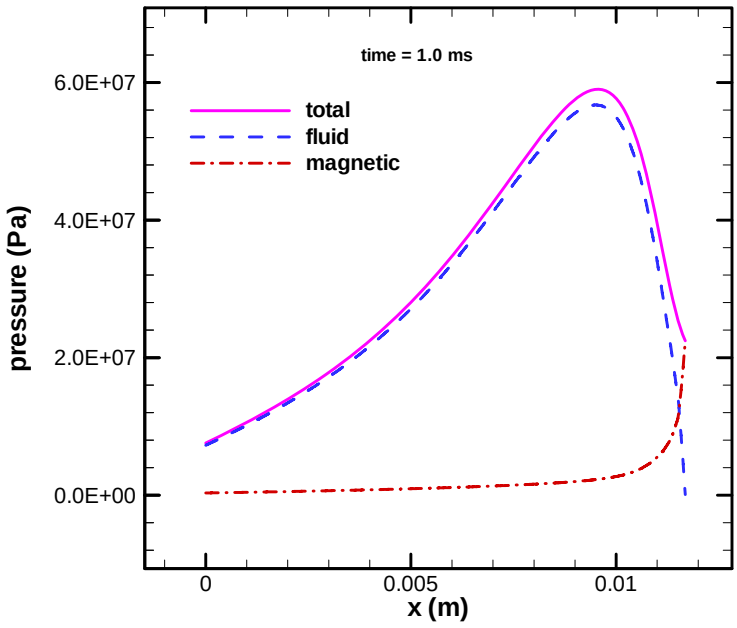

(c)

Figure 4.13 continued

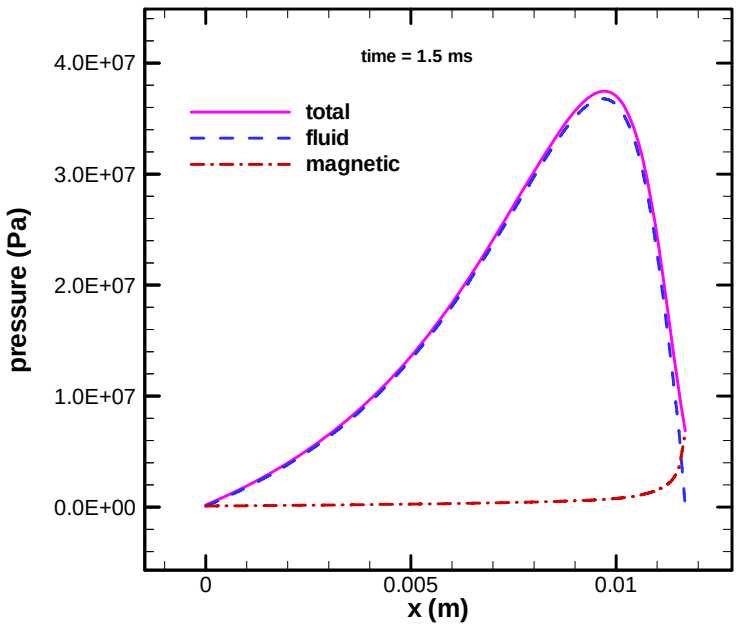

(d)

Figure 4.13 continued

Figure 4.14 contains the distributed forces along the armature leg vs. the distance to the bounded end in the beam deformation module. The dashed line represents the vertical magnetic force on the armature, the dash-dotted line the contact force, the dash-dot-dotted line the fluid force along the entire gap including the pocket, and the solid line is the total of the above. A positive force lifts the armature leg and expands the interface gap, while a negative one squeezes the armature and compresses the interface. However, it is the net moment that mainly determines the deformation. By comparing Figures 4.14a – 4.14d, it is found that the negative magnetic force decreases rapidly from its maximum value at 0.5 ms with the decrease of electric current. The positive fluid force also decreases, but in a much slower pattern compared to the magnetic one. Contact is only observed at the beginning of the launch (0.1 ms) because the gap is quickly expanded as the armature accelerates on the rails. The profile of the total force is pretty interesting,

though. It is negative in the front half due to the large negative magnetic component, and it is positive in the back half as the positive fluid component dominates. The net moment produced by the distributed forces generates an armature leg deformation that expands the interface gap.

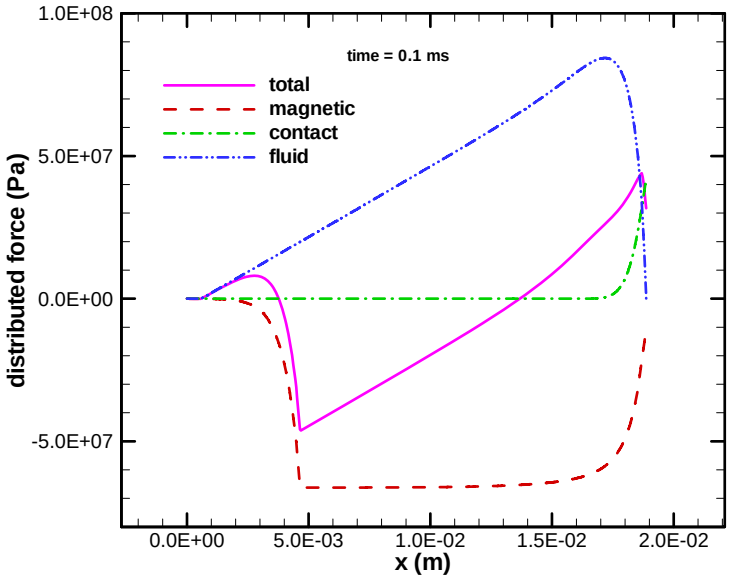

(a)

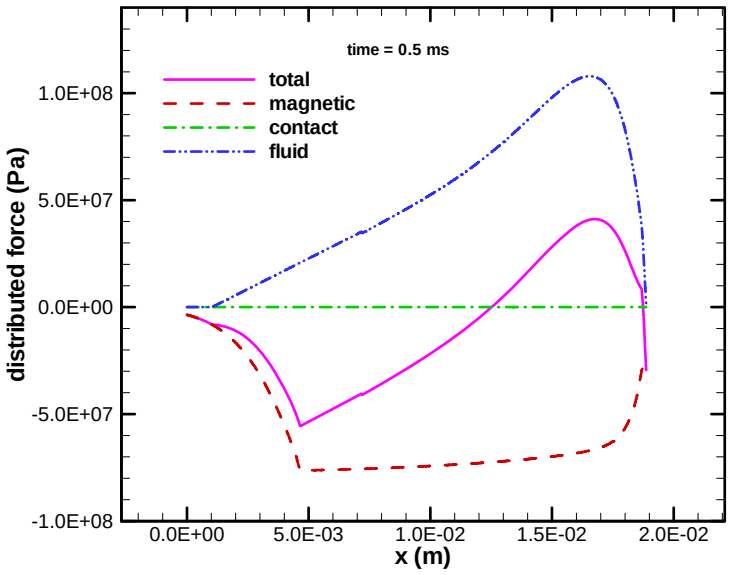

(b)

Figure 4.14 Distributed forces on the armature leg of the base case at different times

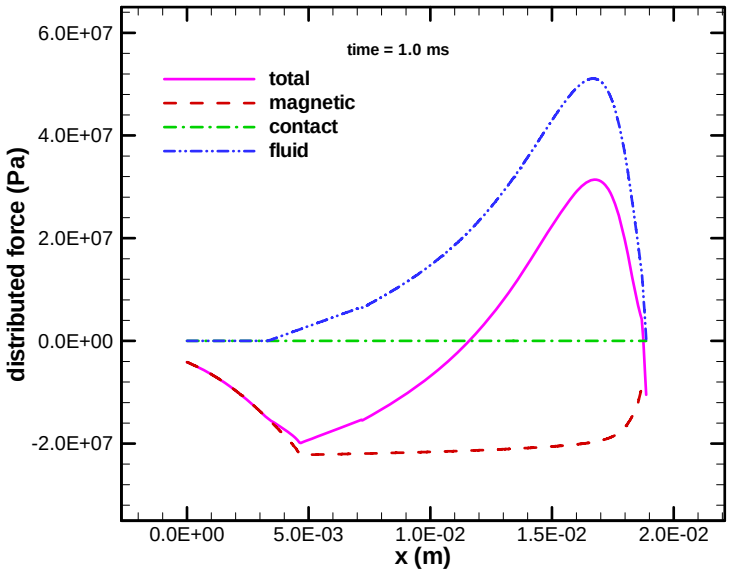

(c)

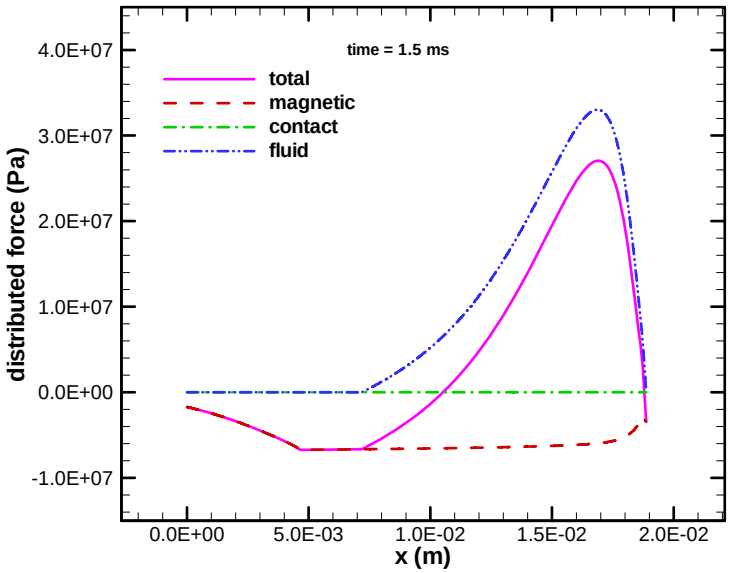

(d)

Figure 4.14 continued

The pressure profile shown above results in interface deformation and a corresponding film profile. The dimensionless film thickness at the interface is plotted in Figure 4.15. At the beginning (0.0 ms), no electromagnetic field is imposed on the system

and the armature is stationary on the rail. The film profile is determined by the static contact between the rail and the armature. The thinnest film profile occurs at 0.1 ms when the magnetic field is very intensive but the fluid pressure is relatively small due to small armature velocity. At 0.5 ms, although the magnetic field achieves its peak, the lifting effects produced by the increasing fluid pressure compensate for the magnetic squeezing effects. As a result, an increase of the film thickness is observed, especially at the trailing edge, where fluid pressure is dominant. At 1.0 ms and 1.5 ms, the magnetic force continues to decrease and the fluid pressure continues to increase. Therefore, a continuously growing film thickness is observed, especially at the trailing edge.

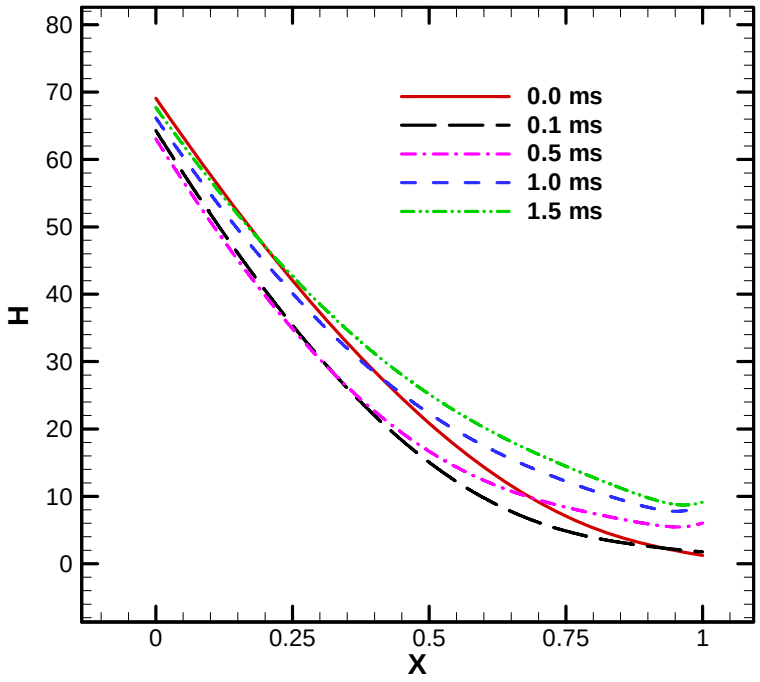

Figure 4.15 Nondimensional interface gap profiles of the base case at different times

The flow patterns in the interface gap are plotted in Figure 4.16. A large recirculation region exists in the front of the gap. A portion of the fluid that is dragged into the gap by the sliding rail flows back to the pocket. The presence of the pocket not only supplies the interface with its charge from the reservoir injection, but also saves the fluid from this reverse flow to provide lubricant to the interface at a later time. Fluid flow at the exit of the interface gap is unidirectional. A short diverging gap segment is formed at the trailing edge due to the high fluid pressure there (1.0 ms and 1.5 ms).

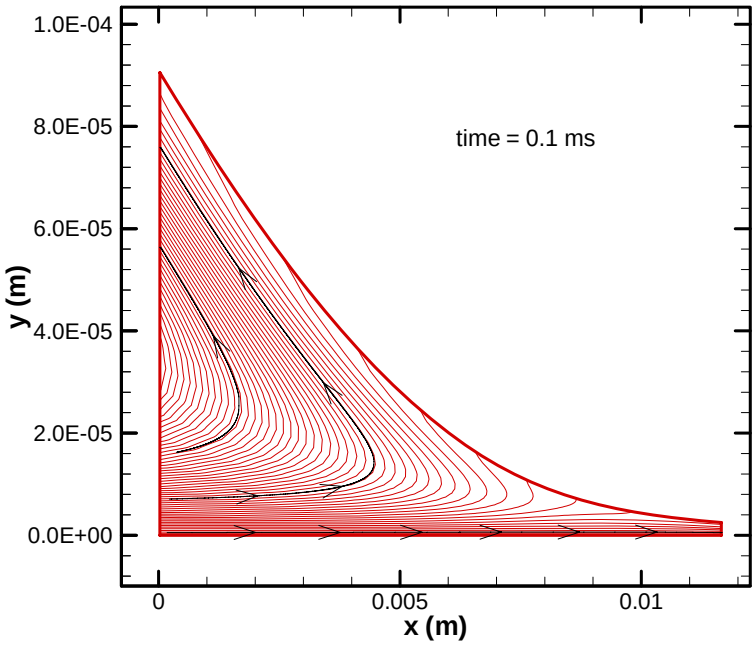

(a)

Figure 4.16 Fluid flow patterns of the base case at different times

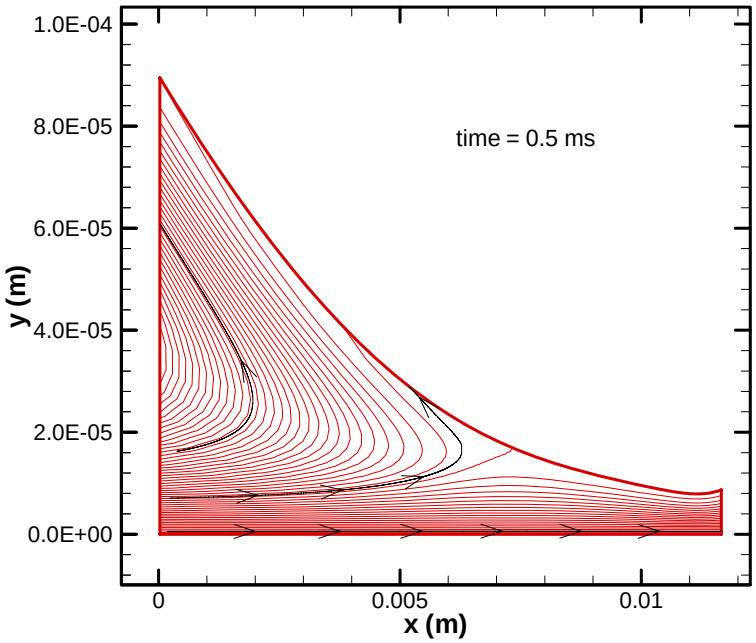

(b)

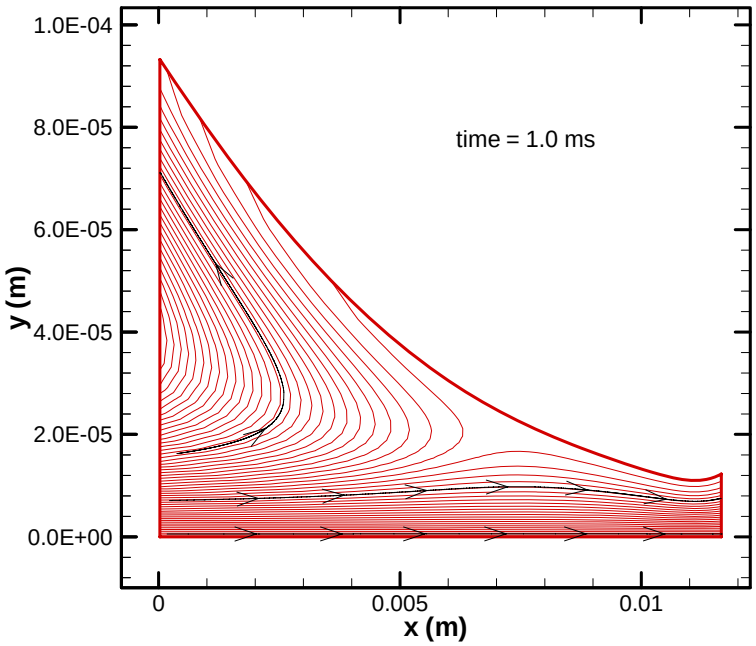

(c)

Figure 4.16 continued

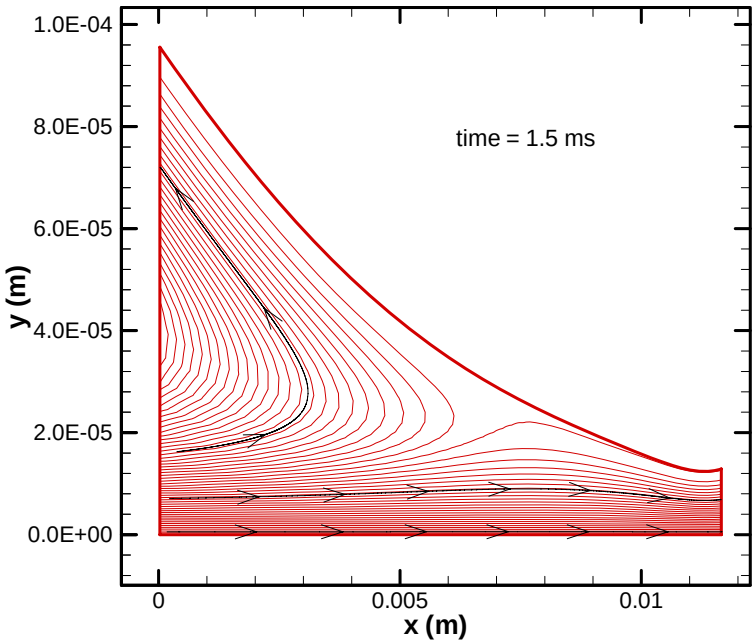

(d)

Figure 4.16 continued

4.2 Launch Failure Troubleshooting

An experimental launch with the base case configuration and parameters was performed by another investigator, and was successful. No transition occurred during the launch: the muzzle voltage remains at a low level with a jump at the end of the launch because the circuit becomes open after the armature has left the muzzle (Figure 4.17, shot 1). A successive shot was launched with the same configuration right after the base case projectile. This second launch failed; i.e. a muzzle voltage jump is observed in the middle of the launch, which indicates that a transition occurs at the interface (t=1.0 ms, shot 2 in Figure 4.17). Transition is known to be the result of an electrical conduction discontinuity caused by lack of lubricant at the interface. In these two launches, a mixture of 75% Ga

and 25% In was used as lubricant. Indium burned in the first launch and its debris left on the rails is considered to be the cause of the failure for the second launch. But the mechanism of the debris's effects was unknown. A numerical analysis with the METHD model was conducted to validate this hypothesis and discover the mechanism of the debris' influence. The material properties of pure gallium are used in the simulation.

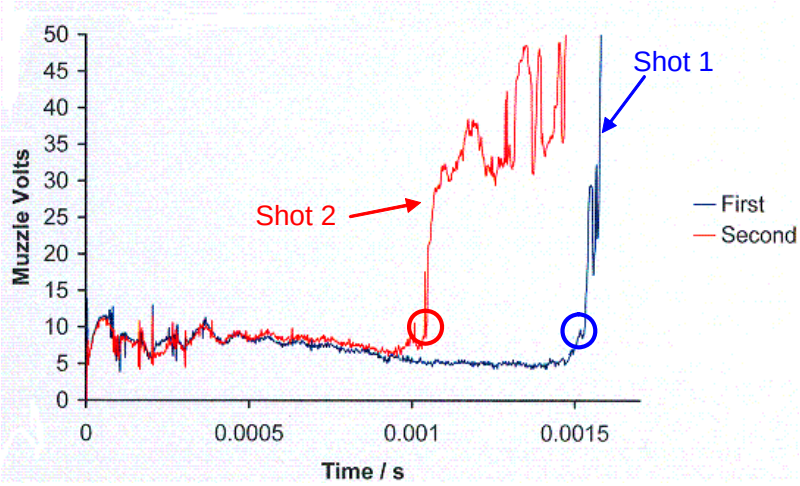

Figure 4.17 Muzzle voltage history of the two shots

In the analysis, the effect of the debris left on the rails was modeled by an increased surface roughness of the rail. Different roughness values were tested and the corresponding Q_{net} histories are plotted in Figure 4.18. The solid line represents the base case, with rail surface roughness equal to 1 micron. The pocket drains out at 1.5 ms, which agrees with the muzzle voltage measurement of shot 1 in Figure 4.17. A close match to the measurements of shot 2 is achieved with a roughness value of 10 microns. As can be seen from Figure 4.19, with increasing roughness, it is the increase of minimum film thickness at the beginning part of a launch that caused more lubricant to flow out from the pocket and resulted in an earlier transition.

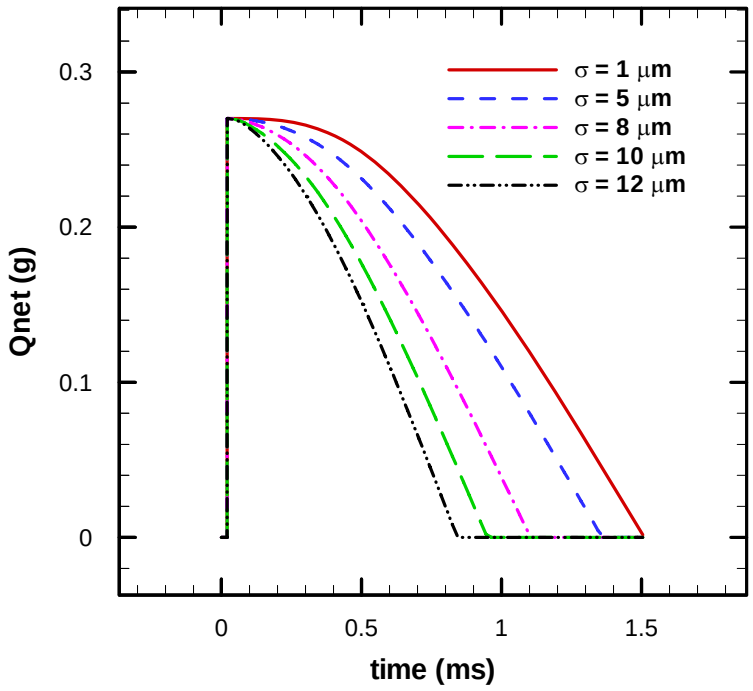

Figure 4.18 Pocket lubricant life with different rail surface roughness

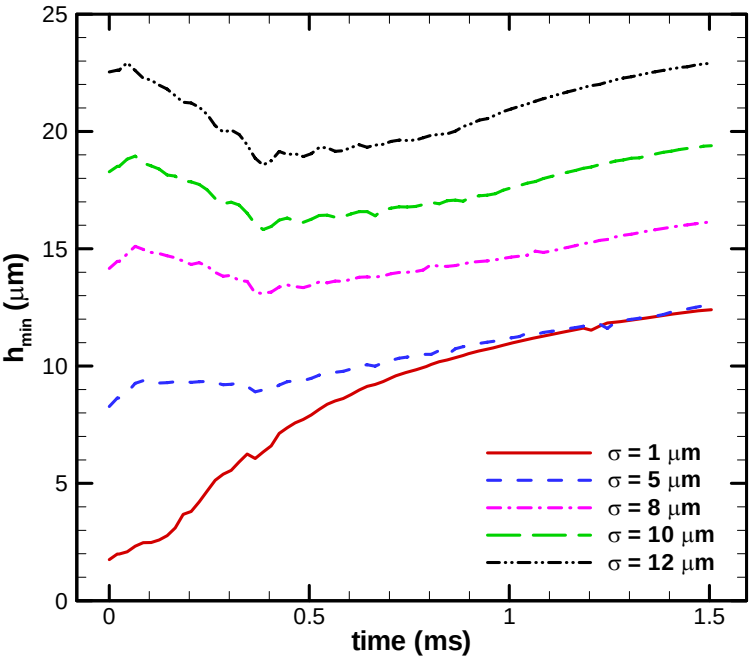

Figure 4.19 Minimum film thickness with different rail surface roughness

4.3 Rail Groove Evaluation

The surface roughness of both rails has been considered to be isotropic so far. An anisotropic rail surface with micro longitudinal grooves has been proposed by Dr. Bair for improved performance. However, the effects of such longitudinal grooves are unknown. Numerical studies have been conducted in this research to reveal and evaluate the influence of such grooves.

The micro longitudinal grooves are included in the METHD model by providing an increased surface roughness with a large surface characteristic value γ. γ was defined by Peklenik in 1967 as the ratio of the autocorrelation functions in the longitudinal and transverse directions. It represents the length-to-width ratio of a representative asperity. γ=1 corresponds to an isotropic surface and values larger than 1 correspond to longitudinal roughness patterns. The average flow model by Patir and Cheng is employed to consider surface anisotropy. The histories of the mass of fluid in the pocket (Q_{net}) are shown in Figure 4.20. For a surface with grooves on the order of one micron, an anisotropic surface (γ=9) produces similar lubrication patterns as an isotropic one. With increasing groove sizes (σ_r=10 microns and 30 microns), anisotropic rail surfaces helps to reduce lubricant consumption compared to isotropic surfaces with the same rms roughness. The reason for this is that a directional rail surface profile reduces the drag force on the fluid by the rails and thus less lubricant is removed by the rails. However, the amplitude of surface roughness plays a more dominant role in the lubrication process. The surface with smaller amplitude consumes less lubricant than one with larger amplitude, regardless of its surface orientation. Such results show that directional rail

surfaces with micro longitudinal grooves consume less lubricant during a launch compared to isotropic surfaces with the same amplitude. But since amplitude plays a more important role and grooving the surface will eventually increase surface amplitude, longitudinal grooves on the rail surface are not a beneficial design.

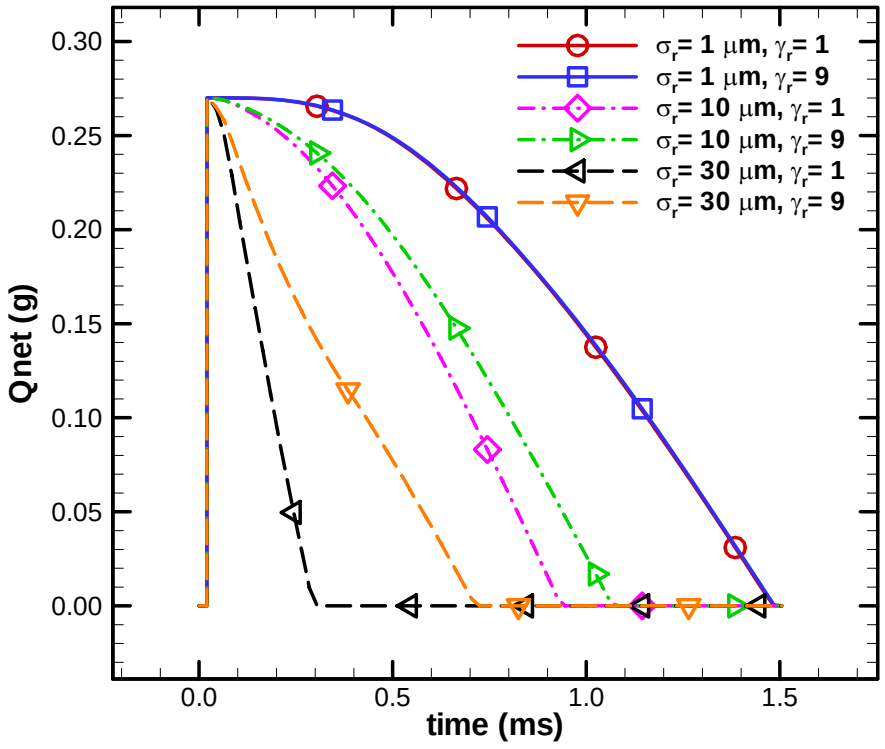

Figure 4.20 Pocket lubricant life with different micro rail surface grooves

4.4 Current Profile Evaluation

In the current Georgia Tech EML experimental device, a pre-charged capacitor is used to supply electric current for launches. The capacitor's discharge curve determines the current history. In the present base case configuration, the electric current increases very fast at the beginning of a launch and reaches its summit at 0.5 ms. The current

amperage then decreases gradually until it is cut off at the end of a launch, as shown in Figure 4.21a. However, this discharge pattern is not the only choice. Other discharge patterns are also available in different EML configurations. In an alternate experimental device with a longer rail set and a longer launch time, a different electric current history is applied. In this current profile, the current increases much slower than the base case configuration at the beginning of the launch. Its maximum magnitude is reached at about 1.5 ms and the current curve is much smoother than the one in the base case, as shown in Figure 5.21b.

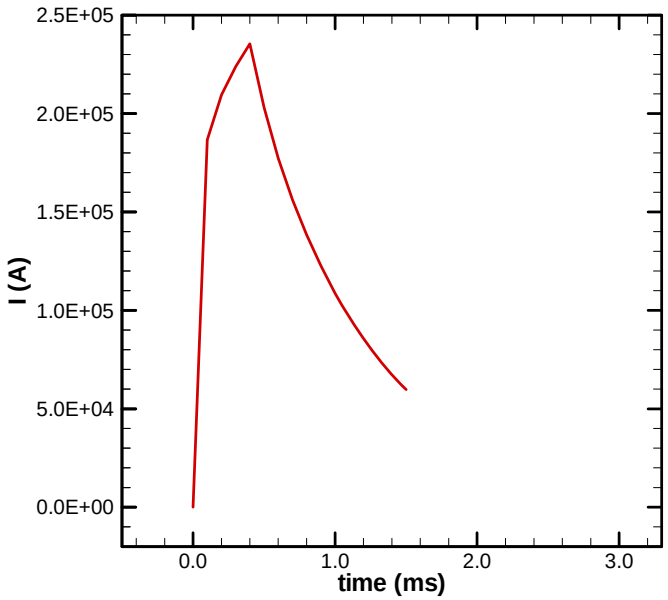

(a)

Figure 4.21 Electric current history of
(a) the Georgia Tech device and (b) the alternate device

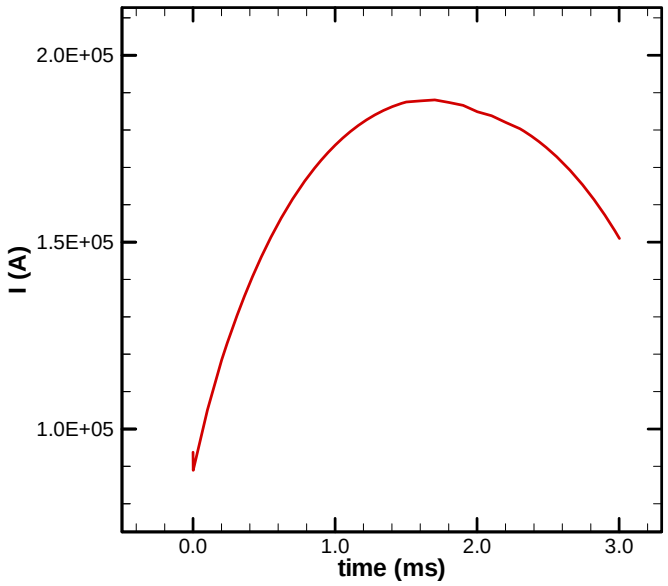

(b)

Figure 4.21 continued

In order to discover the more beneficial current profile for an EML application, the alternate current history is applied to the base case configuration and compared with the Georgia Tech current history. Figure 4.22 shows the armature acceleration and velocity histories with both current histories. With the Georgia Tech current discharge pattern, acceleration is very large at the beginning portion of the launch and decreases rapidly with the quickly dropping current (Figure 4.22.a). With the alternate discharge pattern, the armature acceleration grows with a much smoother gradient (Figure 4.22.b). In both cases, the armature achieves a velocity of about 1000 m/s at 1.5 ms.

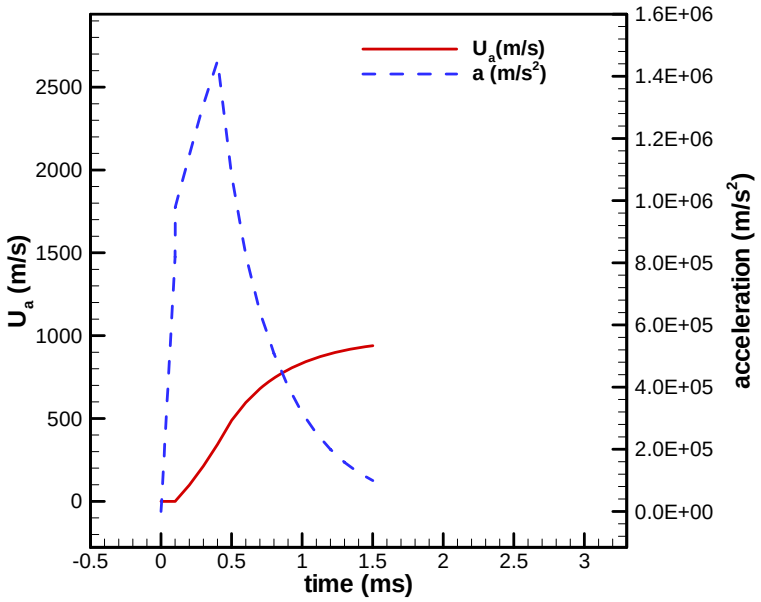

(a)

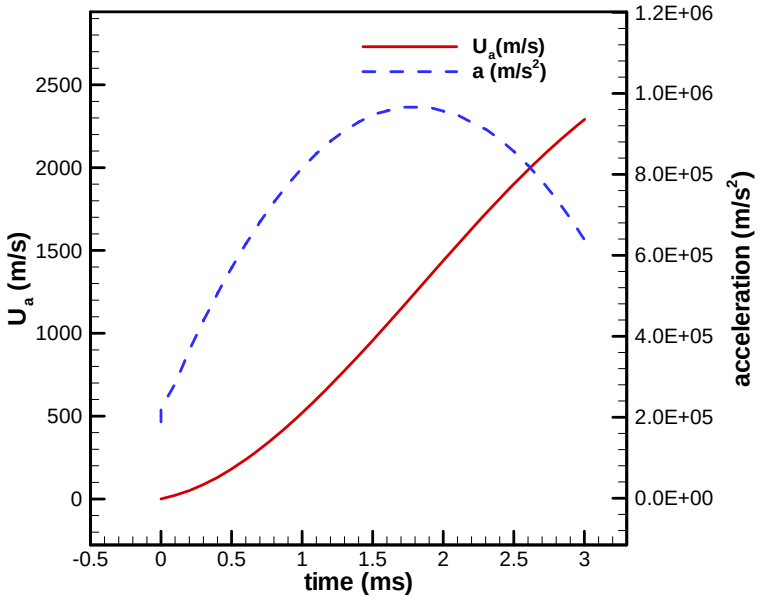

(b)

Figure 4.22 Velocity and acceleration history with
(a) the Georgia Tech current and (b) the alternate current

The histories of the mass flow amounts are illustrated in Figure 4.23. In both launches, lubricant in the reservoir is driven out immediately and excess fluid leaks from the front boundary. However, the pocket empties at 1.5 ms with the Georgia Tech current and at 2.0 ms with the alternate current. Since both launches accelerate the armature to 1000 m/s at 1.5 ms, such results reveal the fact that the alternate current discharge pattern is more effective in reducing lubricant consumption in a launch.

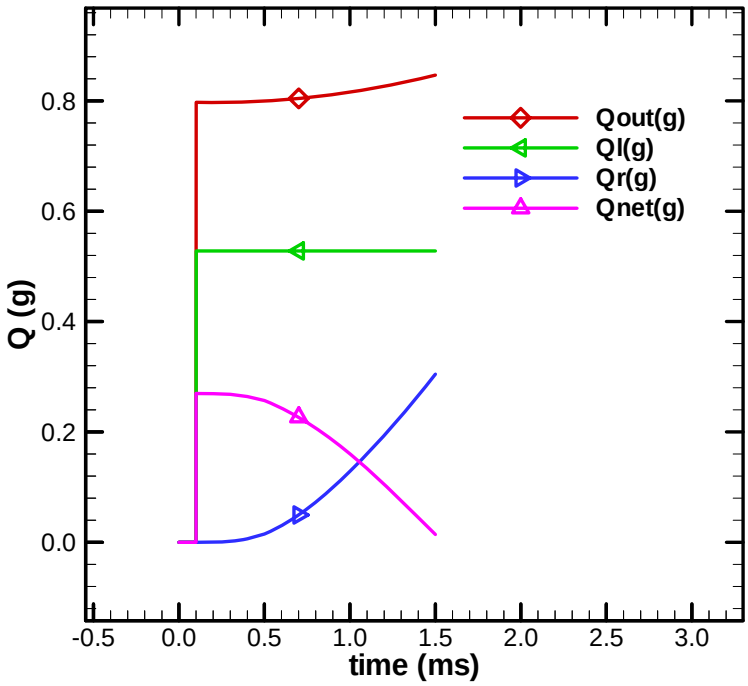

(a)

Figure 4.23 Mass flow amount history of
(a) the Georgia Tech current and (b) the alternate current

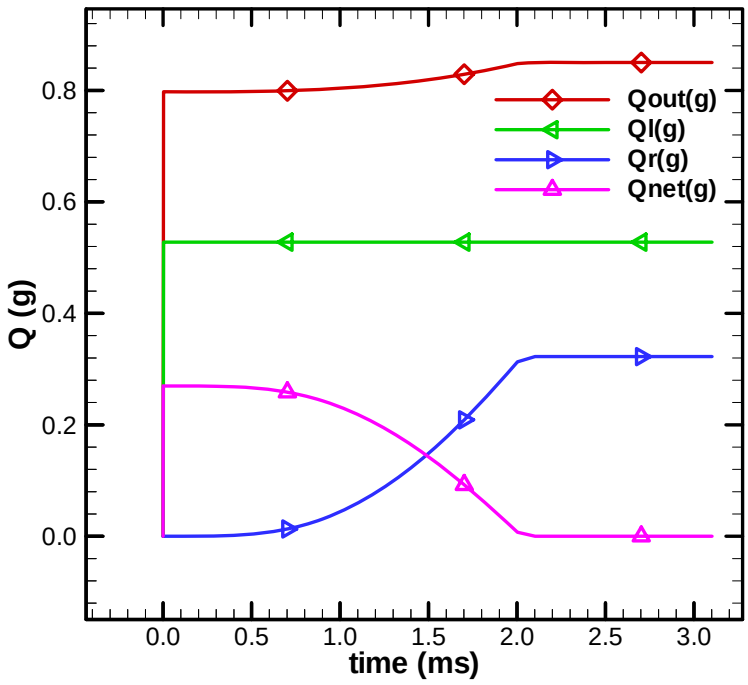

(b)

Figure 4.23 continued

The advantage of the alternate current history can be explained by the magnetic squeeze force on the armature leg. In the first 1.5 ms period of both launches, lubricant consumption increases with higher armature velocity. The alternate current profile provides an intensive electric current to the device in the latter half of the period, when a high velocity is achieved. This intensive electric current produces a much larger magnetic squeeze fore on the armature leg compared to the Georgia Tech current profile (Figure 4.24). Such a squeeze force helps to reduce the interface film thickness (Figure 4.25) and thus to reduce lubricant consumption. As a result, film thickness in the alternate launch is smaller than the original base case launch with the Georgia Tech current profile

throughout the launch history (Figure 4.26) and less lubricant is consumed in the alternate launch.

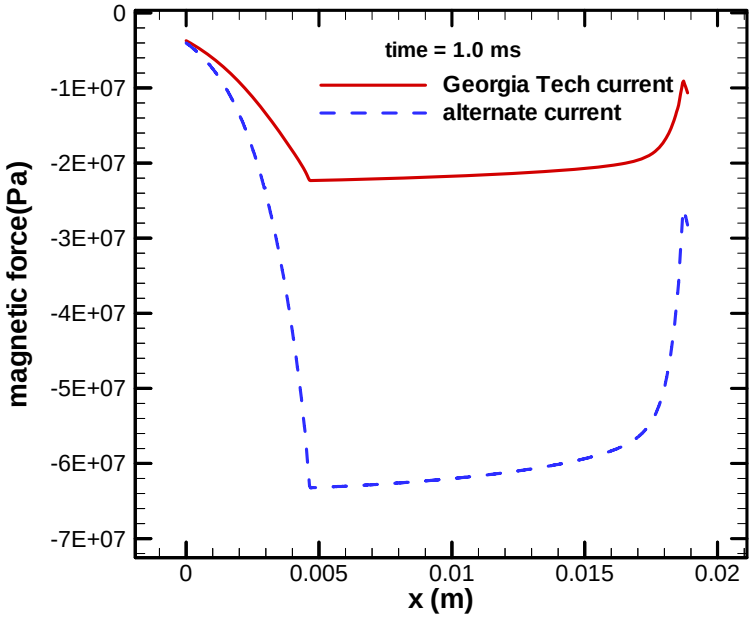

Figure 4.24 Distributed magnetic squeeze force on the armature leg at 1.0 ms with both current profiles

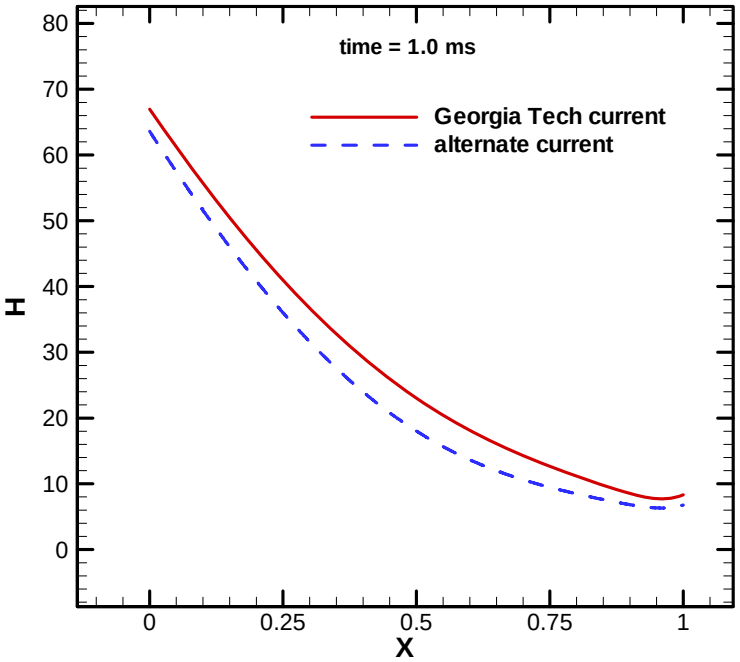

Figure 4.25 Nondimensional interface gap profile at 1.0 ms with both current profiles

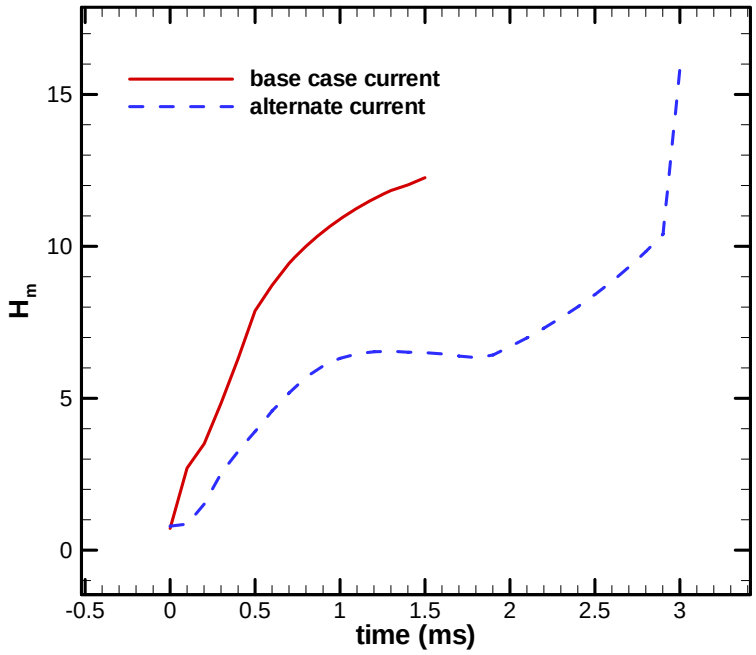

Figure 4.26 Minimum nondimensional film thickness history with both current profiles

Although the alternate current profile is found to be favorable to reduce interface lubricant consumption and to increase pocket lubricant life, the Georgia Tech current profile is applied to the rest of the analyses in order to be consistent with parallel experiments.

4.5 Reservoir Load Optimization

In order to reduce the armature weight, it is desirable to find the optimal reservoir design for a launch. Preliminary tests have shown that since the reservoir discharges quickly at the threshold of a launch, reservoir geometry parameters, such as diameter, do not have significant influence on the injection process. The only factor that can be

optimized is the initial reservoir lubricant load. Figure 4.27 shows the results of simulations in which the reservoir load was reduced from 1.7g, through 0.9g, to 0.5g. For all three cases, fluid in the reservoir empties up quickly (Figure 4.27a) and excess lubricant (if any) leaks from the front edge (Figure 4.27b). The amount of lubricant needed for the downstream flow for one side is about 0.34g (corresponding to a reservoir load of 0.68g), which is approximately the capacity of the pocket plus the lubricant stored in the injection conduit, as shown in Figure 4.27c. Therefore, fully filling the pocket at the beginning of the launch is required and is also sufficient for a successful launch without the occurrence of arcing. With insufficient reservoir capacity (m_{load}=0.5 g for this case), the pocket drains out before the launch is accomplished (Figure 4.27d) and arcing will take place due to the lack of downstream lubricant supply (Figure 4.27c).

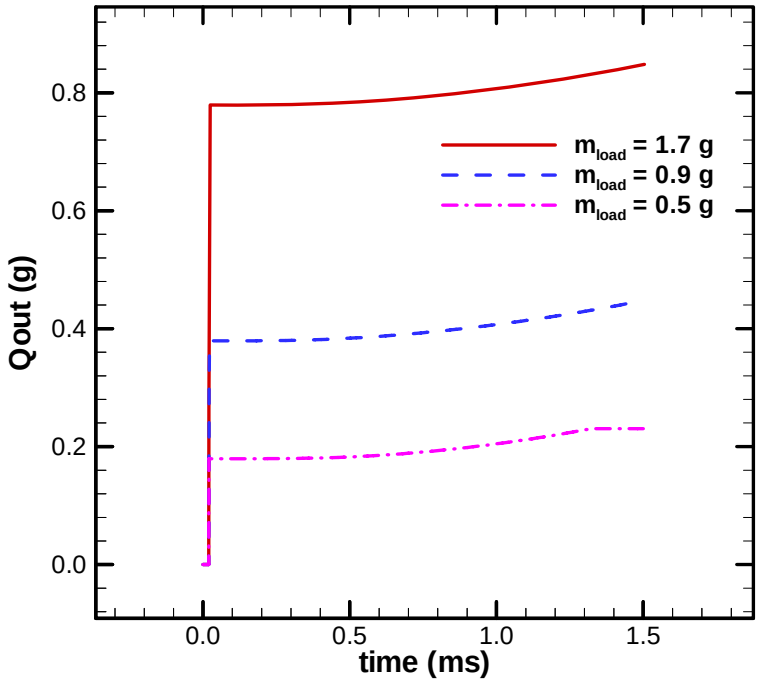

(a)

Figure 4.27 Mass flow amount histories with different reservoir loads: (a) Q_{out}, (b) Q_l, (c) Q_r, and (d) Q_{net}

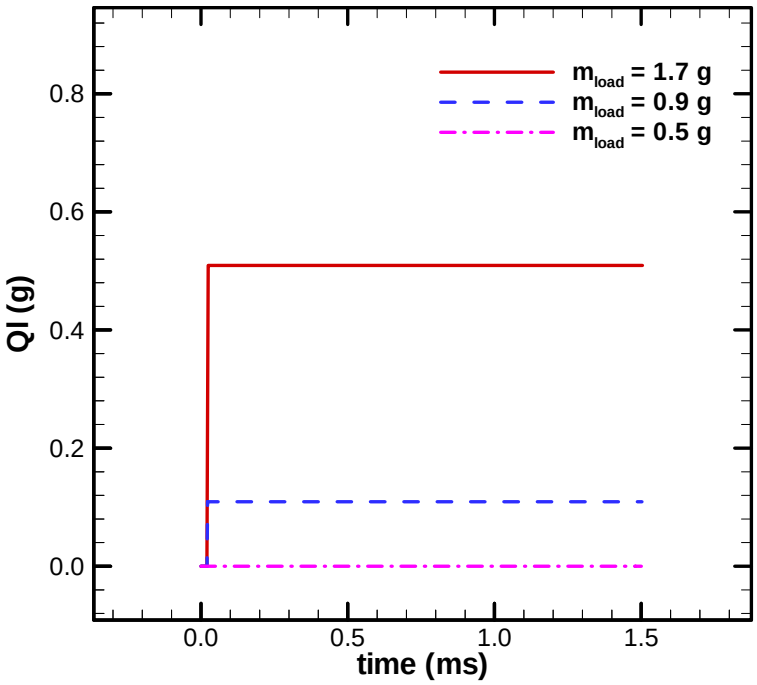

(b)

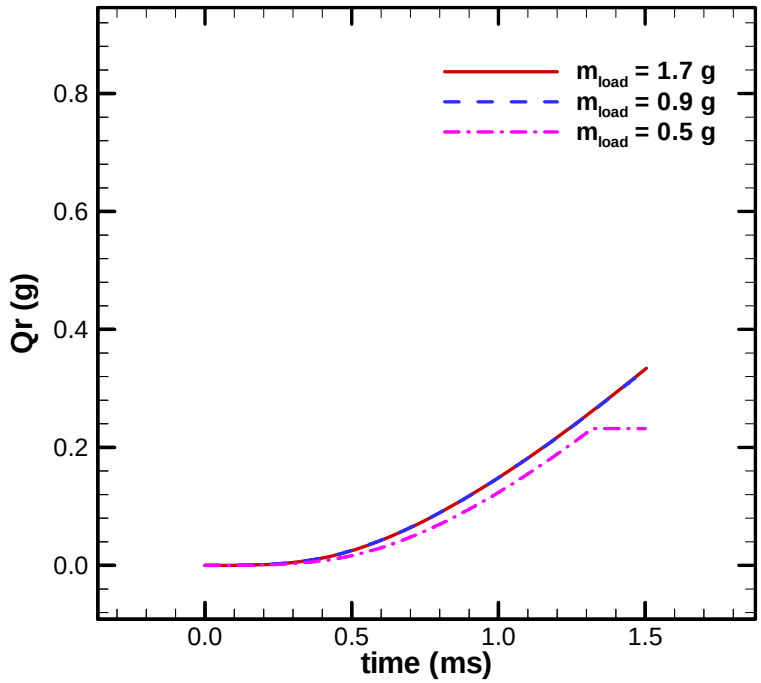

(c)

Figure 4.27 continued

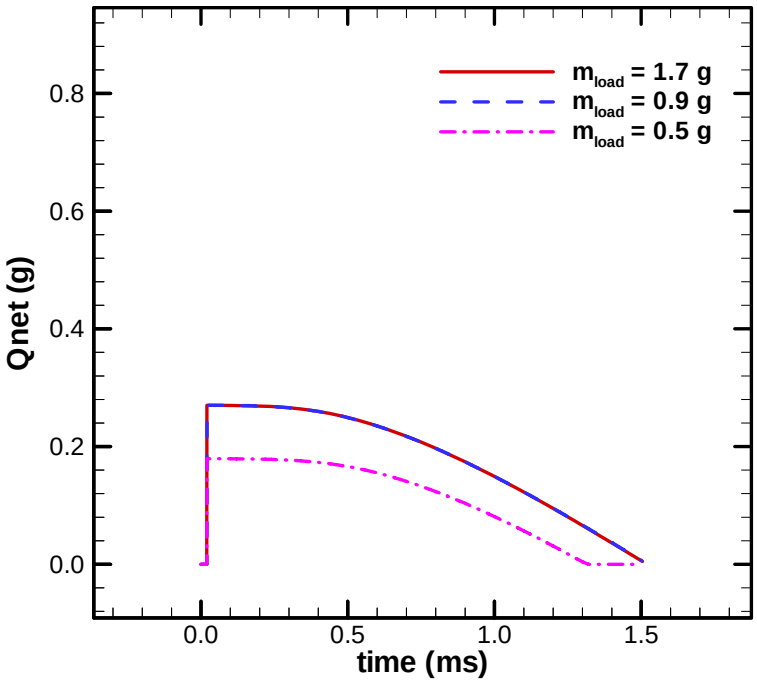

(d)

Figure 4.27 continued

Experiments were performed by Dr. Bair based on these numerical predictions. Figure 4.28 shows the muzzle voltage histories for the three different reservoir loads. These muzzle voltage histories agree with the previous numerical predictions, with no transitions for the first two launches and an early transition (indicated by a muzzle voltage jump before the launch ends) at about 1.3 ms for the launch with an insufficient reservoir load of 0.5 g, which is exactly when the pocket is drained out in the numerical simulation.

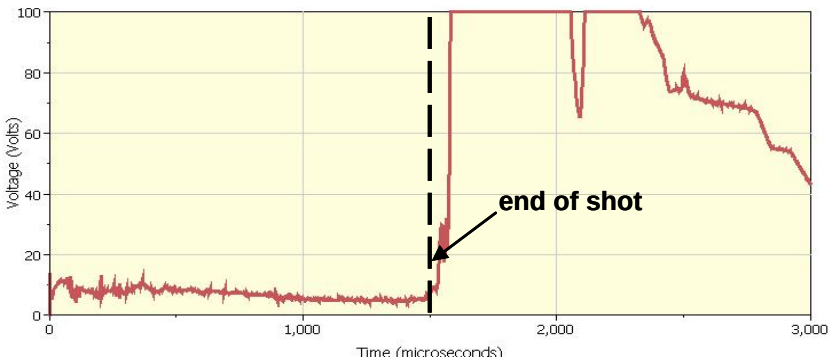

(a)

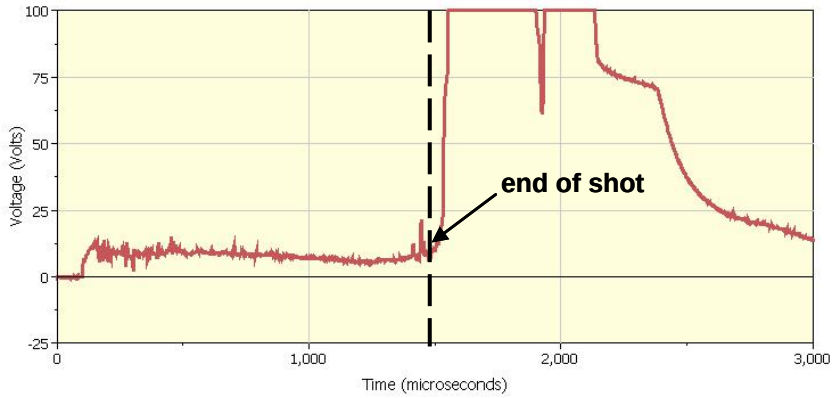

(b)

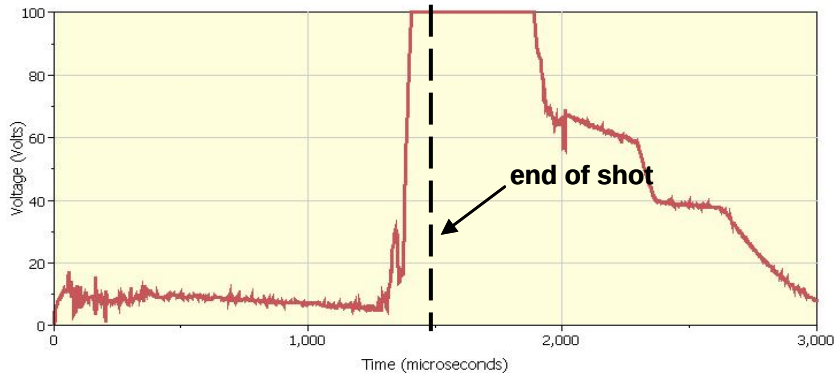

(c)

Figure 4.28 Muzzle voltage histories with different reservoir loads: a) 1.7 g b) 0.9 g c) 0.5 g

Based on the above discussion, both numerical and experimental results suggest that the initial reservoir load should be determined by the lubricant consumption in the injection and lubrication process of a launch. The METHD model developed in this study provides a good prediction of the launch history. An optimized reservoir load of 0.68 g is suggested by the METHD model for the current configuration.

4.6 Geometric Parameter Evaluation

It has been pointed out in Chapter 3 that a converging gap with an upstream injection is favorable for effective injection. As shown in previous results, a well designed pocket is critical to effectively lubricate the armature-rail interface. The effects of pocket geometric parameters, such as pocket location/lubrication length, pocket geometry, pocket capacity, and injection conduit diameter, must be studied to provide design guidance. Design parameters, such as L the lubrication length, L_{pk} the pocket length, *h1* and *h2* the pocket depths and D_h the injection conduit diameter as shown in Figure 4.29, will be studied in this section. To simplify the problem, it is assumed that the changes in all the parameters studied in this section do not have a significant influence on the electromagnetic field and armature stiffness. That is, the original geometry is used for EMAG and deformation calculations.

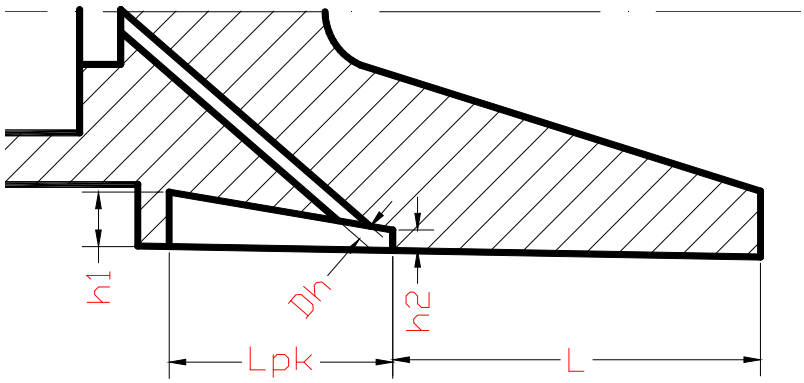

Figure 4.29 Schematic of the injection conduit and pocket

4.6.1 Lubrication Length

In the present configuration, the pocket is located close to the front of the interface. Moving the pocket backwards will reduce the lubrication length at the interface and thus is likely to reduce lubricant consumption. However, such modifications must be carefully examined to make sure that electrical conduction across the interface is not affected. Figure 4.30 shows the electric current density in the film for the current configuration at different times. In the film, the current concentrates at the trailing edge. The density decreases rapidly along the film towards the front. As listed in Table 4.2, the electric current density at the midway of the film reduces to below 10% of its value at the trailing end. Therefore, the influence on electrical conduction by moving the pocket towards the trailing edge until half way of the current lubricant length is negligible.

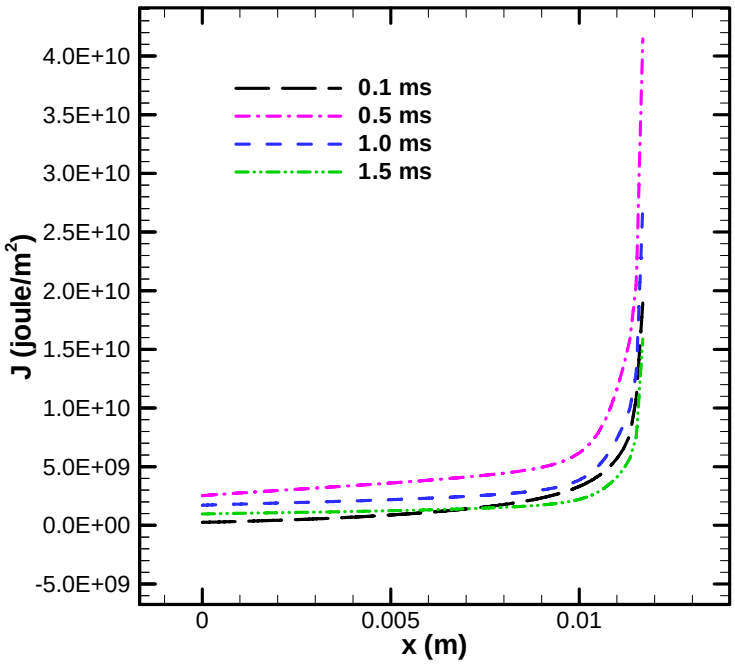

Figure 4.30 Electric current density distribution in the film at different times

Table 4.2 Electric Current Density in the Film at Different Locations

t (ms)	J (joule/m^2)		J_2/J_1
	$x_1=L$	$x_2=L/2$	
0.1	1.764E10	1.071E9	**6.1%**
0.5	3.808E10	3.811E9	**10.0%**
1.0	2.469E10	2.293E9	**9.3%**
1.5	1.452E10	1.308E9	**9.0%**

Another concern about moving the pocket is that the pocket should also be away from contact regions so that the contact status will not be affected by the pocket. Table 4.3 contains the non-dimensional film thickness at the mid-point of the current

lubrication length. The film thickness at this location is much larger than the mixed-lubrication limit of 3 and no contact occurs close to this region throughout the launch.

Table 4.3 Nondimensional Midpoint Film Thickness at Different Times

t (ms)	***H* at *x*=0.5**
0.1	15.11
0.5	16.73
1.0	22.36
1.5	25.21

In addition to the above requirements, it should also be noted that by changing the lubrication length, the lubrication pressure profile and interface contact status in the whole interface gap are affected. A reduced lubrication length produces less fluid pressure and a severer contact status is more likely to occur at the interface, especially when the system is under large magnetic stresses. Such close contact induces a higher contact pressure and a larger friction force. The contact pressure needs to be controlled to prevent material yielding. Friction should also be restricted in order to reduce resistance and possible wear at the interface. Furthermore, locating the pocket away from the large deformation regions also prevents any potential pocket capacity change. Therefore, any potential pocket location design should be simulated to check the contact and friction status at the interface.

Launches with different pocket locations by reducing the lubrication length to 80%, 60% and 50% of its original value are simulated and results are plotted in Figure 4.31. With a pocket closer to the rear end and a shorter lubrication length, the film thickness in

the interface gap is reduced (Figure 4.32) and less lubricant is consumed. Lubricant injected into the pocket lasts much longer than was the case in the original design.

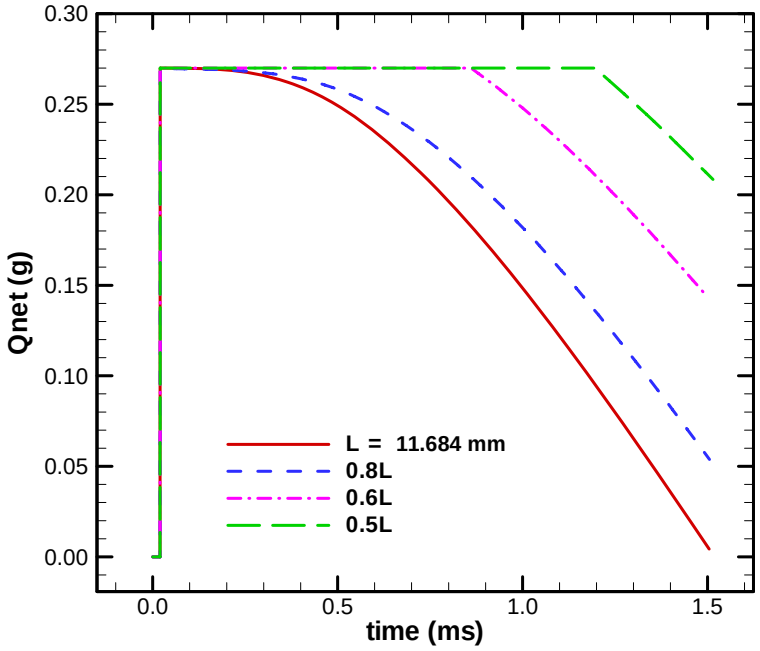

Figure 4.31 Pocket lubricant life with different lubrication lengths

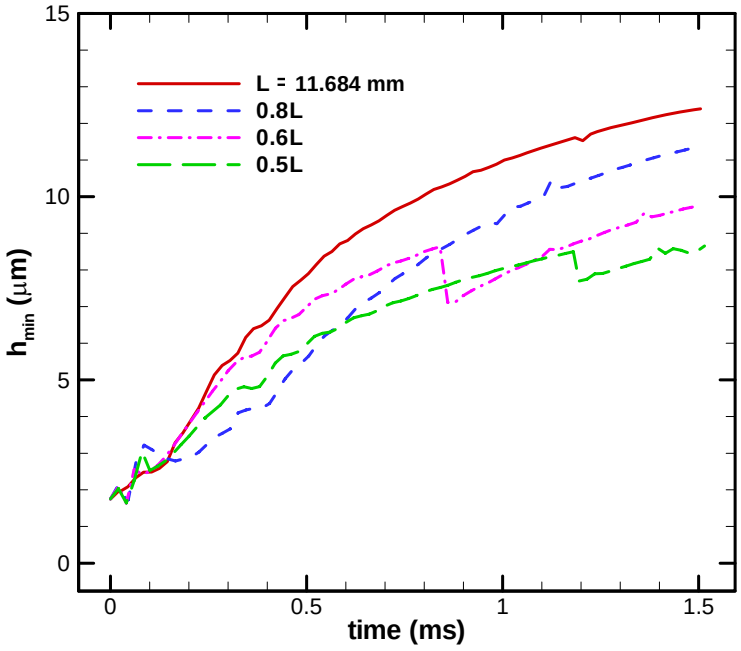

Figure 4.32 Minimum nondimensional film thickness history with different lubrication lengths

In summary, reduction of the lubrication length at the interface is beneficial to decrease the lubrication consumption at the interface. But it must be carefully examined in order to control contact, prevent material yielding and reduce friction and wear.

4.6.2 Pocket Geometry

It is indisputable that increasing pocket capacity helps to provide more lubricant to the interface during a launch. However, an increase in the pocket capacity also requires more lubricant to be loaded before a shot. The influence of an increased pocket capacity is examined below. Different pocket capacities have been simulated by increasing the depths of the pocket as listed in Table 4.4. The pocket depths of the base case (Test 1) are 1.016 mm (0.04 inch) at the front and 0.635 mm (0.025 inch) at the back. Tests 2 and 3 increase the pocket capacity by 25% and 50% by changing the pocket depths, while keeping the same gap length. The reservoir load is 1.7 g for all the three tests. Histories of the lubricant mass amount in the pocket (Q_{net}) are plotted in Figure 4.33. The same amount of lubricant is consumed although the pocket capacity is different in the three tests. More lubricant remains at the end of the launch with an enlarged pocket.

Table 4.4 Pocket Depths with Different Capacity Designs

Test	*h1* (mm)	*h2* (mm)	m_{pk} (g)	Capacity change
1	1.016	0.635	0.27	--
2	1.2222	0.8412	0.3375	+25%
3	1.4285	1.0478	0.4050	+50%

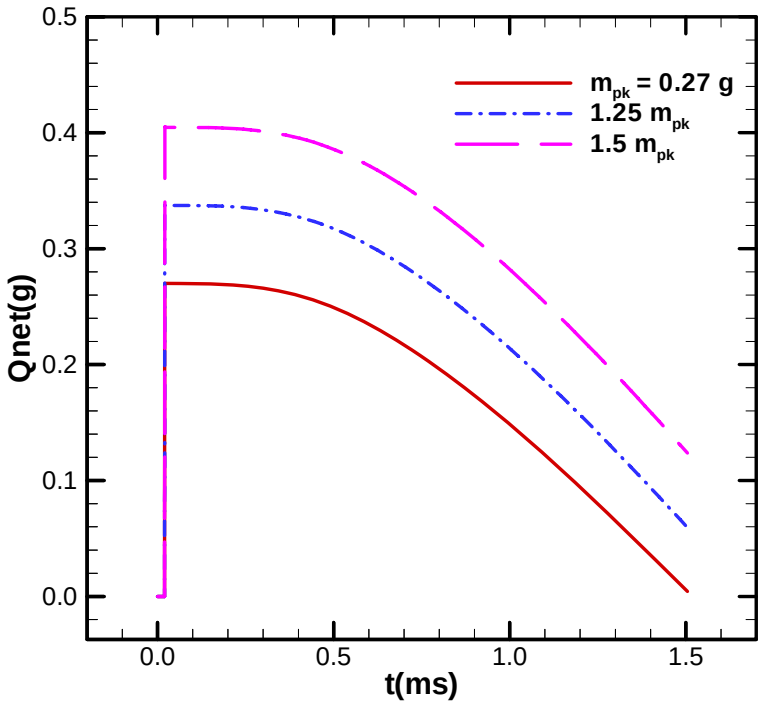

Figure 4.33 Pocket lubricant life with different pocket sizes

The effects of the pocket capacity shown above are very natural and within our expectation. However, the way the pocket aspect ratio affects the lubrication process is unknown yet. Such effects are studied by varying the pocket depths *h1* and *h2* while maintaining the same pocket size. As listed in Table 4.5, four different pocket depth combinations are tested. The results are shown in Figure 4.34. Very little difference is found in these four tests. Generally, a diverging pocket geometry is favorable to improve pocket lubricant life. However, its influence is limited. Considering that in practice a converging pocket is more beneficial to direct fluid to the interface gap entrance, the converging profile used in current design does not need to be changed.

Table 4.5 Pocket Depths with Different Aspect Ratios

Test	*h1* (mm)	*h2* (mm)	m_{pk} (g)
1	1.27	0.381	0.27
2	1.016	0.635	0.27
3	0.8255	0.8255	0.27
4	0.635	1.016	0.27

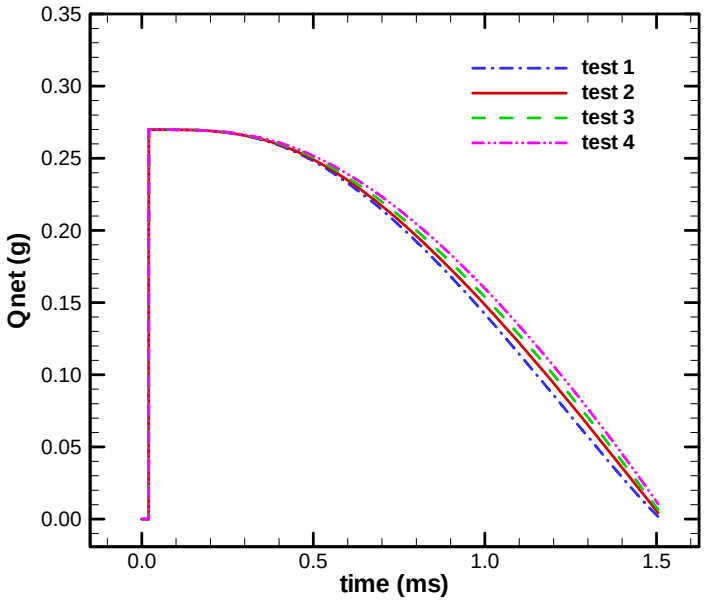

Figure 4.34 Pocket lubricant life with different aspect ratios

4.6.3 Injection Conduit Diameter

The results from the base case reveal that lubricant in the reservoir is completely injected into the pocket at the beginning of a launch. If the injection process can be slowed down and the injection speed can be controlled to match the lubricant consumption rate at the interface, the reservoir load will last much longer and the pocket geometry can be reduced.

A series of injection conduit diameters with the base case configuration are investigated for this purpose and the results are shown in Figure 4.35. The diameter is first reduced from its original value 1.09 mm (0.43 inch) to 25.4 μm (0.001 inch) (Figure 4.35a). With this conduit size, the reservoir lubricant life is dramatically improved to 0.7 ms. With a further reduced conduit diameter of 19.05 μm (0.00075 inch), lubricant in the reservoir lasts for the entire launch and the pocket is still full in the end (Figure 4.35b). Much less lubricant leaks out from the front edge with this conduit diameter. When the conduit diameter is finally reduced to 12.7 μm (0.0005 inch) (Figure 4.35c), the injection process is severely depressed. Although lubricant from the reservoir charges the pocket at the beginning of the launch, the injection speed cannot match up with the lubricant consumption rate as the sliding speed goes up. As a result, the pocket drains out at 1.3 ms and insufficient lubricant is supplied to the interface from injection.

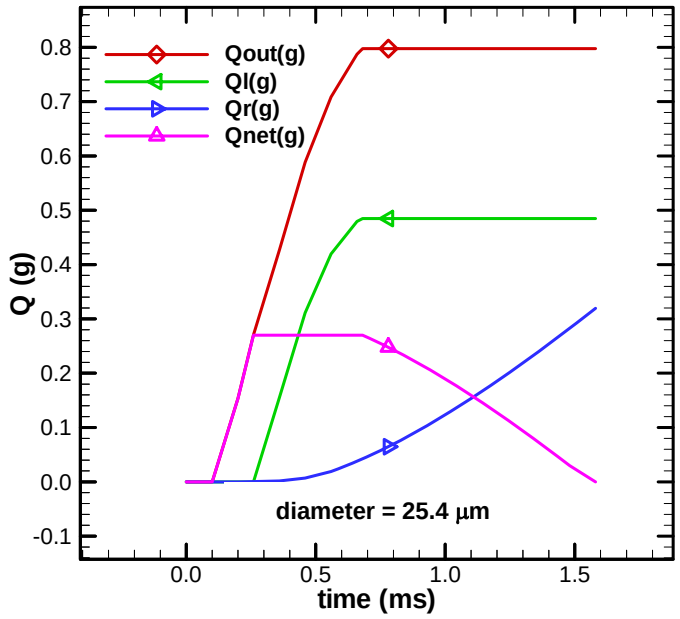

(a)

Figure 4.35 Mass flow amount histories with different injection conduit diameters

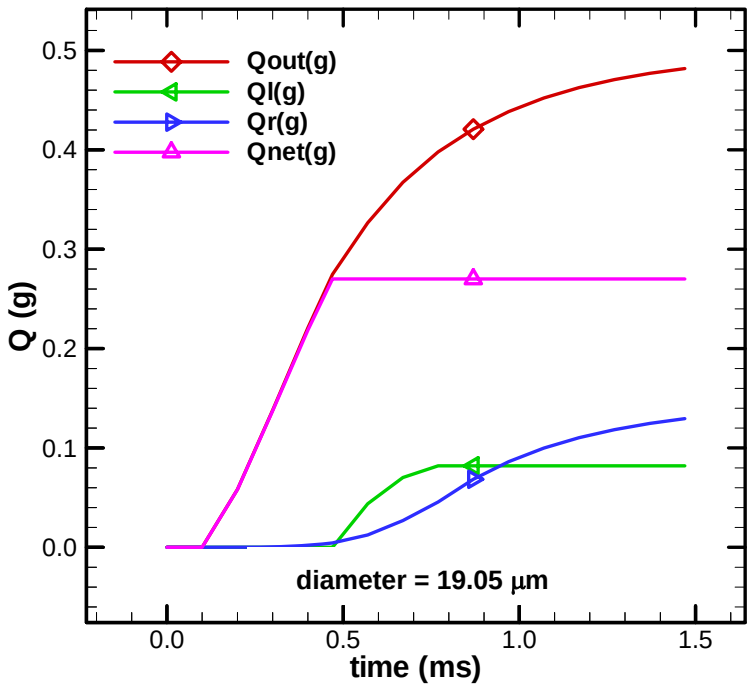

(b)

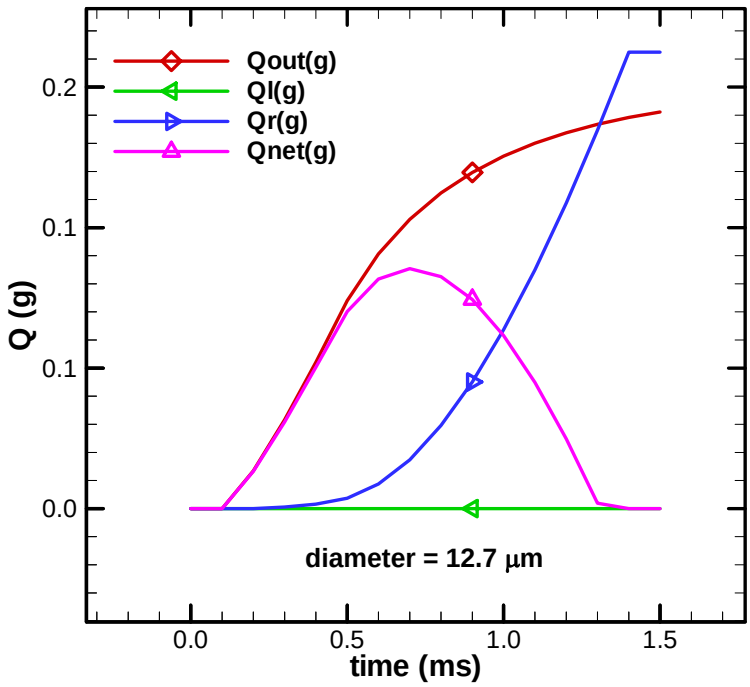

(c)

Figure 4.35 continued

This injection conduit diameter study reveals that by choosing an appropriate diameter, the injection process can be controlled so that reservoir lubricant life can be improved and pocket geometry can be reduced. However, several factors must be considered in practice. First, injection conduit surface roughness also plays an active role and depresses injection when the conduit diameter falls into its range. Second, breakthrough of the reservoir membrane that initially holds the lubricant will be very difficult with a tiny injection conduit. The last and the most important thing is that conduits with such a small diameter are hard to machine and can be easily contaminated. Therefore, reducing the injection conduit diameter is not a practical design to regulate the flow.

4.7 Recommended Design Procedure

From the parametric study performed above, it is found that design factors such as lubrication length, pocket capacity, pocket length, pocket aspect ration and injection conduit diameter have different influences on the lubrication process. To achieve a better injection and lubrication process, the procedure for designing an optimal pocket using the METHD model developed in this study is recommended as:

1. The lubrication length needs to be determined first. Although a shorter length helps to reduce the lubricant consumption at the interface, a desirable fluid pressure by an appropriate lubrication length must be maintained at the interface in order to: 1) ensure a good conduction of electric current across the interface;

2) prevent excessive interface contact to avoid material yielding and reduce friction and wear.

2. Once the lubrication length is determined from a series of parametric simulations, the minimum reservoir load can be derived by balancing the amount of fluid flowing out from the trailing edge of the interface.
3. With the optimized reservoir load and lubrication length, the pocket size can be adjusted to accommodate the lubricant consumption in the launch process.
4. The complete set of optimized parameters needs to be simulated with the METHD model to consider all the changes. If any problems are found, steps 1, 2, and 3 need to be repeated to achieve a proper design.

Because of the elastic material behavior and non-melting assumptions used in this study, the METHD model is only applicable to launches without material yielding and melting. In practice, the optimized design obtained from the design procedure given above must be validated and calibrated with experiments.

4.8 Scaling Study

In order to study the scale effects, a scaling simulation was performed in this study. In this case, the dimensions of the device (both the armature and the rails) are doubled. The armature mass and pocket capacity increased accordingly. The electric current is increased with the square of the dimensional increase. Reservoir load was initially chosen to be increased with the cube of the dimensional increase, i.e. 13.6 g. Its optimal value was determined later according to the optimal pocket design. With these modified

parameters, results for the launch simulated in Section 3.1 were regenerated with a new 3 meter long rail set.

Figure 4.36 shows the scaled electric current history. The maximum current was increased to four times the original value (from 2.5E5 A in Figure 4.2 to 1E6 A in Figure 4.36). The shot in the base case only covered a one meter long rail set and the current was cut off after 1.5 ms because the armature had left the muzzle. To provide a reasonable current history for the scaled shot, the current was extended beyond 1.5 ms with a least-square fit.

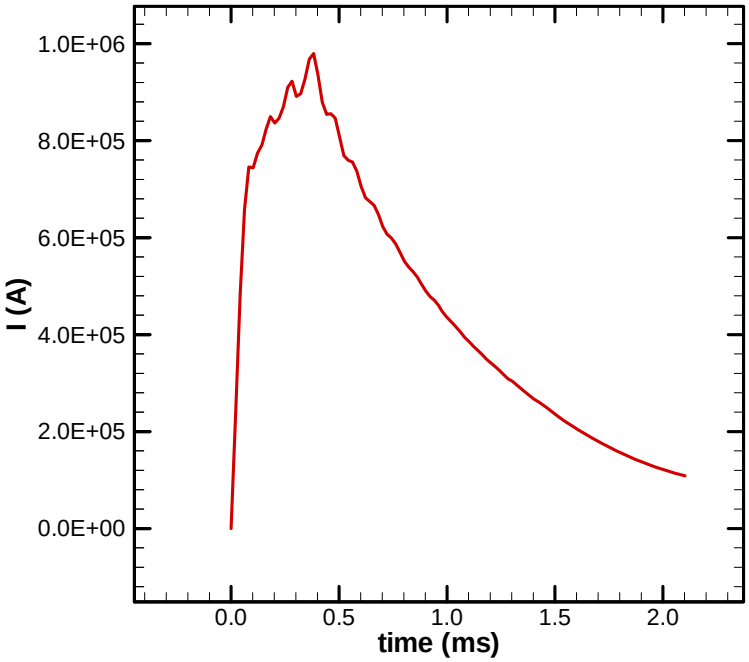

Figure 4.36 Scaled electric current history

The armature acceleration and velocity history for this scaled simulation are shown in Figures 4.37 and 4.38. The propulsion energy increases with the square of the current increase, i.e. 16 times the base case. The mass of the armature increases with the cube of the dimension change, i.e. 8 times the base case. Therefore, a doubled acceleration is

observed in the scaled study. With this doubled acceleration and extended rail length, a final velocity of 2000 m/s is achieved at the muzzle in 2.1 ms. No yielding is observed in this scaled configuration. The thermal analysis indicates temperature above the melting point in a small region of the armature at the trailing edge due to intense joule heating, which violates the non-melting assumption of this study. However, the cross section area of the melting region is less than 2 mm^2 and results obtained from the METHD model is still believed to provide a close prediction.

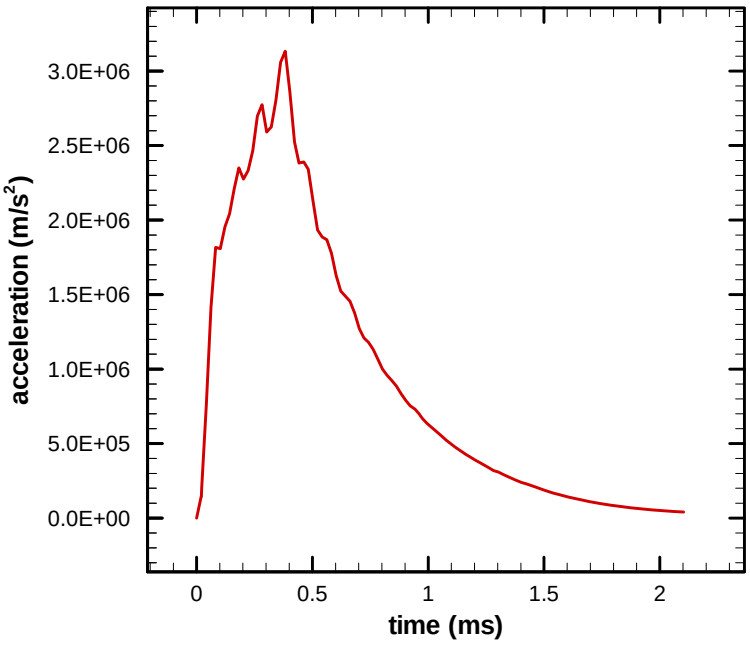

Figure 4.37 Armature acceleration history of the scaled configuration

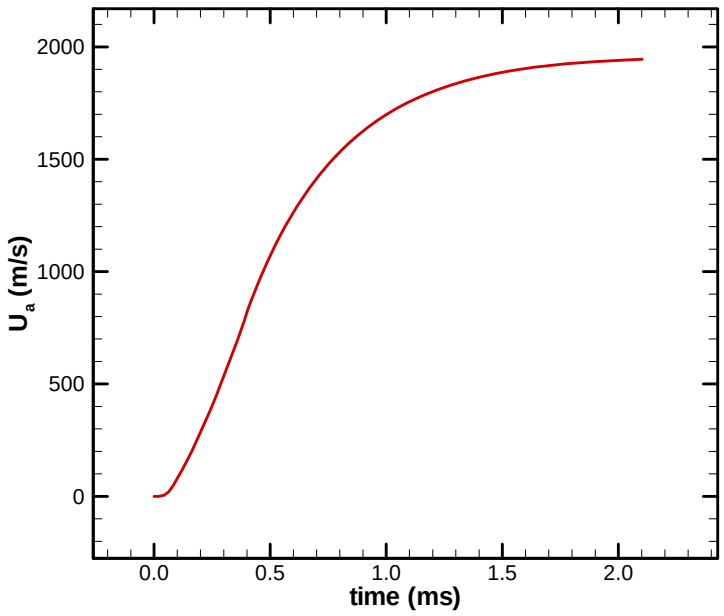

Figure 4.38 Armature velocity history of the scaled configuration

Histories of the mass flow amounts at different boundaries for this scaled study are plotted in Figure 4.39. A similar injection process is observed in this scaled simulation compared to the base case. Although the pocket capacity increased to 8 times the original size, the pocket drains out at 2.0 ms, about 0.1 ms before the launch ends. Compared to the lubrication process of the base case, less lubricant is consumed at the beginning portion of the shot ($t<0.5$ ms) in the scaled run. This is because the amplified electromagnetic field produces a much larger magnetic squeeze force on the armature leg and as a result the interface gap height (Figure 4.40) is smaller than the base case (Figure 4.15). However, in the last portion of the scaled launch ($t>1.5$ ms), the increased sliding velocity and lubrication length generate high fluid pressures and the interface gap is widely opened. Large lubricant consumption is observed in this period.

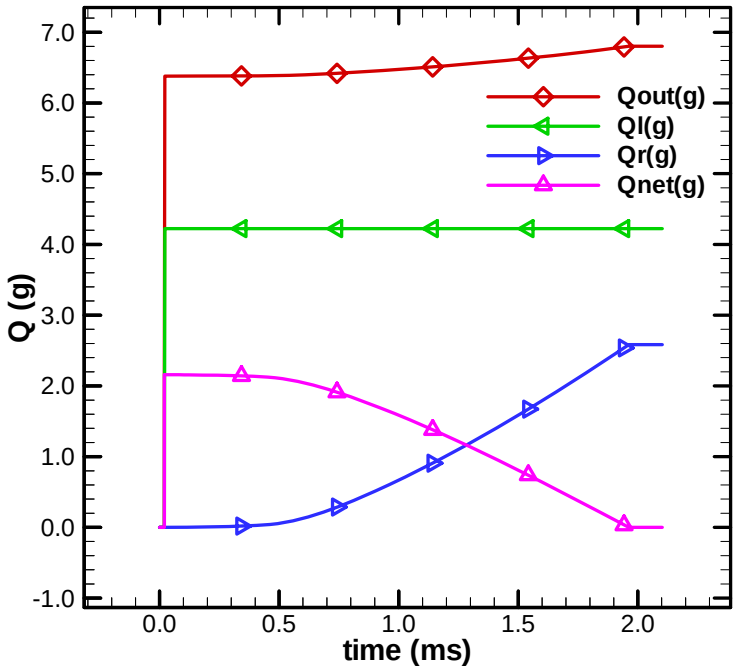

Figure 4.39 Mass flow amount history of the scaled configuration

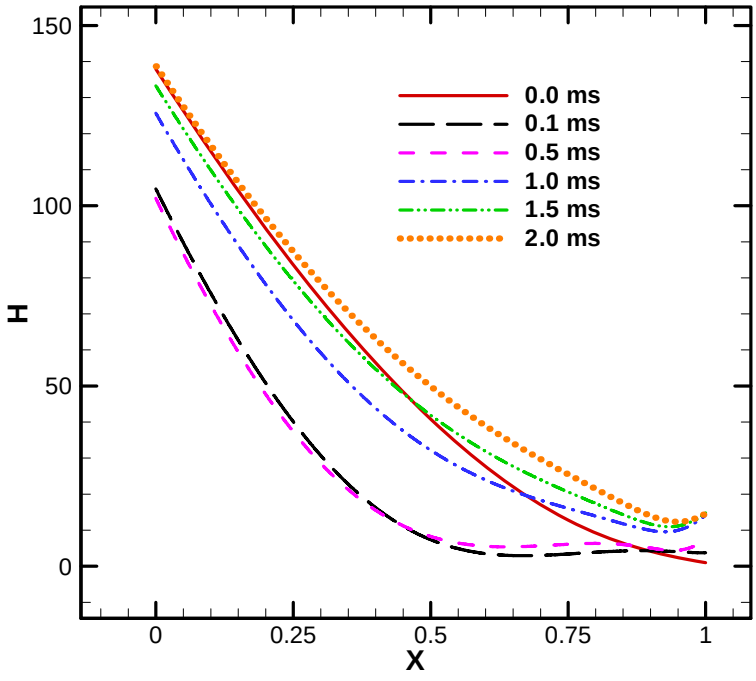

Figure 4.40 Nondimensional interface gap profiles at different times of the scaled configuration

4.9 Injection Design Optimization

4.9.1 Base Case

Following the design guidelines presented in Section 3.6, a series of simulations were conducted and the optimal design parameters were determined for the base case configuration. A lubrication length of 8.89 mm (0.35 inch) is found to significantly reduce interface lubrication consumption to 0.25 g while still maintaining acceptable contact pressure and friction force (Figure 4.41). Figure 4.42 shows the interface gap profiles at different times for this optimized design. In these gap profiles, film thickness is reduced compared to the base case, and the pocket is away from the contact region with a minimum non-dimensional film thickness of 30. The pocket is then redesigned by reducing its notch depths based on this updated lubricant consumption. Details of the modifications are listed in Table 4.6. With this new design, the required pocket load is reduced from 1.7 g to 0.5 g, with a 71% decrease. The corresponding mass flow amounts of this optimized base case are plotted in Figure 4.43. Note that in this improved design, there is no loss of lubricant through the upstream edge (Q_l equals zero).

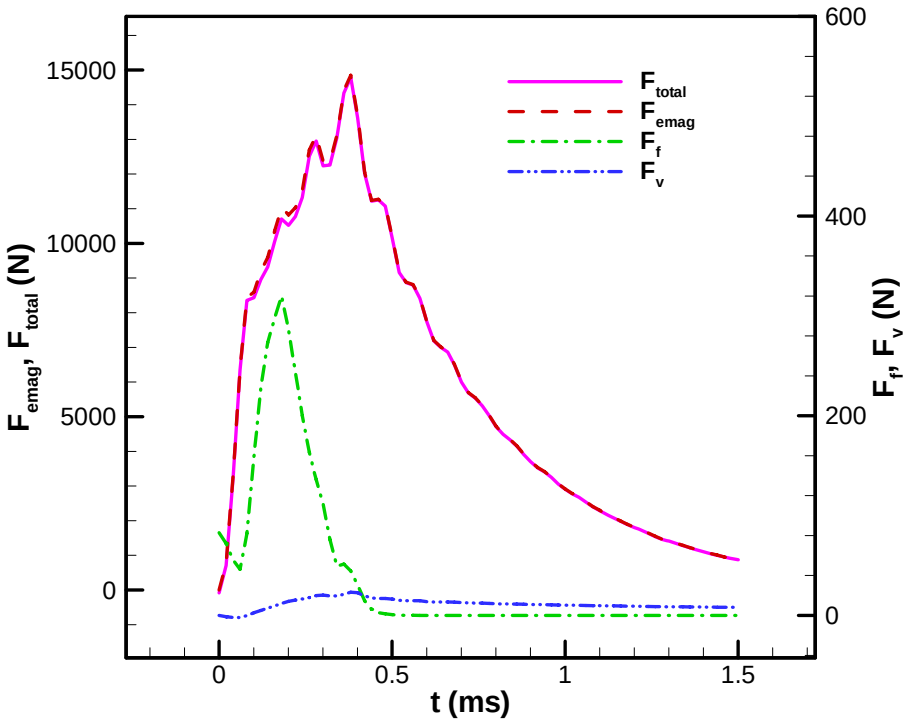

Figure 4.41 *x*-direction armature force history of the optimized base case configuration

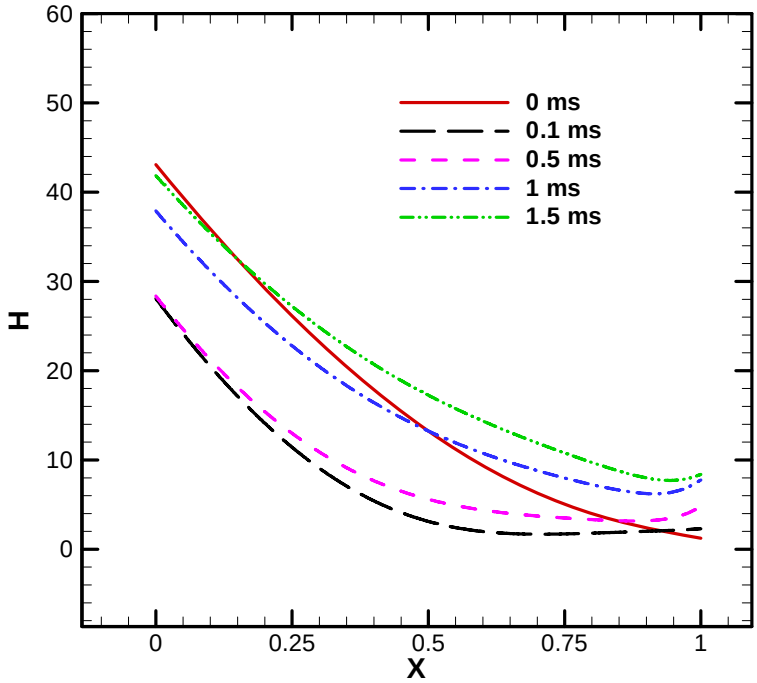

Figure 4.42 Nondimensional interface gap profiles at different times of the optimized base case configuration

Table 4.6 Original and Optimized Parameters of the Base Case

	Original design	**Optimized design**	**Change**
L	11.684 mm (0.46 inch)	8.89 mm (0.35 inch)	-24%
h1	1.016 mm (0.04 inch)	0.762 mm (0.03 inch)	-25%
h2	0.635 mm (0.025 inch)	0.381 mm (0.015 inch)	-40%
L_{pk}	6.604 mm (0.26 inch)	6.604 mm (0.26 inch)	0%
m_{pk} **(g)**	0.270	0.187	-31%
m_{load} **(g)**	**1.7**	**0.5**	**-71%**

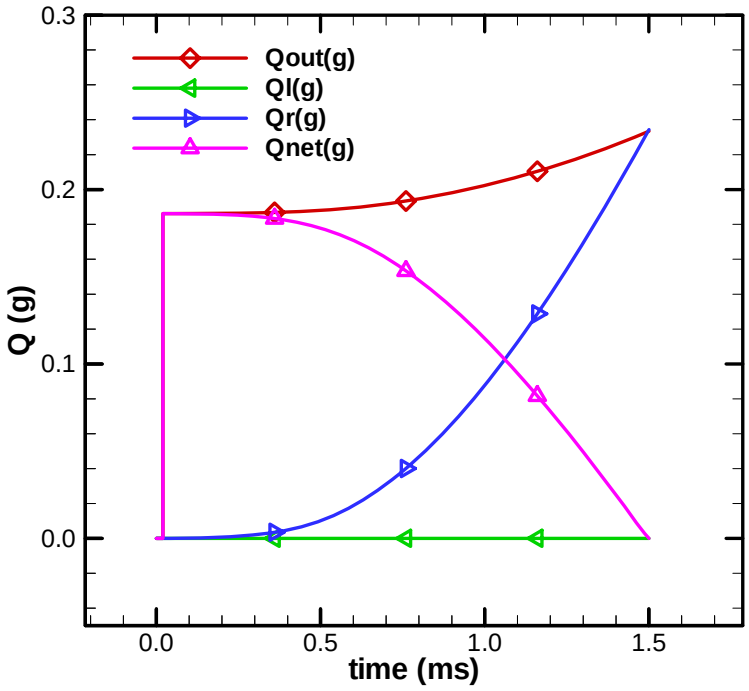

Figure 4.43 Mass flow amount history of the optimized base case configuration

4.9.2 Scaled Configuration

The same optimization procedures were conducted for the scaled configuration. In the optimized design, the pocket geometry is retained and the lubrication length is reduced to 21.03 mm (0.828 inch). Optimization details are listed in Table 4.7. In this scaled configuration, the magnetic squeeze force on the armature leg increases with the square of the dimensional change. This increased magnetic force results in a severe contact condition and a large friction force (Figure 4.44) at the interface. Therefore, in this optimized scaled configuration, the lubrication length cannot be reduced to the same ratio as the optimized base case. A sufficient lubrication length is desired to generate enough fluid lifting pressure and to reduce contact and friction. Interface gap profiles are plotted in Figure 4.45. Intensive contact is observed at 0.1 ms and 0.5 ms. With this optimized design, reservoir load was reduced from 13.6 g to 5.1 g with a 62.5% decrease and the lubrication life was extended from 2.0 ms to the entire launch period, as shown in Figure 4.46. The optimized parameters for this scaled case demonstrate that any modifications to the EML system configuration need to be studied in a case by case manner. A simple scaling of the original dimensions might not be appropriate for the changed configuration.

Table 4.7 Original and Optimized Parameters of the Scaled Configuration

	Original design	**Optimized design**	**Change**
L	23.37 mm (0.92 inch)	21.03 mm (0.828 inch)	-24%
h1	2.032 mm (0.08 inch)	1.524 mm (0.06 inch)	-25%
h2	1.27 mm (0.05 inch)	0.762 mm (0.03 inch)	-40%
L_{pk}	13.21 mm (0.52 inch)	13.21 mm (0.52 inch)	0%
m_{pk} **(g)**	2.16	2.07	-31%
m_{load} **(g)**	**13.6**	**5.1**	**-62.5%**

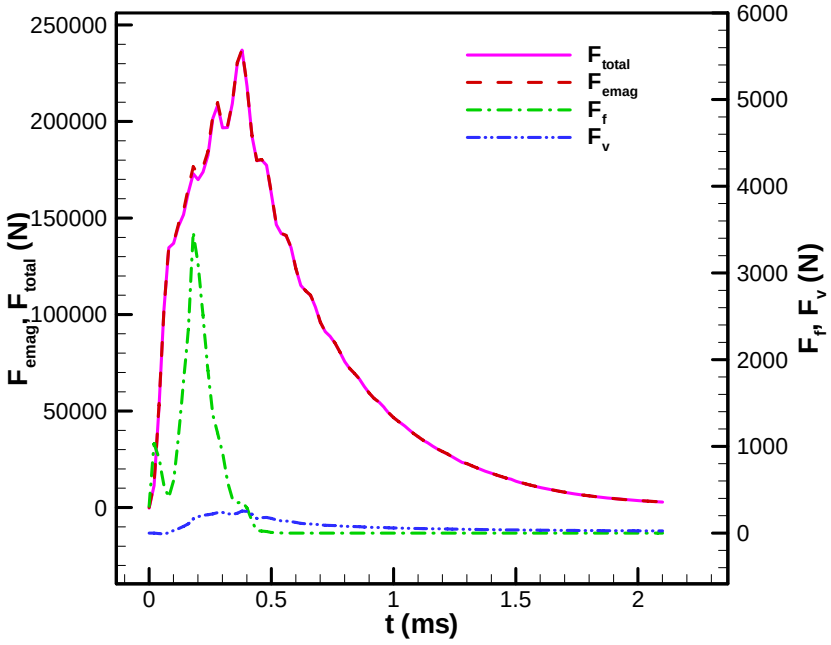

Figure 4.44 *x*-direction armature force history of the optimized scaled configuration

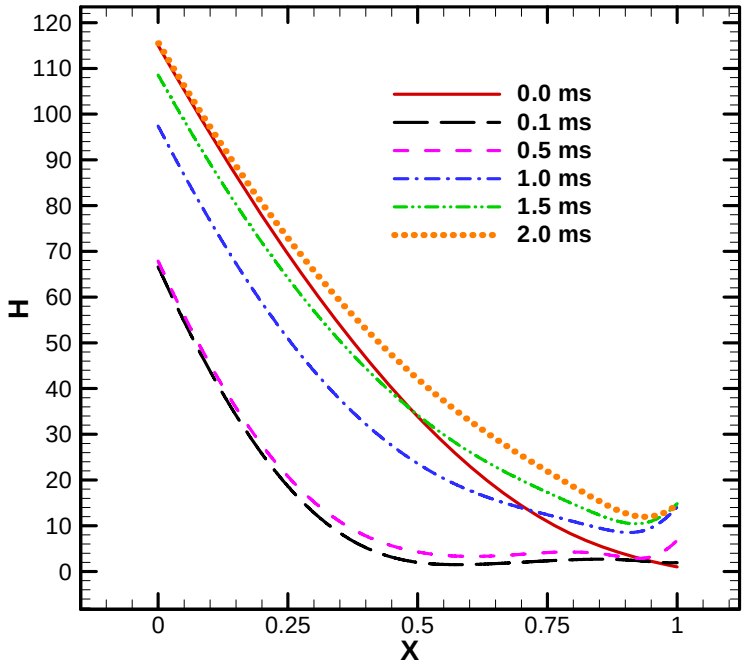

Figure 4.45 Nondimensional interface gap profile at different times of the optimized scaled configuration

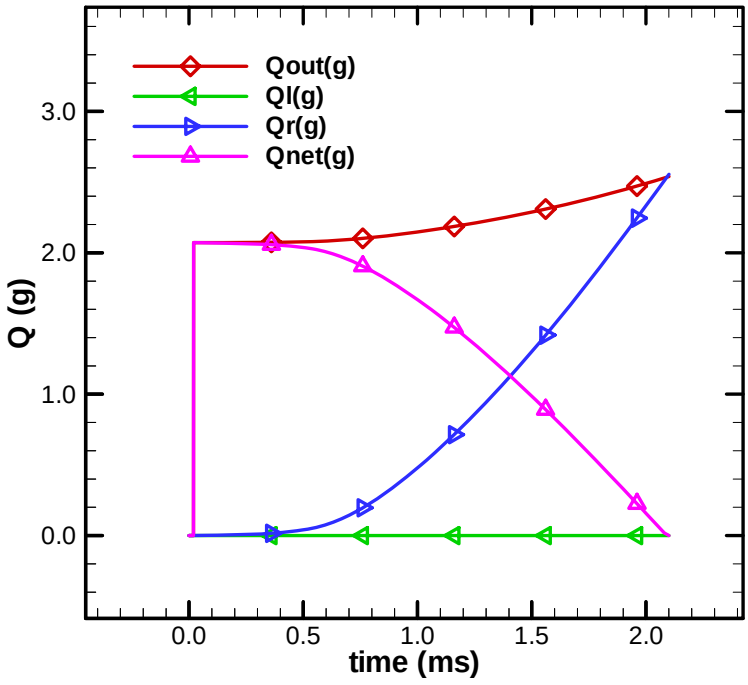

Figure 4.46 Mass flow amount history of the optimized scaled configuration

CHAPTER 5

CONCLUSIONS

The behavior at the armature-rail interface in an electromagnetic launcher system is critical to a successful launch. An analytical model to describe such an interface is quite a challenge because the launch process is dynamic and is under extreme magnetic stresses. The tightly coupled multiple physics fields at the interface add even more difficulties to the analysis. Very few analytical models, especially those that consider lubricant injection, are found in the literature.

Three analytical models are developed in this study in a progressive manner. The final magneto-elastothermohydrodynamic (METHD) model successfully couples a comprehensive fluid lubrication model with the electromagnetic effects, thermal effects, contact, and deformation. The METHD model is validated with both experimental measurements and commercial FEA software results.

The history of a typical launch is simulated with the METHD model as the base case. Distributions of magnetic flux density, electric current density, magnetic body force, and temperature field are calculated. Armature acceleration and velocity history is predicted, and calculated armature location history is validated with experimental measurements. Detailed injection, lubrication and launch processes are revealed: lubricant loaded in the reservoir is found to quickly discharge into the pockets; excess lubricant leaks from the front edge of the interface. The pocket behaves as a spare reservoir and provides fluid to lubricate the interface throughout the entire launch process. Contact and friction are observed at the beginning of the launch. However, as the sliding speed increases with time, the interface gap is lifted open by the fluid pressure, and contact is eliminated at the

interface. Such details can only be obtained from an analytical model, and they provide valuable information to guide future injection system design.

With the validated METHD model, a troubleshooting study is conducted to identify the cause of a failed launch. The debris left on the rails after a previous launch is found to introduce the problem by increasing rail surface roughness and interface lubricant consumption. Potential rail designs with micro grooves are examined by simulations with different surface profiles. It is found that the grooves are not a favorable design because they increase rail surface roughness and reduce pocket lubricant life. Two electric current histories with the same armature and rail configuration are examined and the alternate current profile is found to be favorable to reduce interface lubricant consumption and to increase pocket lubricant life from 1.5 ms to 2.0 ms, compared to the original Georgia Tech current profile. Based on the injection and lubrication patterns discovered in the METHD model, a series of different initial reservoir loads are simulated, and results are validated with experimental muzzle voltage measurements. The current design of a 1.7 g initial load is found to be excessive, but a 0.5 g load is found to be insufficient in both simulation and experimental results.

The effects of several injection design parameters are studied in a parametric way. A shorter lubrication length is found to be the most effective design to decrease interface lubricant consumption and extend pocket lubricant life. A large pocket size guarantees a longer lubricant life with no surprise but the aspect ratio of the pocket is found to have very limited influence on lubricant consumption. A smaller injection conduit is likely to slow down the injection process and extend reservoir lubricant life. It is also found that a reduction in injection conduit diameter is not a practical design to regulate the flow

because of the effects of the injection conduit inner surface roughness, reservoir membrane and difficulties in machining and operation.

Based on the findings of the parametric study, a recommended design procedure is developed in this study to guide the design of an injection system, in order to ensure sufficient lubrication throughout the entire launch process while requiring minimum reservoir load. Optimized parameters are found following this design procedure for both the base case and a scaled configuration. The optimized designs reduced the lubricant consumption by 71% for the base case and 62.5% for the scaled configuration, compared to the original design.

The analytical model developed in this study provides an effective tool to predict and optimize the performance of a potential EML injection design under given operating conditions. The boundaries of acceptable operation, especially the initial reservoir load, can be found using the model. However, it is still necessary to incorporate this analytical model with experimental study to produce the most accurate information for practice.

APPENDIX A

OPTIMUM GAP PROFILE AND INJECTION LOCATION – MHD MODEL

As mentioned in Section 3.1.4, combinations of different interface gap profiles (converging, parallel, and diverging) and different injection locations (upstream, center, and downstream) are simulated with a direct injection design to determine the most beneficial injection configuration. Numerical results have been generated for the parameters in Table A.1. Figure A.1 contains streamline patterns for a converging film with $\theta_1=0.1^o$. The pattern in Figure A.1a is for the case of a film without injection (e.g. if the lubricant is deposited on the rail); it contains a region of reverse flow. In this study, a successful injection is identified to be the injection to completely feed the interface without any fluid flowing in from the leading edge. Figures A.1b-d, for injection at an upstream location, show that an injection speed of 10 m/s is insufficient to fill the interface with lubricant, 50 m/s almost fills the interface, while 100 m/s completely fills the interface. Figure A.2 shows the pressure distribution with these injections. Injection increases fluid pressure in the film, especially at the injection location. Figure A.3 depicts the mass flow rates along the gap under different injections. The mass flow rate remains constant except at the location of injection. Comparison of different injection speeds shows that increasing injection in this case doesn't have a notable influence on the mass flow rate at the trailing edge. Excess fluid flows out from the leading edge and could be saved if a pocket exists at the front to hold fluid. Figures A.4-A.6, for injection at a center location, show similar results. However, Figure A.5 shows that much higher film

pressures are developed with center injection than with upstream injection; thus, center injection requires higher injection power. A higher injection speed in center injection also increases the mass flow at both edges as shown in Figure A.6.

Table A.1 Parameter Values in Direct Injection Case

U	1000 m/s
μ	2.0×10^{-3} Pa-s
a	8.0×10^{5} m/s2
P_c	0.0 Pa
P_{ref}	10^{5} Pa
P_{mt}	1.0×10^{8} Pa
ρ_c	6.0×10^{3} kg/m^3
L	11.48×10^{-3} m (0.46 in.)
L_{inj}	1.6×10^{-4} m (1/160 in.)
θ_1	0.1^o, 0.0^o, -0.1^o
h_0	4.24×10^{-6} m
σ	1.414×10^{-6} m

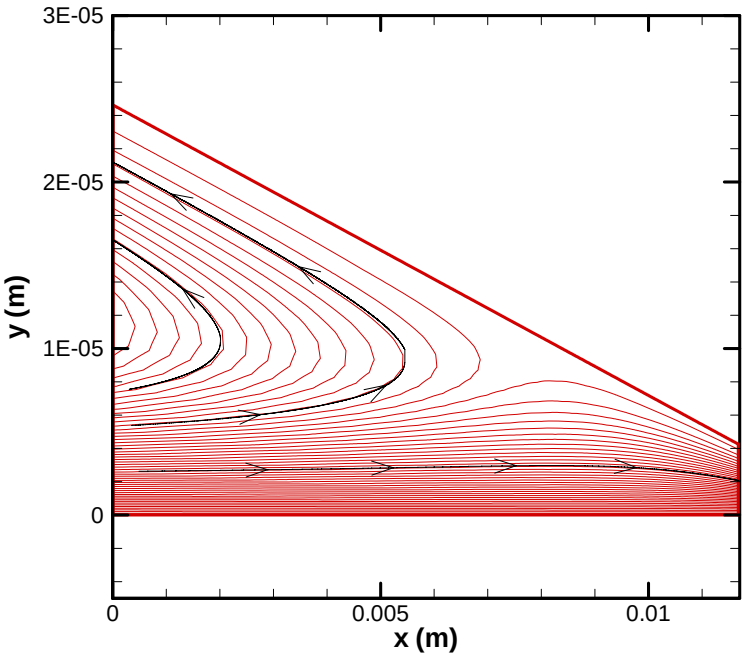

(a) V=0 (No Injection)

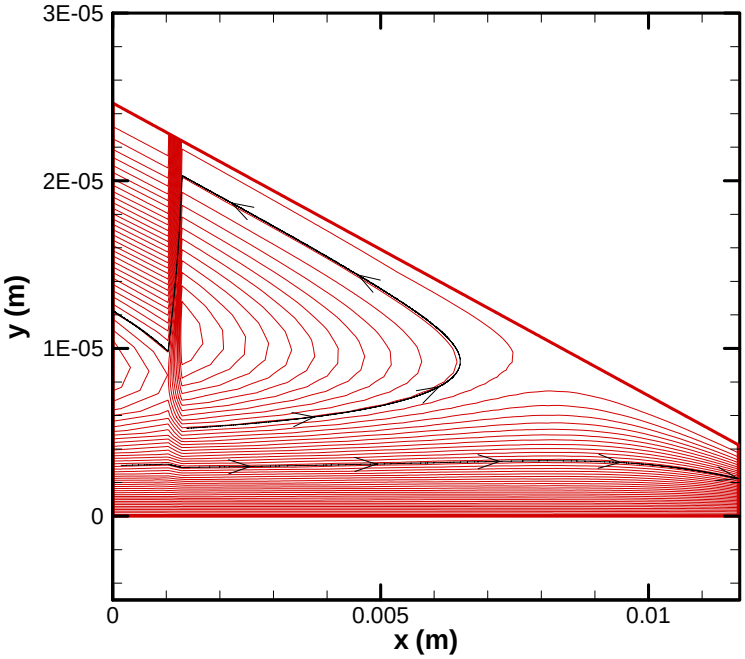

(b) V=10 m/s

Figure A.1 Stream lines with different upstream injection speed for a converging gap (θ_1 = 0.10 ^{o})

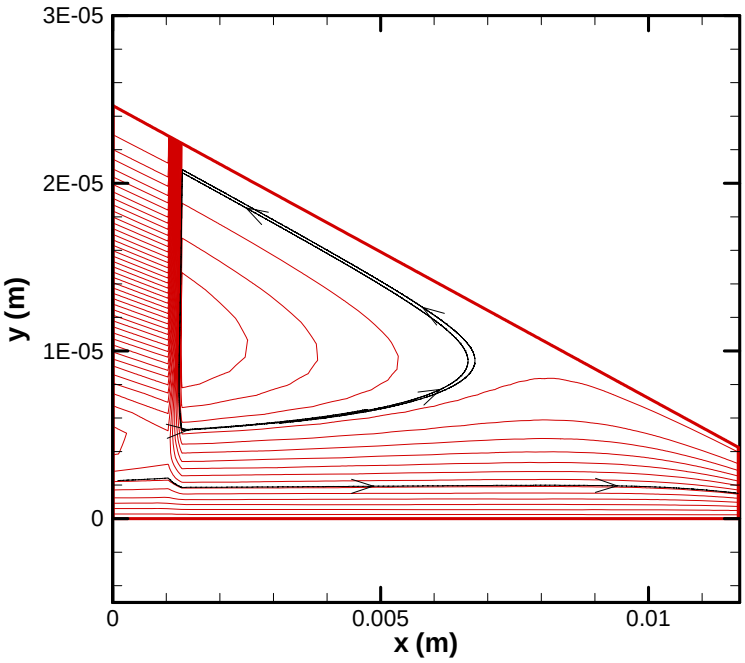

(c) V=50 m/s

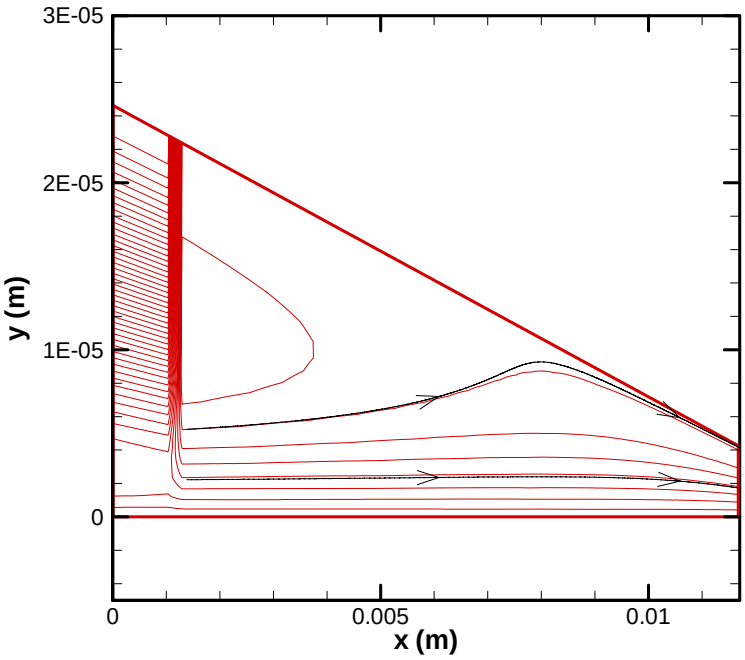

(d) V=100 m/s

Figure A.1 continued

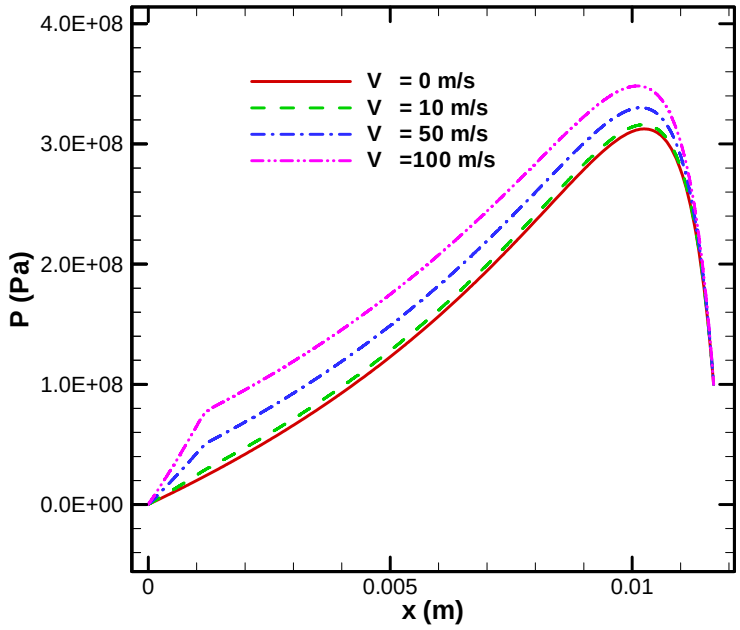

Figure A.2 Pressure distribution with different upstream injection speed for a converging gap ($\theta_1 = 0.10^{o}$)

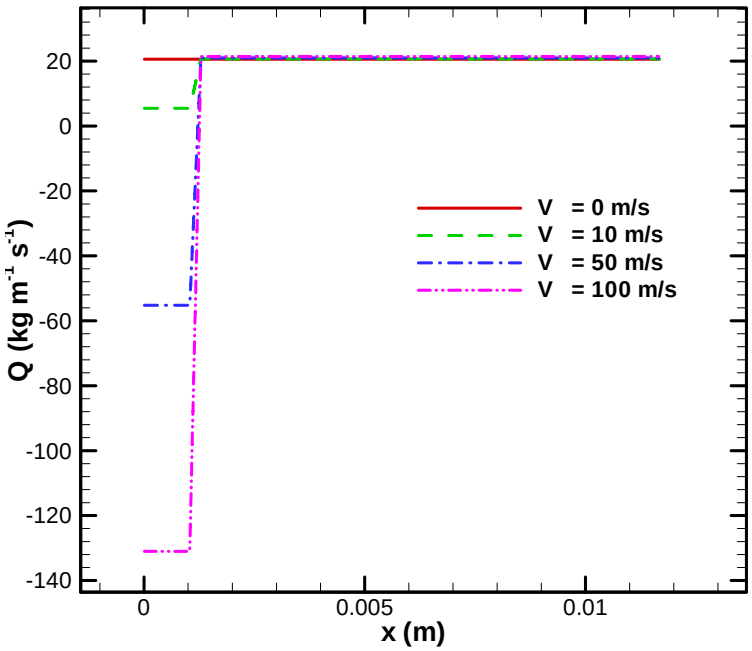

Figure A.3 Mass flow rates along the film with different upstream injection speed for a converging gap ($\theta_1 = 0.10^{o}$)

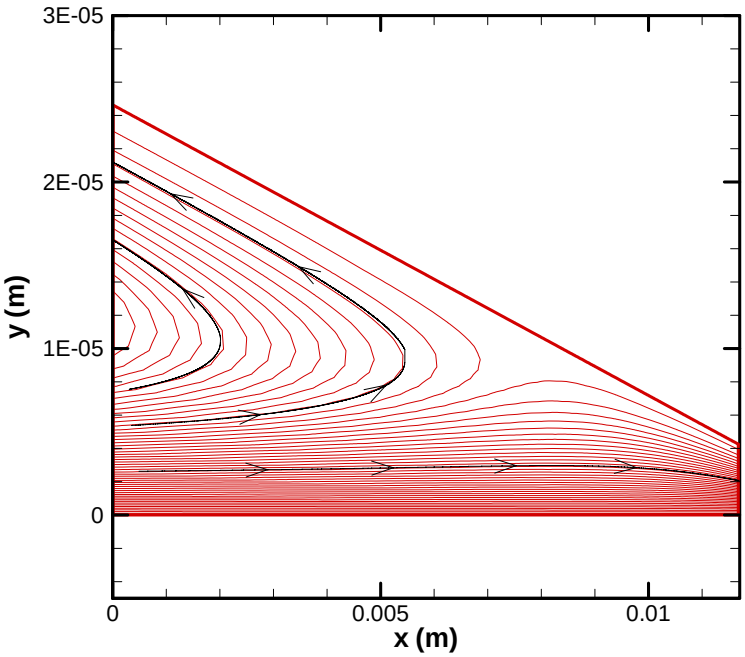

(a) V=0 (No Injection)

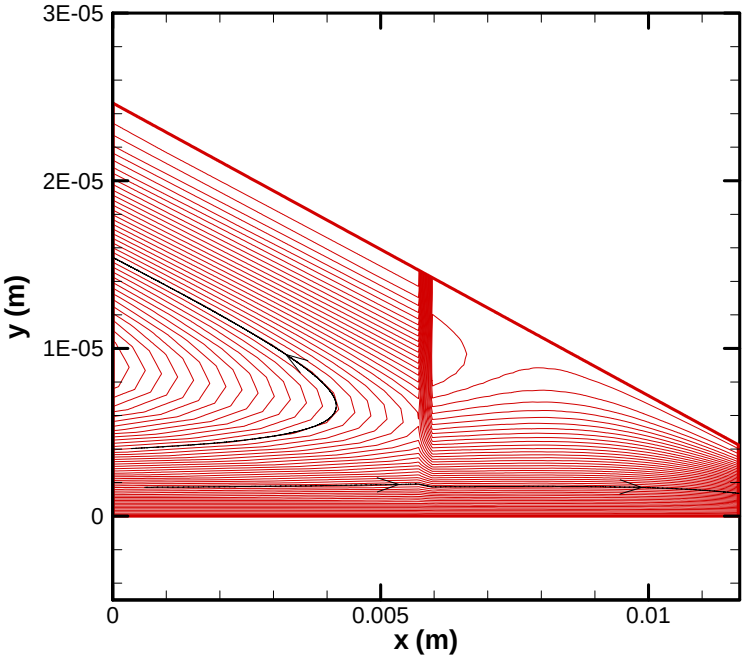

(b) V=10 m/s

Figure A.4 Stream lines with different center injection speed for a converging gap (θ_1 = 0.10 ^{o})

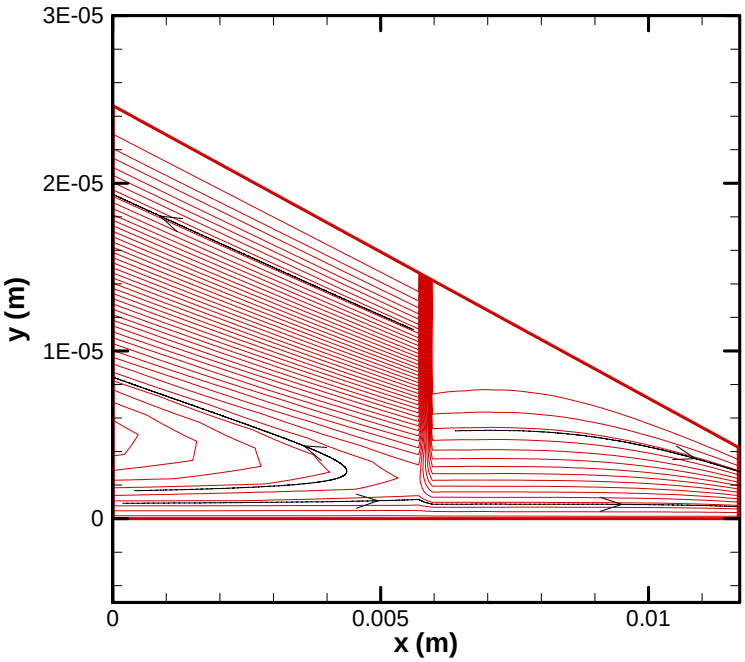

(c) V=50 m/s

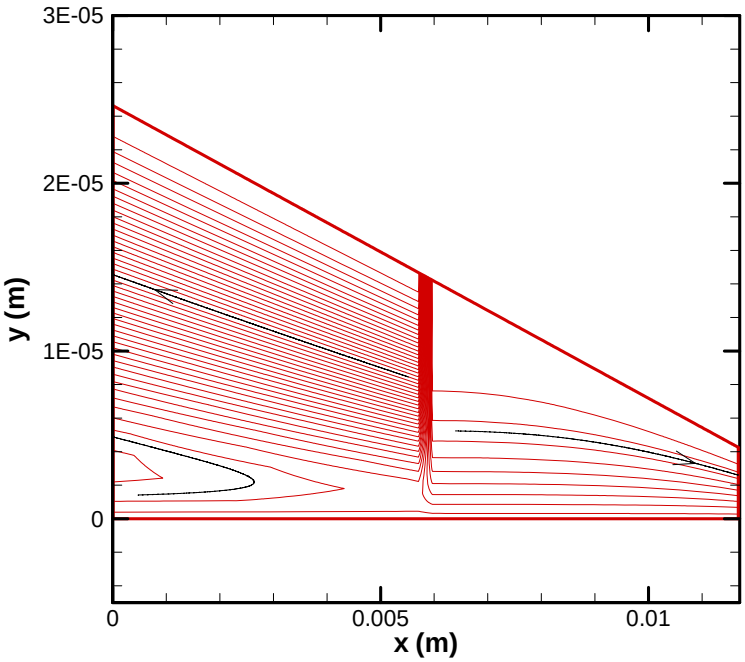

(d) V=100 m/s

Figure A.4 continued

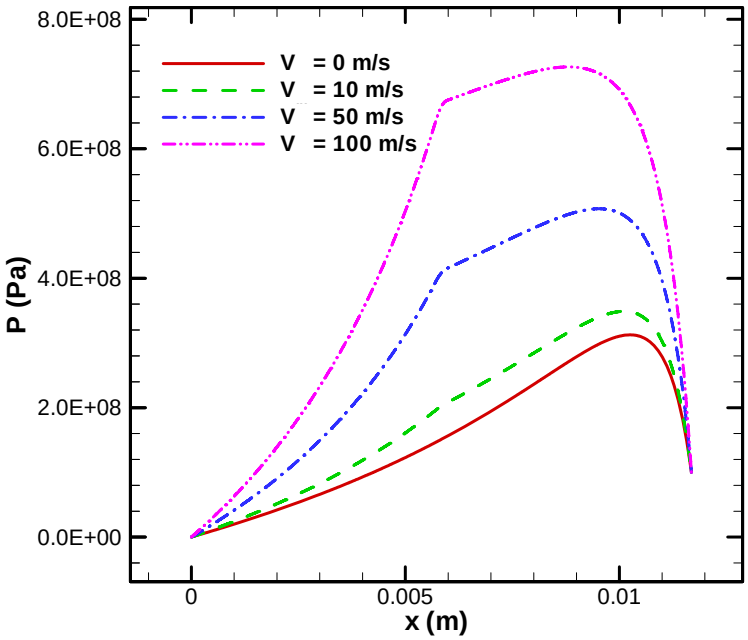

Figure A.5 Pressure distribution with different center injection speed for a converging gap ($\theta_1 = 0.10^{o}$)

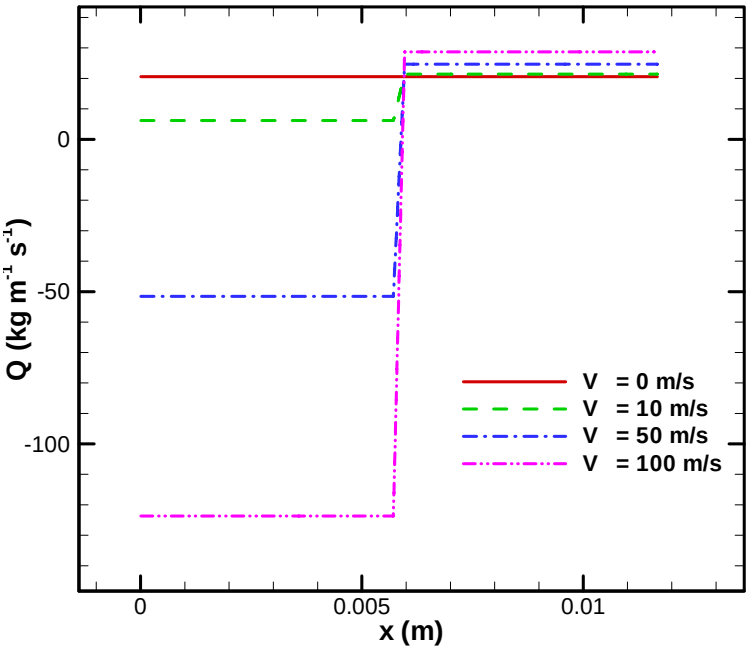

Figure A.6 Mass flow rates along the film with different center injection speed for a converging gap ($\theta_1 = 0.10^{o}$)

Figures A.7 and A.10 contain streamline patterns for a film of constant thickness ($h = 3\sigma$). These figures show that for such parallel surfaces, an injection speed of 10 m/s is insufficient to fill the interface with lubricant, while 50 m/s and 100 m/s completely fill the interface. Figures A.8 and A.11 show that higher film pressures are developed with center injection than upstream injection, and both injection configurations result in much higher film pressures than the previous converging configuration. Figures A.9 and A.12 show that higher injection speeds produce higher flow rates at the trailing edge, especially in center injection, where mass flow rates at both edges are almost equal.

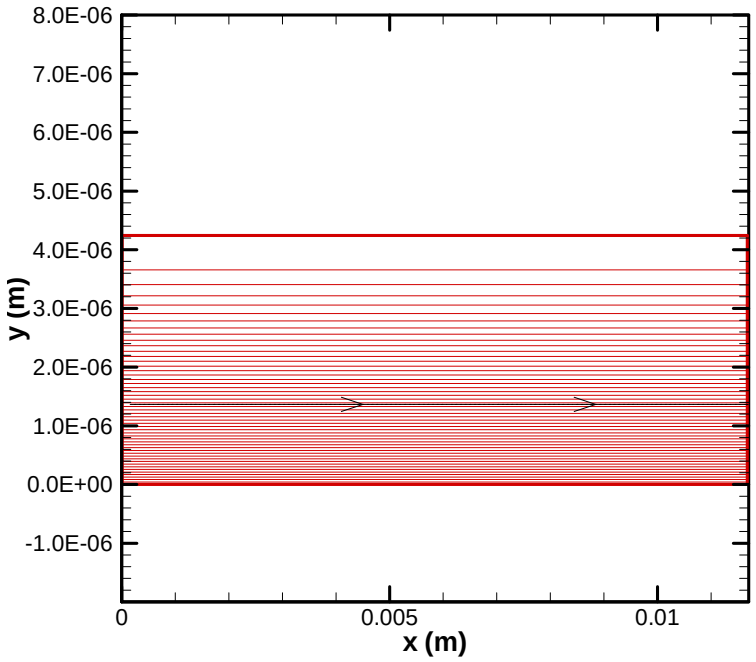

(a) V=0 (No Injection)

Figure A.7 Stream lines with different upstream injection speed for a parallel gap ($\theta_1 = 0^o$)

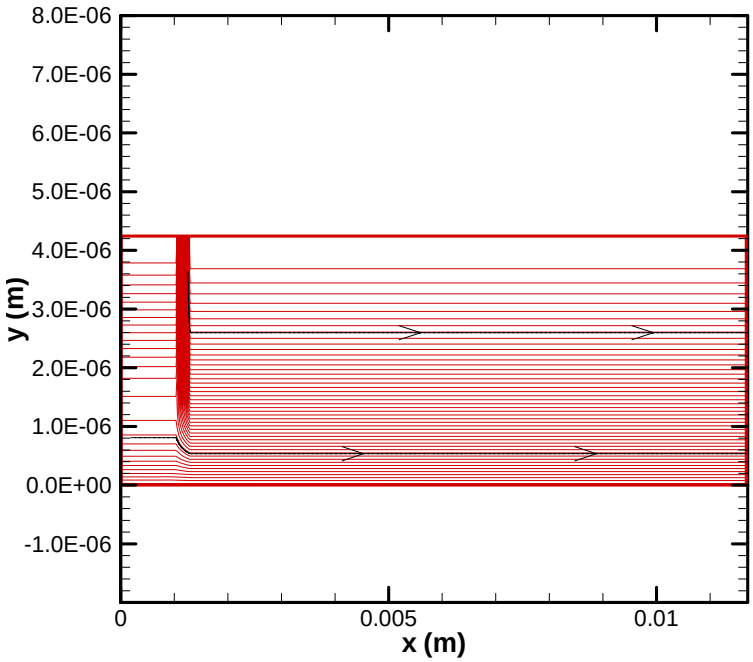

(b) V=10 m/s

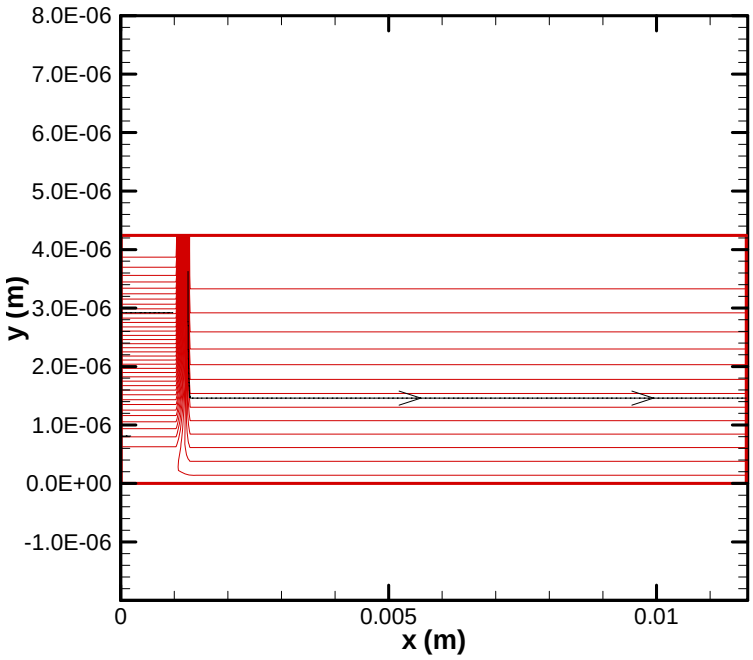

(c) V=50 m/s

Figure A.7 continued

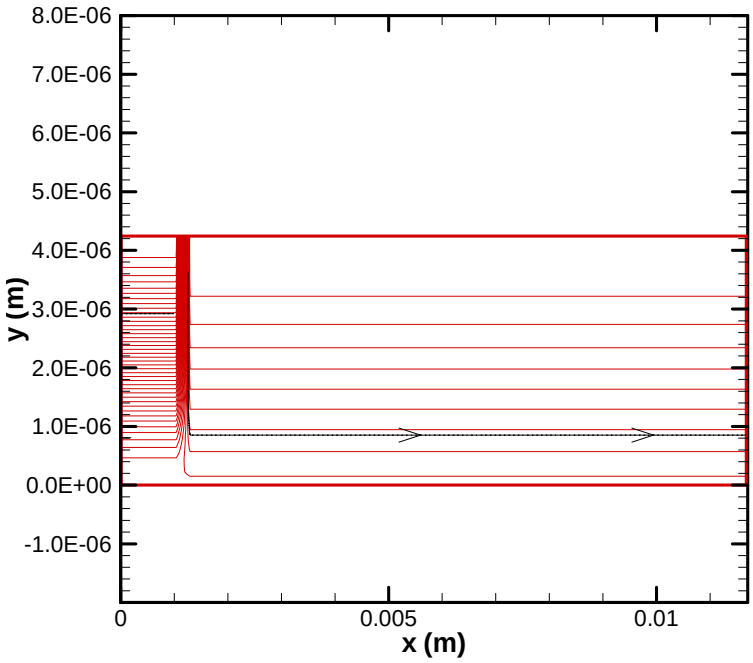

(d) V=100 m/s

Figure A.7 continued

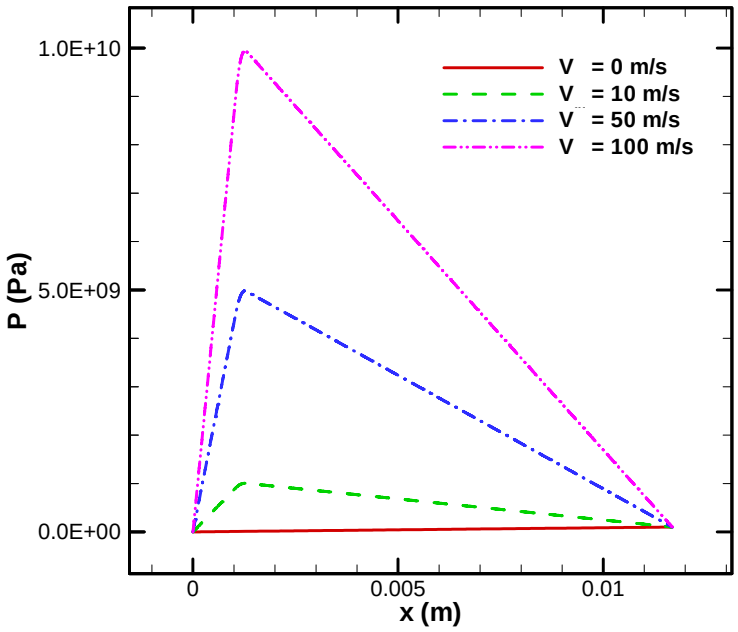

Figure A.8 Pressure distribution with different upstream injection speed for a parallel gap ($\theta_1 = 0^o$)

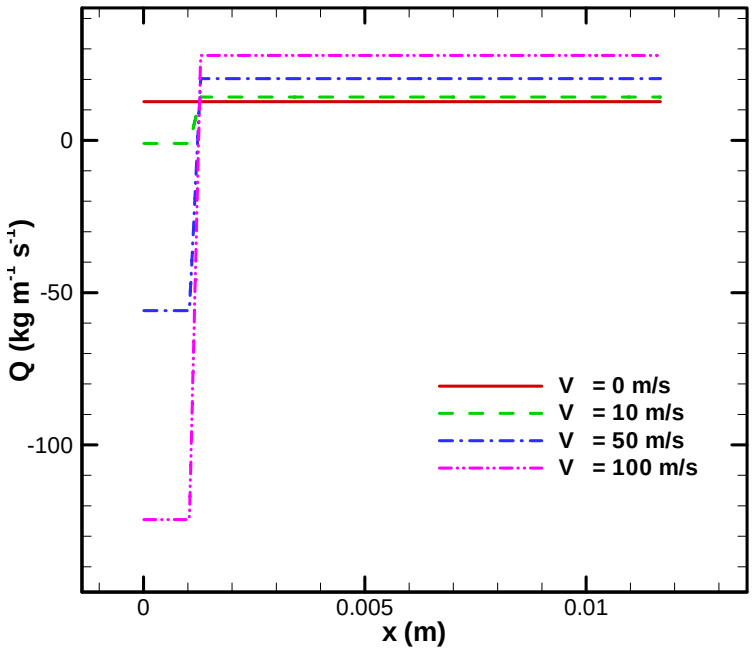

Figure A.9 Mass flow rates along the film with different upstream injection speed for a parallel gap ($\theta_1 = 0^o$)

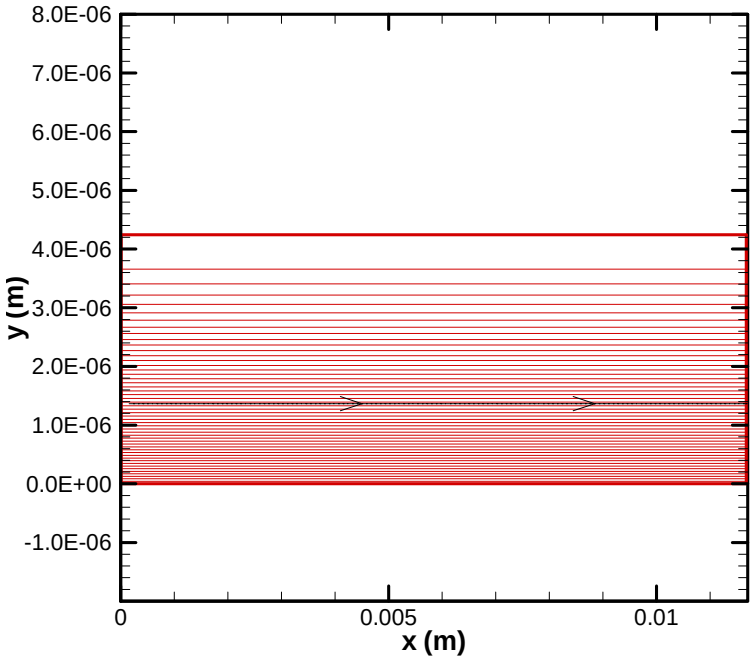

(a) V=0 (No Injection)

Figure A.10 Stream lines with different center injection speed for a parallel gap ($\theta_1 = 0^o$)

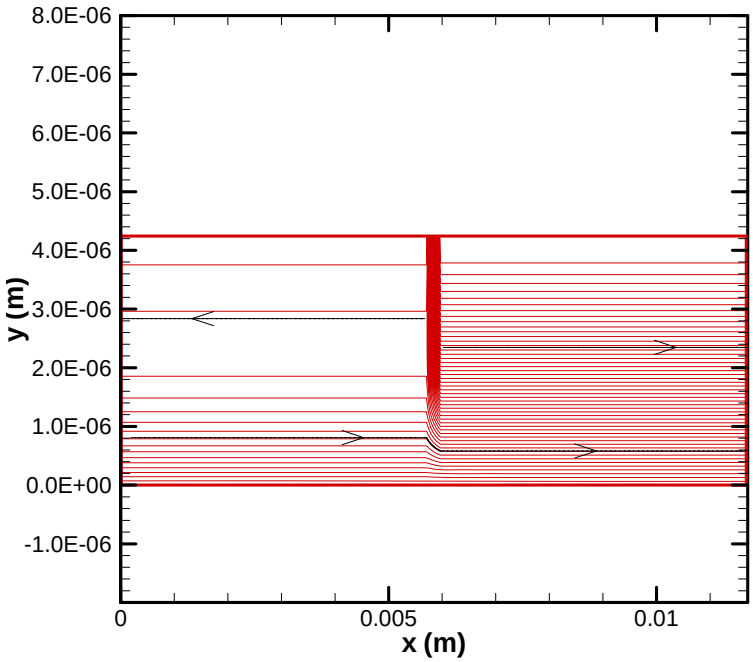

(b) V=10 m/s

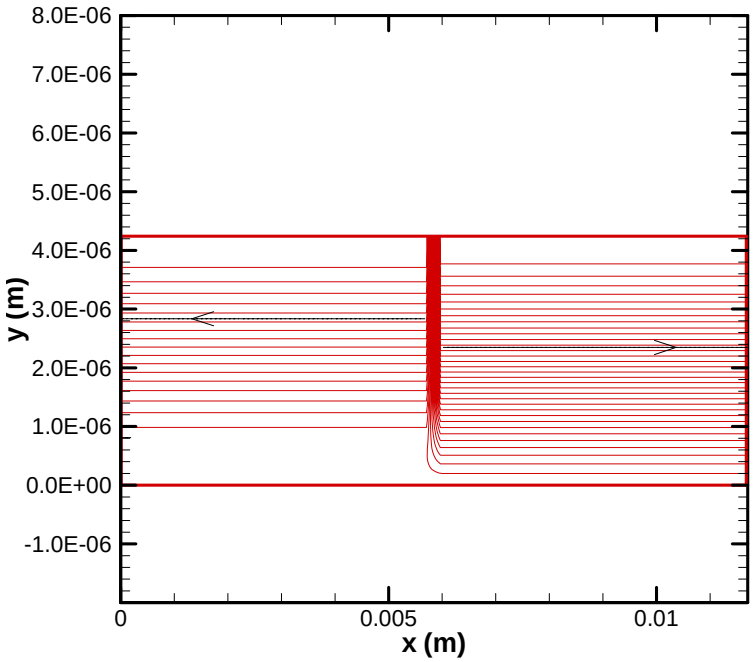

(c) V=50 m/s

Figure A.10 continued

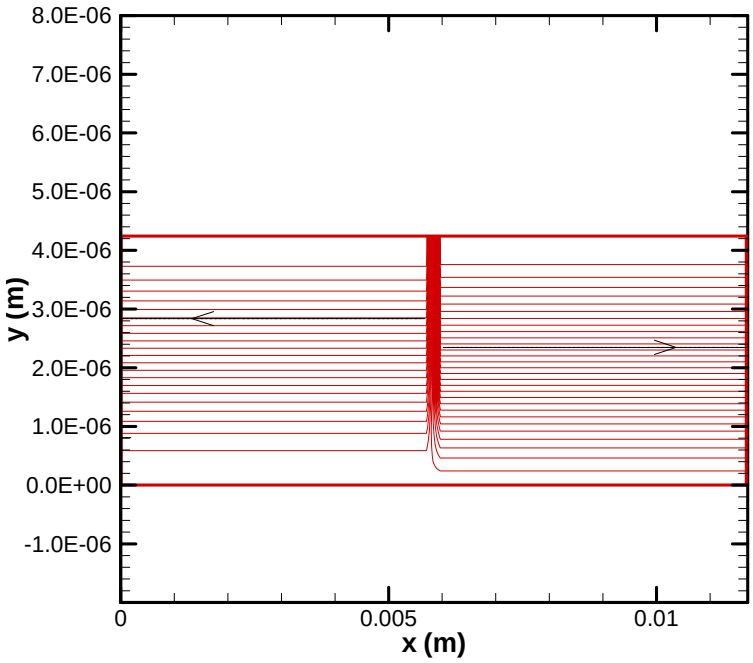

(d) V=100 m/s

Figure A.10 continued

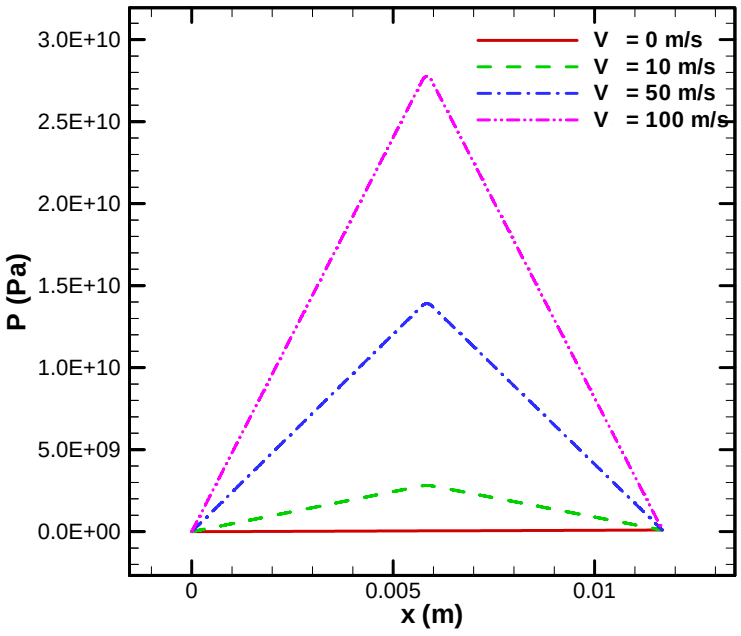

Figure A.11 Pressure distribution with different center injection speed for a parallel gap ($\theta_1 = 0^o$)

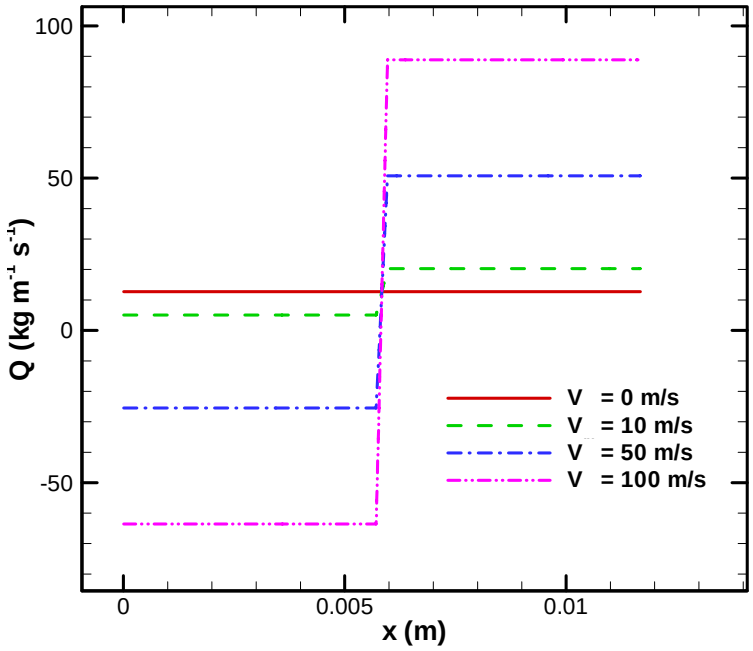

Figure A.12 Mass flow rates along the film with different center injection speed for a parallel gap ($\theta_1 = 0^o$)

Streamline patterns for a diverging film are drawn in Figures A.13 and A.16. For no injection and for an injection speed of 10 m/s, most of the film cavitates, while injection speeds of 50 m/s and 100 m/s suppress cavitation. Figure A.16, for upstream injection, shows that an injection speed of 10 m/s is insufficient to fill the interface with lubricant, while 50 m/s and 100 m/s completely fill the interface. Figure A.16, with center injection, shows that an injection speed of 10 m/s hardly fills the interface; 50 m/s partly fills the interface; and 100 m/s almost completely fills the interface. Figures A.14 and A.17 show that higher film pressures are developed with upstream injection than with center injection (a manner opposite to the converging and uniform film results). The upstream injection pressures are higher than the pressures for a converging film but lower than those for a uniform film with the same injection speeds. The center injection pressures

are lower than the corresponding pressures for both converging and uniform films. However, in both diverging gap injection configurations, most of the fluid flows out from the trailing edge (Figure A.15 and A.18), especially in center injection, where all of the fluid flows out from the trailing edge.

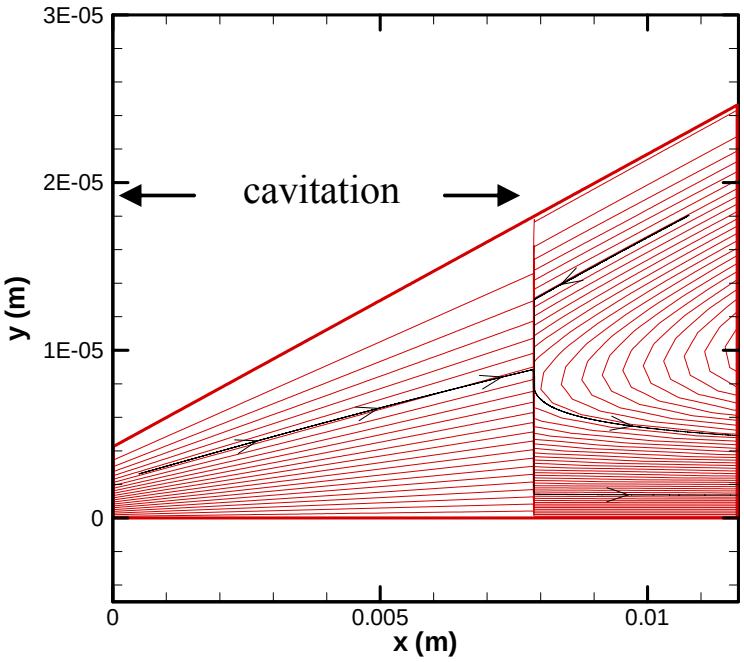

(a) V=0 (No injection)

Figure A.13 Stream lines with different upstream injection speed for a diverging gap (θ_1 = -0.10^o)

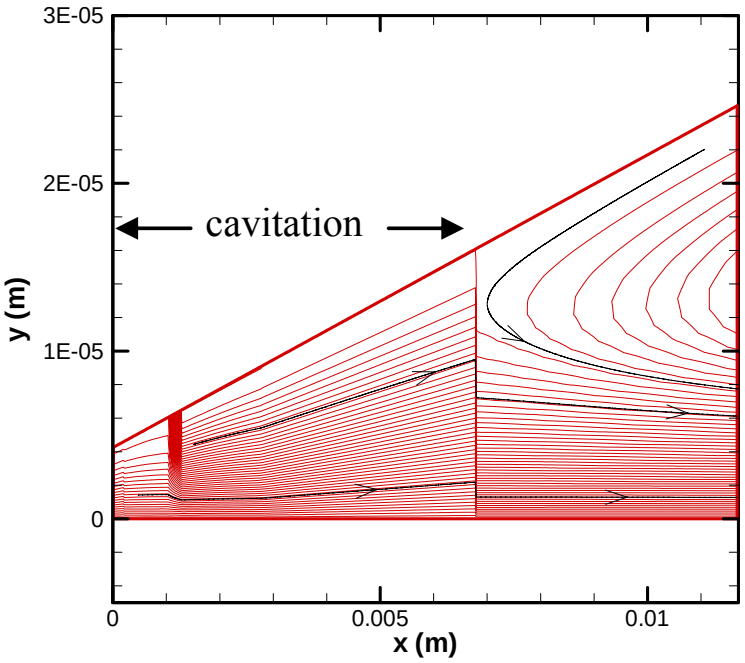

(b) V=10 m/s

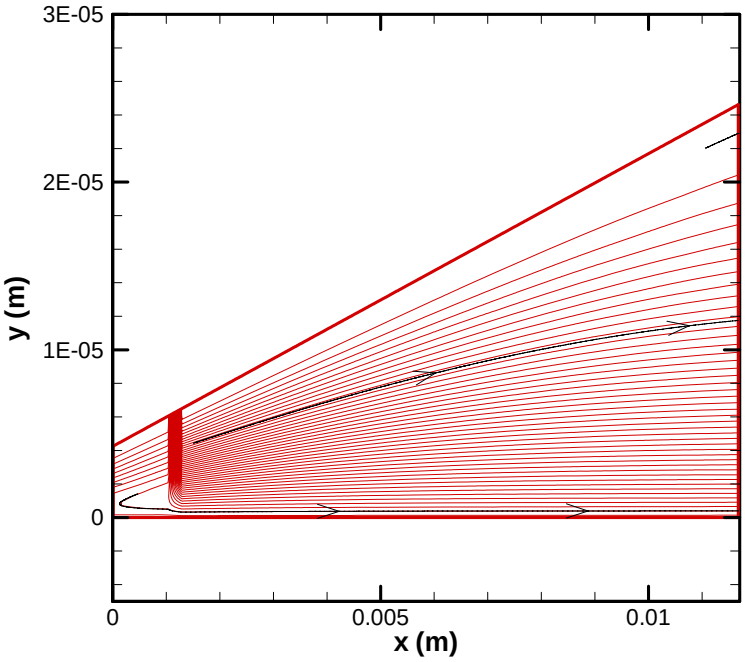

(c) V=50 m/s

Figure A.13 continued

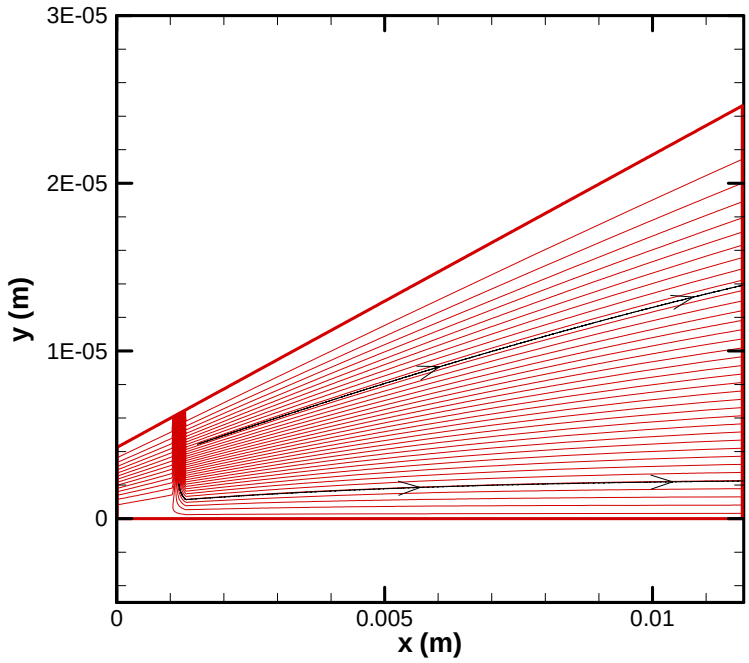

(d) V=100 m/s

Figure A.13 continued

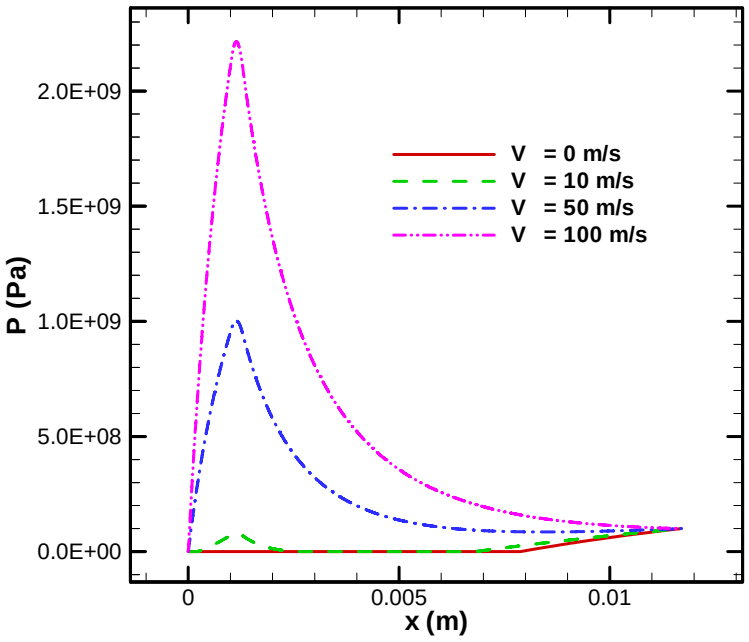

Figure A.14 Pressure distribution with different upstream injection speed for a diverging gap (θ_1 = -0.10^o)

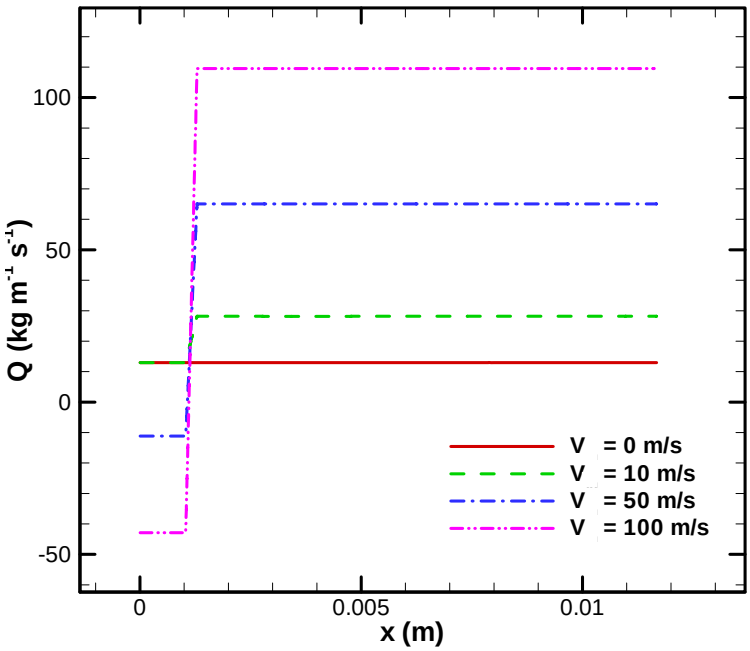

Figure A.15 Mass flow rates along the film with different upstream injection speed for a diverging gap (θ_1 = -0.10^o)

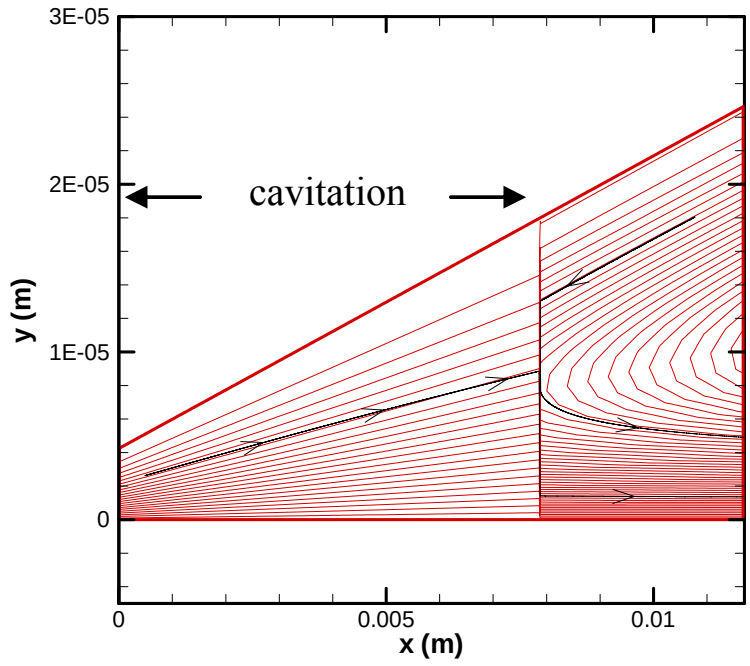

(a) V=0 (No Injection)

Figure A.16 Stream lines with different center injection speed for a diverging gap (θ_1 = -0.10^o)

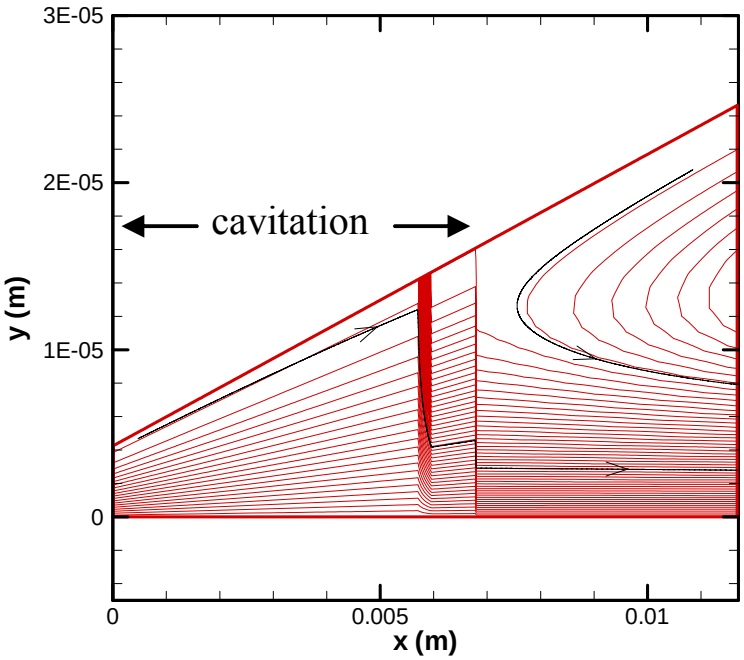

(b) V=10 m/s

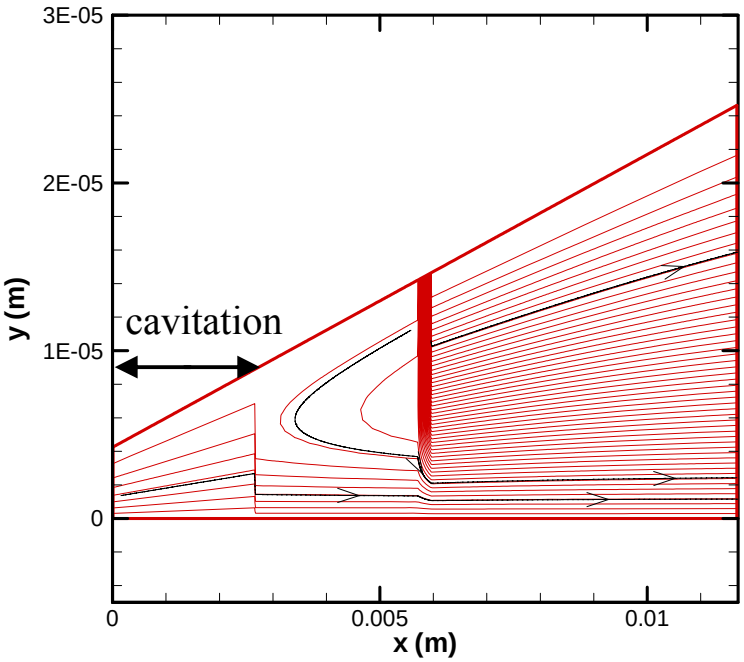

(c) V=50 m/s

Figure A.16 continued

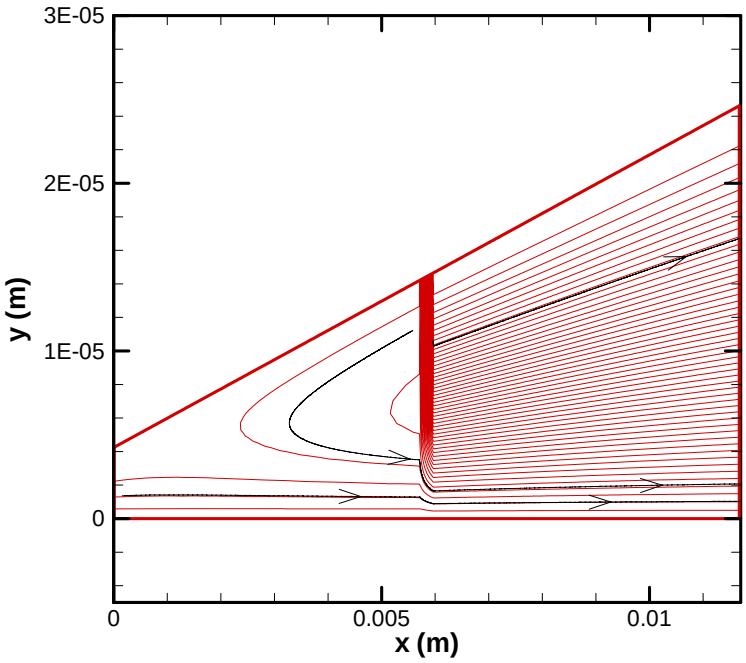

(d) V=100 m/s

Figure A.16 continued

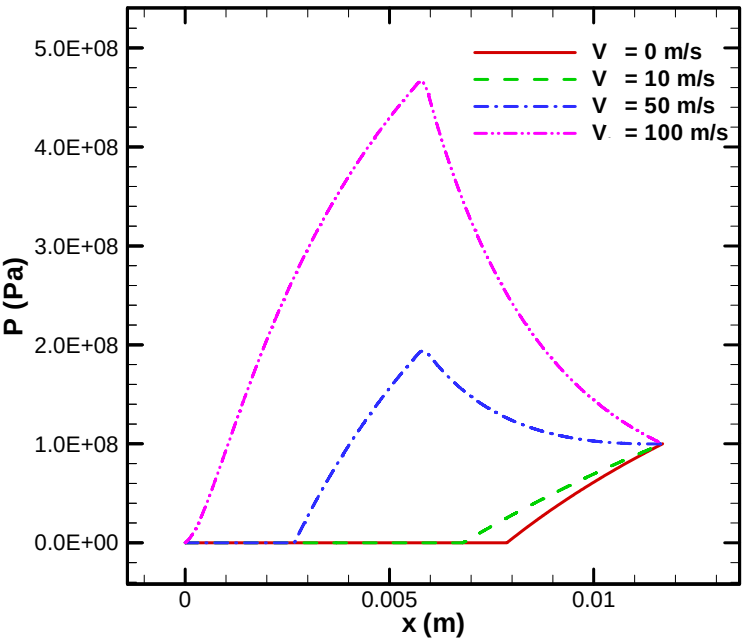

Figure A.17 Pressure distribution with different center injection speed for a diverging gap (θ_1 = -0.10 ^{o})

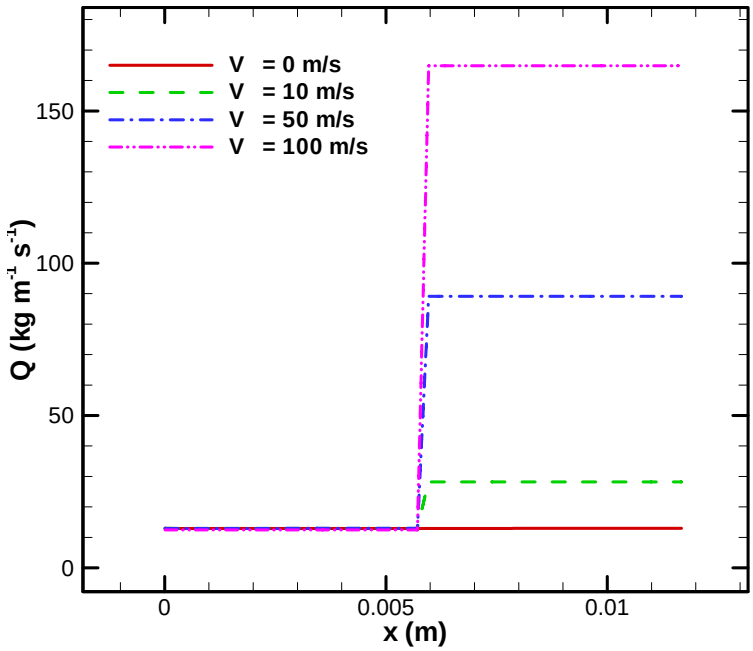

Figure A.18 Mass flow rates along the film with different center injection speed for a diverging gap ($\theta_1 = -0.10^o$)

Comparison of the above injection combinations indicates that upstream injection with a converging gap requires a smaller injection pressure and consumes less lubricant at the trailing edge than the other injection configurations. This study reveals that the most beneficial injection configuration is a converging film with upstream injection.

As mentioned earlier, the flow characteristics in the armature-rail interface gap are unknown and some researchers believe the flow is laminar (Stefani et al., 2001, 2005). The results in the previous section were regenerated with a turbulent model using Constantinescu's formula. Figures A.19-A.21 show the converging gap with upstream injection. The flow patterns (Figure A.19) and mass flow rates (Figure A.21) are similar to the results obtained earlier with the laminar model (Figures A.1 and A.3). However,

the fluid pressure predicted in the turbulent model (Figure A.20) is much higher than in the laminar model (Figure A.2). Similar results and even higher pressures are observed in the other configurations, such as center injection and parallel gaps. Such high fluid pressures will cause armature material yielding and failing. However, no evidence of yielding has been observed in experiments. Therefore, it is believed that the laminar model is more appropriate for this EML application, consistent with the results of Stefani et al.

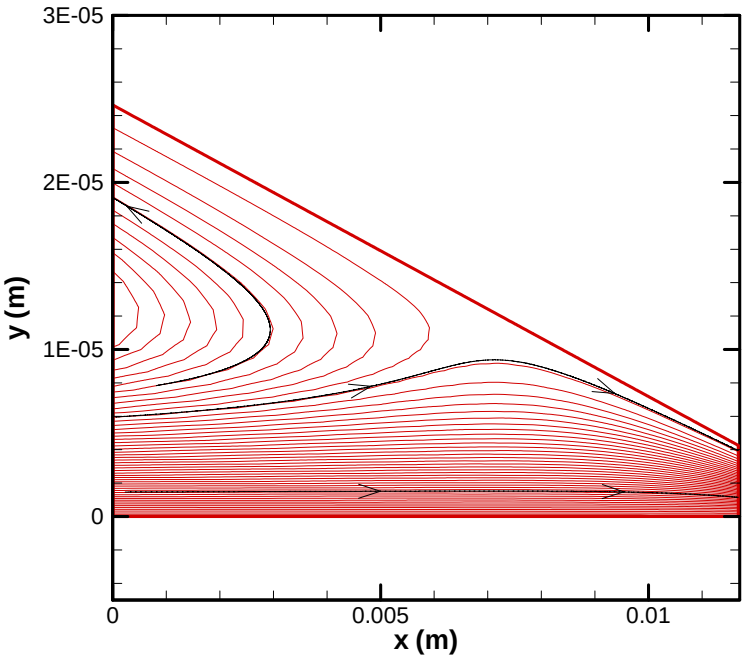

(a) V=0 (No injection)

Figure A.19 Stream lines with different upstream injection speed for a converging gap by a turbulent model ($\theta_1 = 0.10^o$)

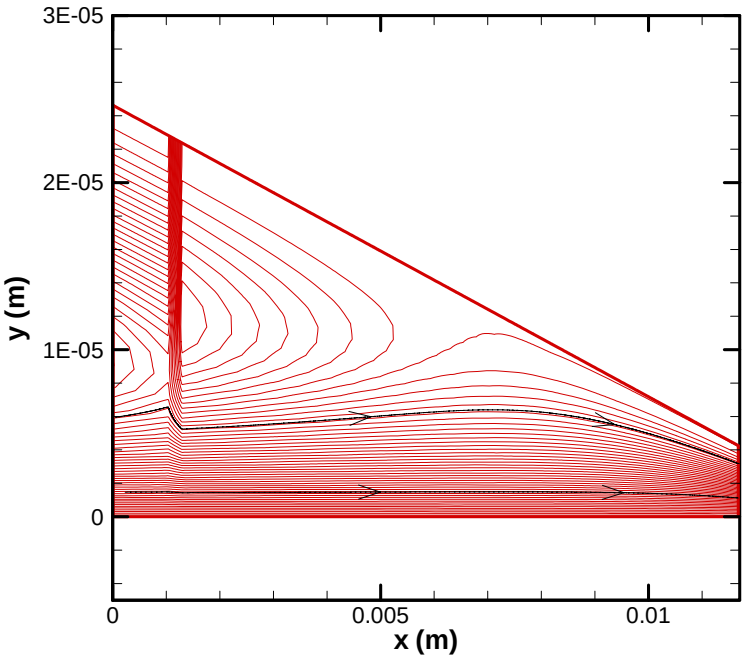

(b) V=10 m/s

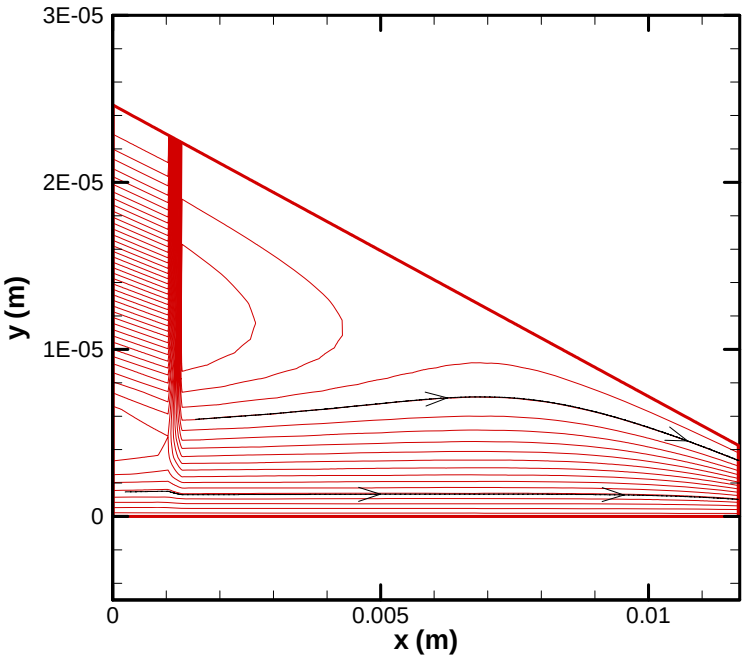

(c) V=50 m/s

Figure A.19 continued

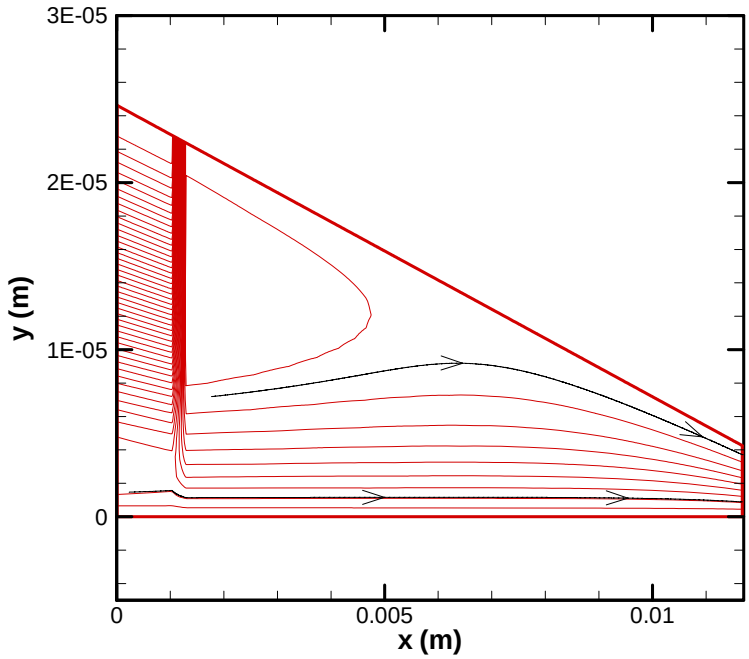

(d) V=100 m/s

Figure A.19 continued

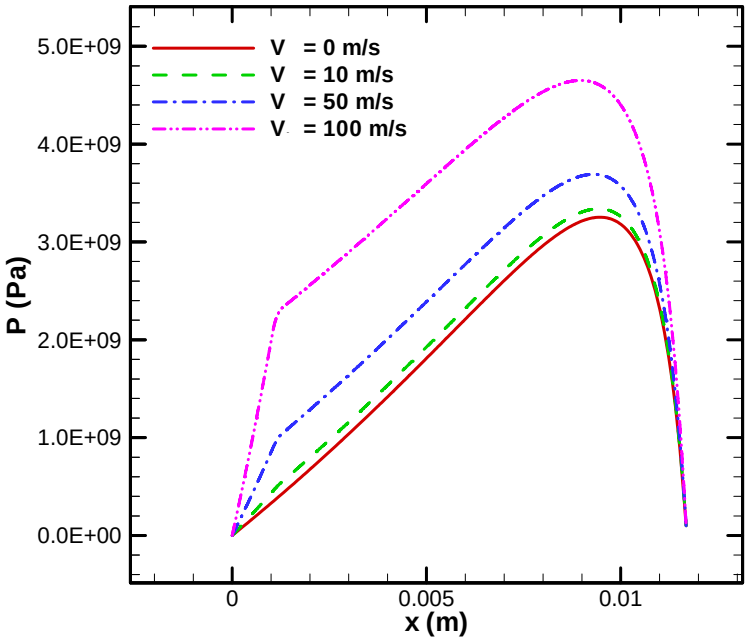

Figure A.20 Pressure distribution with different upstream injection speed for a converging gap by a turbulent model ($\theta_1 = 0.10^o$)

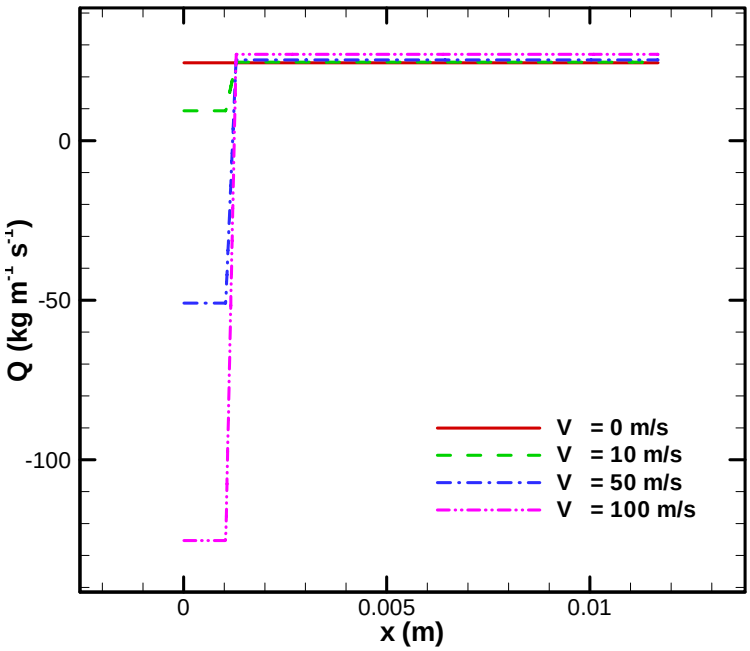

Figure A.21 Mass flow rates along the film with different upstream injection speed for a converging gap by a turbulent model ($\theta_1 = 0.10^o$)

APPENDIX B

RESULTS AND DISCUSSION OF MHD MODEL

The MHD model simulates the launch and injection process solely with a lubrication model. The electromagnetic field is not calculated and the magnetic pressure at the trailing edge is computed from equation 3.34. Interface contact and deformation are also neglected and the interface is assumed to be a converging gap with a constant slope. All the material properties are constant because a thermal module is not included in this analysis.

Figure B.1 contains the histories of the mass flow rates for the base case configuration with the MHD model. In the computation, the viscosity of the fluid μ is 2.0 x 10^{-3} Pa-s, the density ρ is 6.0 x 10^{3} kg/m^{3}, the minimum film thickness $h_{\min}$ is 4.24 x 10^{-6} m, and the combined standard deviation of both the armature and the rail surfaces σ is 1.414 x 10^{-6} m. By validating with experimental results from a dry shot without lubricant and by neglecting friction, the inductance gradient *L'* is determined to be 0.53 uH/m. The gap angle is chosen to be 0.3^{o} converging. As shown in the figure, the MHD model predicts a similar injection process compared to the METHD model: lubricant in the reservoir is almost all driven out at the beginning of the launch; the pocket is immediately filled and excess fluid flows out from the leading edge at once. However, since the interface gap height change during the launch is not considered, the MHD model predicts much smaller lubrication consumption at the interface.

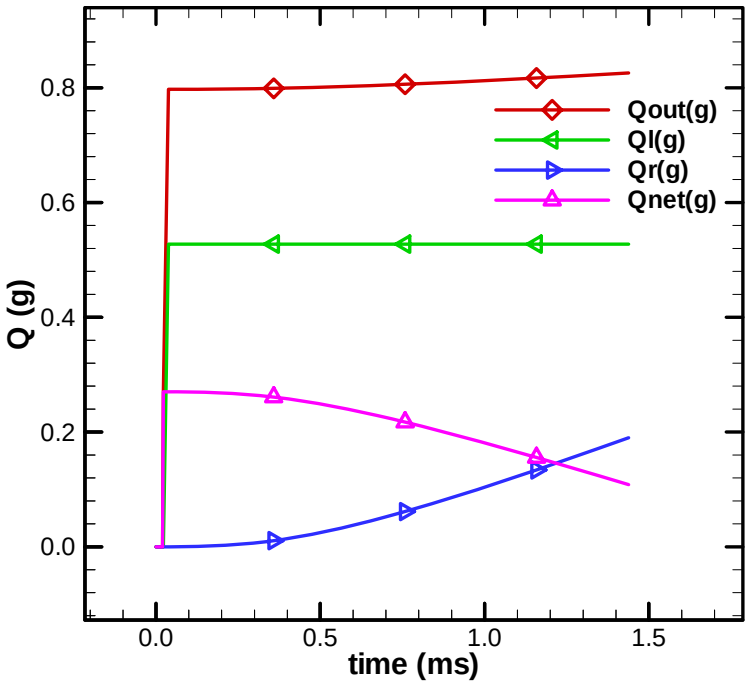

Figure B.1 Mass flow amount history of the MHD model

APPENDIX C

RESULTS AND DISCUSSION OF MEHD MODEL

The predicted mass flow amounts of the base case in Section 4.1, using the MEHD model, are plotted in Figure C.1. The MEHD model predicts a larger lubricant consumption at the interface compared to the METHD model. Lubricant in the pocket empties out at 1.35 ms, which does not agree with the experimental measurements presented in Figure 4.28a. A possible reason for this mismatch is neglect of temperature dependent material properties and thermal deformation. Firstly, the lubricant viscosity at room temperature is higher than that at a higher temperature. Numerical tests show that an increased viscosity leads to higher lubricant consumption at the interface. Secondly, comparing with the film thickness history prediction from the METHD model in Figure 4.15, the MEHD model predicts a larger film thickness as shown in Figure C.2. The uneven temperature field in the METHD model tends to produce a thermal deformation and squeeze the armature leg towards the rails, which results in smaller film thickness.

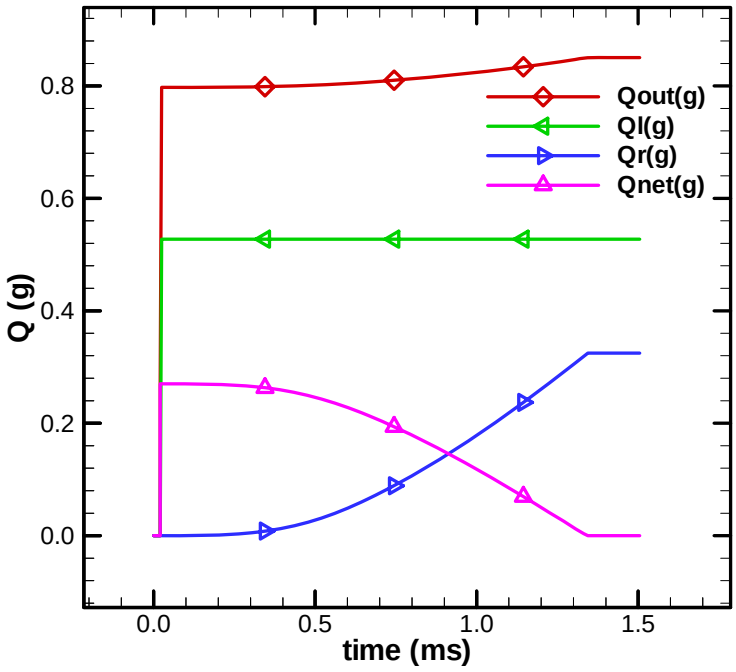

Figure C.1 Mass flow amount history of the MEHD model

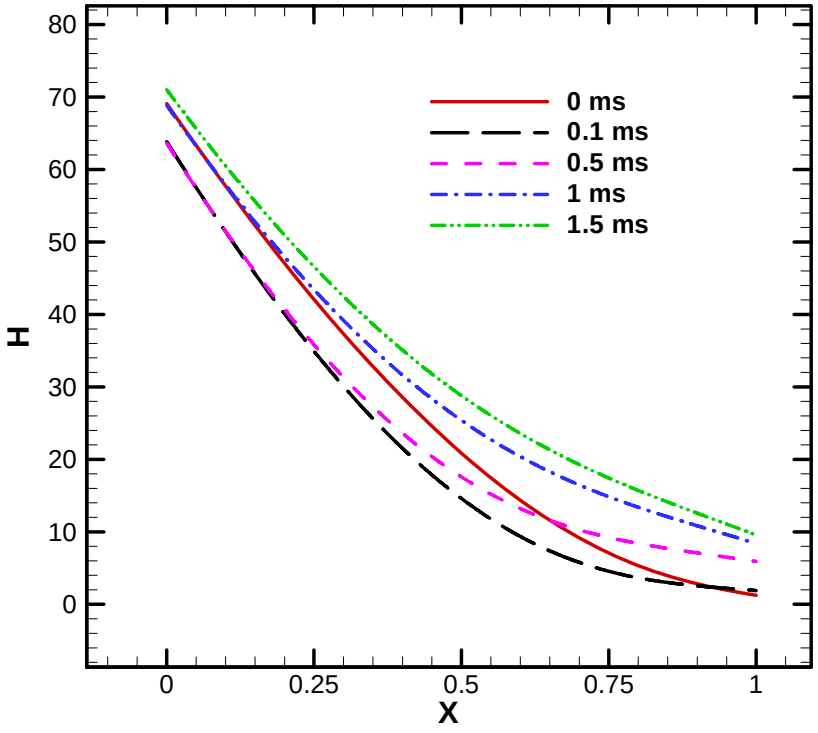

Figure C.2 Nondimensional interface gap profiles at different times of the MEHD model

REFERENCES

1. ANSYS, Inc., "ANSYS Release 9.0 Documentation," 2004.

2. Bair, S., Personal communication, in Georgia Tech, Atlanta, GA, 2008.

3. Bansal, D., Streator, J., Kovalchenko, A., and Danyluk, S., "Effect of current polarity on tribological behavior of copper-aluminum electrical interface," IJTC 2007, 2008, pp. 467–469.

4. Bansal, D., and Streator J., "Influence of surface roughness on friction and contact resistance in sliding electrical contacts," IJTC 2007, 2008, pp. 1057–1059.

5. Barber, J. P. and Dreizin Y. A., "Model of contact transitioning with realistic armature-rail interface," IEEE Trans., vol. 31, no. 1, 1995, pp. 96–100.

6. Boley, B. A. and Weiner, J. H., Theory of thermal stresses, Mineola, NY: Dover Publ., inc, 1997.

7. Brunetiere, N., Tourneie B., and Frene J., "Influence of fluid flow regime on performances of non-contacting liquid face seals," J. of Tribology, vol. 124, 2002, pp. 515–523.

8. Brunetiere, N., Tourneie B., and Frene J., "TEHD lubrication of mechanical face seals in stable tracking mode: part 1 – numerical model and experiments," J. of Tribology, vol. 125, 2003, pp. 608–616.

9. Chang, K. M., Lee, S. C. and Li, S. H., "Squeeze film damping effect on a MEMS torsion mirror," J. Micromech. Microeng., vol 12, 2002, pp. 556–561.

10. Critchley, R., Leyden, C., and Argyle A. P. J., "The use of coupled EM-hydro finite element techniques for the design of railguns," IEEE Trans. Magn., vol. 35, no. 1, 1995, pp. 576–581.

11. Daneshjoo, K., Rahimzadeh, M., Ahmadi, R., and Ghassemi, M., "Dynamic response and armature critical velocity studies in an electromagnetic railgun," IEEE Trans. Magn., vol. 43, no. 1, 2007, pp. 126–131.

12. Drobyshevski, E.M., Kolesnikova, E.N., and Yuferev, V.S., "Calculating the liquid film effect on solid armature rail-gun launching", IEEE Trans. Magn., vol. 35, no. 1, 1999, pp. 53–58.

13. Drobyshevskii, E. M., Kolesnikova, E. N., and Yuferev, V. S., "Influence of lubricant on the motion of a body in an electromagnetic raigun accelerator. I. Electric current distribution in the accelerated body and the rails," Technical Phys., vol. 44, no. 7, 1999, pp. 831–838.

14. Drobyshevskii, E. M., Kolesnikova, E. N., and Yuferev, V. S., "Influence of lubricant on the motion of a body in an electromagnetic raigun accelerator. II. Temperature distribution in the armature, rail and liquid film," Technical Phys., vol. 44, no. 10, 1999, pp. 1234–1241.

15. Drobyshevski E. M. et al., "Physics of solid armature launch transition into arc mode," IEEE Trans. Magn., vol. 37, no. 1, 2001, pp. 62–66.

16. Elrod, H. G. and Ng, C. W., "A theory for turbulent fluid films and its application to bearings," J. of Lubrication Technology, 1967, pp. 346–362.

17. Engel, T. G., Neri, J. M., and Veracka, M. J., "Characterization of the velocity skin effect in the surface layer of a railgun sliding contact," IEEE Trans. On Magn., vol. 44, no. 7, 2008, pp. 1837–1844.

18. Finnemore, E. J. and Franzini, J. B., Fluid mechanics 10th edition, New York, NY: McGraw-Hill, 2002, pp. 264–265.

19. Flegontova, E. Yu. and Yuferev, V. S., "Influence of lubricant on the motion of a body in an electromagnetic raigun accelerator. II. Hydrodynamics of a conducting lubricant," Technical Phys., vol. 44, no. 10, 1999, pp. 1226–1233.

20. Gere, J. M., Mechanics of materials 5th edition, Pacific Grove, CA: Brooks/Cole, 2000, pp. 609–615.

21. Ghassemi, M. and Pasandeh R., “Thermal and electromagnetic analysis of an electromagnetic launcher,” IEEE Trans. Magn., vol. 39, no. 3, 2003, pp. 1819–1822.

22. Ghassemi, M. and Barsi, Y. M., “Effect of liquid film (indium) on thermal and electromagnetic distribution of an electromagnetic launcher with new armature,” IEEE Trans. Magn., vol. 41, no. 1, 2005, pp. 408–413.

23. Ghassemi, M., Barsi, Y. M., and Hamedi, M. H., “Analysis of force distribution acting upon the rails and the armature and prediction of velocity with time in an electromagnetic launcher with new method,” IEEE Trans. Magn., vol. 43, no. 1, 2007, pp. 132–136.

24. Hopkins, D. A. et al., “Analysis of startup behavior in a C-shaped armature using linked EMAP3D/DYNA3D finite element codes,” IEEE Trans. Magn., vol. 35, no. 1, 1999, pp. 59–64.

25. Hsieh, K. T., “A Lagrangian formulation for mechanically, thermally coupled electromagnetic diffusive processes with moving conductors,” IEEE Trans. Magn., vol. 31, no. 1, 1995, pp. 604–609.

26. Hsieh, K. T. and Kim, B. K., “3D modeling of sliding electrical contact,” IEEE Trans. Magn., vol. 33, no. 1, 1997, pp. 237–239.

27. James, T. E. and James, D. C., “Resistive contact region solid armatures: electro-thermal design optimization,” IEEE Trans. Magn., vol. 31, no. 1, 1995, pp. 162–167.

28. James, T. E., “Current wave and magnetic saw-effect phenomena in solid armatures,” IEEE Trans. Magn., vol. 31, no. 1, 1995, pp. 622–627.

29. James T. E. and James D. C., “Contact pressure distribution and transition in solid armatures,” IEEE Trans. Magn., vol. 37, no. 1, 2001, pp. 81–85.

30. Jerome, T. T., “Dynamic response of electromagnetic railgun due to projectile movement,”, IEEE Trans. Magn., vol. 39, no. 1, 2003, pp. 472–475.

31. Johnson A. J. and Moon F. C., “Elastic waves and solid armature contact pressure in electromagnetic launchers,” IEEE Trans. Magn., vol. 42, no. 3, 2006, pp. 422–429.

32. Kim, B.K., Hsieh, K. T., and Bostick F. X., "A three-dimensional finite element model for thermal effect of imperfect electric contacts," IEEE Trans. Magn., vol. 35, no. 1, 1999, pp. 170–174.

33. Kothmann, R. E. and Stefani, F., "A thermal hydraulic model of melt-lubrication in railgun armatures," IEEE Trans. Magn., vol. 37, no. 1, 2001, pp. 86–91.

34. Li, W. L., Weng, C. I., and Hwang, C. C., "Effects of roughness orientations on thin film lubrication of a magnetic recording system," J. Phys. D: Appl. Phys., vol 28, 1995, pp. 1011–1021.

35. Li, W. L., and Weng, C. I., "Modified average Reynolds equation for ultra-thin film gas lubrication considering roughness orientations at arbitrary Knudsen numbers," Wear, vol. 209, 1997, pp. 292–300.

36. Marshall, R. A. and Wang, Y., "Railguns: their science and technology," China Machine Press, Beijing, China, 2004.

37. Merril, R. and Stefani F., "Electrodynamics of the current melt-wave erosion boundary in a conducting half-space," IEEE Trans. Magn., vol. 39, no. 1, 2003, pp. 66–71.

38. Merrill, R. and Stefani, F., "A turbulent melt-lubrication model of surface wear in railgun armatures," IEEE Trans. Magn, vol. 41, No. 1, 2005, pp. 414–419.

39. Newill, J. F., Powell J. D., and Zielinski A. E., "Coupled finite-element codes for armature design," IEEE Trans. Magn., vol. 39, no. 1, 2003, pp. 148–152.

40. Patankar, S. V., Numerical heat transfer and fluid flow, Taylor and Francis, 1980.

41. Patir, N. and Cheng, H. S., "An average flow model for determining effects of three-dimensional roughness on partial hydrodynamic lubrication," J. of Lubrication Technology, vol. 100, 1978, pp. 12–17.

42. Patir, N. and Cheng, H. S., "Application of average flow model to lubrication between rough sliding surfaces," J. of Lubrication Technology, vol. 101, 1979, pp. 220–229.

43. Payvar, P. and Salant, R. F., "A computational method for cavitation in a wavy mechanical seal,", J. of Tribology, vol. 114, 1992, pp. 199–204.

44. Peklenik, J., "New development in surface characterization and measurement by means of random process analysis," Proc. Instn. Mech. Engrs., vol. 182, 1967, pp. 108–111.

45. Powell, J. D. and Zielinski, A. E., "Current and heat transfer in the solid-armature railgun," IEEE Trans. Magn., vol. 31, no. 1, 1995, pp. 645–650.

46. Powell, J. D. and Zielinski, A. E., "Observation and simulation of solid-armature railgun performance," IEEE Trans. Magn., vol. 35, no. 1, 1999, pp. 84–89.

47. Rapka, J. R., Hildenbrand, D.J., and Weldon, J.M., "The determination of launch induced static and dynamic rail deflection of a Benet 50 mm railgun barrel," IEEE Trans. Magn., vol. 31, no. 1, 1995, pp. 231–236.

48. Salant, R. F., Maser, N., and Yang, B., "Numerical model of a reciprocating hydraulic rod seal," J. Tribl., vol.129, 2007, pp. 91–97.

49. Salant, R. F. and Shen, D., "Hydrodynamic effects of shaft surface finish on lip seal operation," Tribology Trans., vol. 45, 2002, pp. 404–410.

50. Salant, R. F. and Wang, L., "Simulation of liquid lubricant injection in electromagnetic launcher armatures," IEEE Trans. Magn., vol. 43, No. 1, 2007, pp. 364–369.

51. Spells, K. E., "The determination of the viscosity of liquid Gallium over an extended range of temperature," Proc. Phys. Soc., vol. 48, 1936, pp. 299–311.

52. Streator, J. L., "A model of mixed lubrication with capillary effects," Proc. 15th Leeds-Lyon Symp. On Tribl., Vienna, Austria, 2001, pp. 121–128.

53. Szeri, A. Z., "Tribology: friction, lubrication, and wear," McGraw–Hill, 1980.

54. Thiagarajan, V. and Hsieh, K. T., "An algorithm to couple an external RL circuit with the finite-element code EMAP3D," IEEE Trans. Magn., vol. 43, no. 1, 2007, pp. 376–379.

55. Tripp, J. H., “Surface roughness effects in hydrodynamic lubrication: the flow factor method,” J. of Lubrication Technology, vol. 105, 1983, pp. 458–465.

56. Tzeng, J. T., “Dynamic response of electromagnetic railgun due to projectile movement,” IEEE Trans. Magn., vol. 39, no. 1, 2003, pp. 472–475.

57. Wang, L., Bair, S. and Salant, R. F., “Numerical prediction of electromagnetic launch history with liquid lubricant injection,” submitted to IEEE Trans. Magn.

58. Williams, J. A., Engineering Tribology, New York: Oxford University Press, 1994, pp. 116–122.

59. Woods, L. C., “The current melt-wave model,” IEEE Trans. Magn., vol. 33, no. 1, 1997, pp. 152–156.

60. http://www.efunda.com/materials/elements/element_info.cfm?Element_ID=Ga, accessed on Nov 11, 2008.

61. Young, F. J. and Hughes, W. F., “Rail and armature current distributions in electromagnetic launchers,” IEEE Trans. Magn., vol. 18, no. 1, 1982, pp. 33–41.

62. Zielinski,A. E., Newill, J. F., and Powell, J. D., “Experiments to assess structural loads during solid armature contact transition,” IEEE Trans. Magn., vol. 39, no. 1, 2003, pp. 92–96.

VITA

LEI WANG

Lei Wang was born in Longchang, Sichuan Province, China in 1981. He attended Tsinghua University from 1998 to 2004, where he received a Bachelor's degree in mechanical engineering and automation and a Master's degree in material processing engineering, both from mechanical engineering department. His master's thesis dealt with numerical simulation of fluid flow in thin slab continuous casting molds with an electromagnetic brake. He entered the Woodruff School of Mechanical Engineering at Georgia Institute of Technology in 2004 to pursue his Ph.D. under the guidance of Prof. Richard F. Salant. He studies the coupled fields at the armature-rail interface in an electromagnetic launcher system with lubricant injection, involving film lubrication, electromagnetics, contact mechanics, thermal effects, and deformation mechanics.